THE UNIVERSITY *of* EDINBURGH

THE UNIVERSITY OF EDINBURGH

Single cell measurements of bacterial physiology traits during exposure to an external stress

Ekaterina Krasnopeeva

A thesis submitted in fulfilment of the requirements for the degree of Doctor of Philosophy

December 13, 2018

Abstract

The electrochemical gradient of protons, or proton motive force (PMF), is at the heart of bacterial energetics. It consists of two components: the pH difference between a cell cytoplasm and the environment, and the membrane potential. The PMF powers such vital cellular processes as ATP production, motility and active membrane transport.

The aim of this doctoral project was to relate the changes in the physiological state of the cell to the PMF in a variety of stressful environments and, using this, uncover the mechanisms through which these stresses induce cellular damage. In this thesis I have shown that by modelling an *Escherichia coli* cell as an electric circuit, the relationship between bacterial PMF, the electric properties of the cell membrane and the catabolism can be described mathematically. Subsequently, using the bacterial flagellar motor (BFM) as a single-cell "voltmeter" I have quantitatively described the effects of different stresses on the maintenance of cellular free energy. To achieve my goal I developed an assay for simultaneous monitoring of the PMF and the intracellular pH by using a combination of fluorescence and back-focal-plane (BFP) interferometry techniques. I confirmed the accuracy of the proposed approach by applying it to a known stress — indole treatment — and recovering the previously shown functional dependency between indole concentration and the membrane conductance. I then tested a variety of different stresses and found that butanol acts as an ionophore changing membrane conductance linearly with concentration and functionally characterised membrane damage caused by light of shorter wavelengths. I further proved that this light damage was mediated by reactive oxygen species by repeating light damage experiments in anaerobic conditions. Anaerobic conditions were also used for studying an acid challenge response where I demonstrated that the presence of oxygen is required for the maintenance of the cytoplasmic pH.

Additionally, in the course of my project I tested and characterised several pH indicators. I demonstrated that the cpYFP sensor, previously used in eukaryotic cells, could be successfully used in *E. coli* to allow the internal pH measurements in the higher pH range, while the pHRed sensor was shown to form the aggregates in the cell cytoplasm and, consequently, to slow down the growth. The optimal protocol of the pH sensors calibration was established

and several calibration-related issues discussed.

Finally, I revisited the experiments that demonstrate the PMF and BFM speed proportionality. I found that under high load the motor speed saturates with PMF disproving the currently accepted idea of the PMF-motor speed linear relationship holding irrespective of the motor load. I proposed the possible explanation of the observed phenomenon and discussed potential experiments that could test my hypotheses.

Declaration

I declare that this thesis was composed by myself, that the work contained herein is my own except where explicitly stated otherwise in the text, and that this work has not been submitted for any other degree or professional qualification.

Ekaterina Krasnopeeva
December 13, 2018

Acknowledgements

Most of all, I'd like to thank Dr Teuta Pilizota for being a great supervisor. It's been a pleasure, an honour and a lot of fun to work with you. Your guidance, support, encouragement and overwhelming (even too overwhelming sometimes) enthusiasm helped me a great deal to become who I am now.

I'd like to thank all the members of the TP group for many many things but, most importantly, for creating a great atmosphere in the lab, making it enjoyable to come to work every day, even the gloomiest one. Special thanks to Dr Alex McVey and Dr Jerko Rosko for helping me with the writing.

I would also like to thank Dr Bartek Waclaw, Dr Peter Swain, Dr Vincent Martinez, Dr Jana Schwarz-Linek and Dr Chien-Jung Lo.

Lastly, I want to thank my friends and family, especially my husband, Dr-to-be Ivan Maryshev, for making me happy.

"The important thing in science is not so much to obtain new facts as to discover new ways of thinking about them."

Sir William Lawrence Bragg

" Одно число всегда равно другому с точностью до численного множителя. Поэтому любой эксперимент подтверждает любую теорию."

А. Кондратьев

Contents

Chapter 1

Introduction

1.1 Bacterial energetics

It is hard to think of a good definition of life. According to the Oxford English Dictionary it is "the condition that distinguishes animals and plants from inorganic matter, including the capacity for growth, reproduction, functional activity, and continual change preceding death." However, growth and self-reproduction are sometimes observed in inorganic chemical ensembles (Li et al., 2014), simple mechanical devices can perform functional activity, and the concept of death is even more controversial than life itself. A physicist could say that one of the defining features of life is its ability to maintain a displacement from thermodynamic equilibrium (which in this case would be called "death"). Indeed, life constantly produces, stores and uses up energy trying to sustain its core features, including those listed in the Oxford Dictionary. To understand the general laws that these energy fluxes obey, let us consider a living cell from the point of view of thermodynamics.

1.1.1 Thermodynamics of the living systems

Thermodynamics classifies all possible systems based on their degree of isolation. There are three types of systems: isolated, closed and open. An isolated system is an ensemble of N objects enclosed in a well-defined volume V, which exchanges neither energy nor matter with the space outside of the V. The statistical postulate of equilibrium affirms that any isolated system spontaneously evolves towards the state of thermodynamic equilibrium characterised by the

fact that there is no differences in the states of its subsystems, and its macroscopic parameters are constant. In an isolated system processes are driven by an increase of the entropy (or, roughly speaking, a degree of disorder). A closed system is capable of exchanging energy but not matter across its boundaries. Any closed system can be considered as a subsystem of a bigger isolated system, such as the universe itself, that obeys the increase in entropy principle. Thus, the processes in the closed system can occur when the total entropy (the system in question plus its surroundings) increases.

To describe the thermodynamic state of a system physics uses the thermodynamic potentials — scalar functions of the temperature (T), pressure (p), volume (V), entropy (S), the number of particles in the system (N_i) and the chemical potential for an i-type particle (μ_i) (Duhem, 1886). Most commonly, four thermodynamic potentials are used: internal energy $U(S, V, N_i)$, enthalpy $H(S, p, N_i)$ Helmholtz free energy $F(T, V, N_i)$ and Gibbs free energy $G(T, p, N_i)$, expressed as (1.1).

$$\begin{aligned}
\Delta U &= T\Delta S - p\Delta V + \sum_i \mu_i \Delta N_i, \\
\Delta H &= \Delta(U + pV) = T\Delta S + V\Delta p + \sum_i \mu_i \Delta N_i, \\
\Delta F &= \Delta(U - TS) = -S\Delta T - p\Delta V + \sum_i \mu_i \Delta N_i, \\
\Delta G &= \Delta(U - TS + pV) = -S\Delta T + V\Delta p + \sum_i \mu_i \Delta N_i
\end{aligned} \tag{1.1}$$

At constant pressure and temperature it is the most convenient to use Gibbs free energy (that can be re-written as $\Delta G = \Delta H - T\Delta S$) to calculate the change in the total entropy via the enthalpy flow across the boundary. The change in the free energy of a closed system and its surroundings is a measure of the net driving force for a process. In order for a process to occur spontaneously it has to result in a negative ΔG, in which case the total entropy of the universe increases.

The most complex systems to describe are the open systems, which can exchange both energy and matter with the surroundings, making equilibrium thermodynamics inapplicable. All biological systems are open in a thermodynamic sense, and only reach true equilibrium upon death. It is, however, possible to apply the laws of equilibrium thermodynamics to a living system

by considering individual reactions, or group of reactions, occurring in an organism (such as catabolism or biosynthesis) as closed systems, where matter is conserved (Nicholls et al., 1992; Cleri, 2016). This simplification allows us to use Gibbs free energy and other thermodynamic potentials to mathematically describe the state of the biological system.

1.1.2 Reaction coupling

If we consider the processes in a living cell thermodynamically as described above, we'll learn that most of the essential reactions, such as synthesis of the biological molecules, active transport across the membrane, motility, etc., result in a $\Delta G > 0$. For these reactions to occur, they must be coupled with the energetically favourable ones to lower the total ΔG of the combined reactions below zero. An example of the energetically favourable reaction most commonly used for the coupling is adenosine triphosphate (ATP) hydrolysis. ATP is a nucleoside triphosphate which, as far as we know, is used as the primary energy currency by all living organisms, from the simplest bacteria to humans. ATP consists of adenosine and three phosphate groups. Energy is released from the ATP molecule upon hydrolysis of the anhydride bounds. Resulting products of this reaction are adenosine diphosphate (ADP) and inorganic phosphate (P_i). The equilibrium constant of this reaction is 10^5 M, which means that for a system in equilibrium for P_i and ADP concentrations being 10^{-2} M of and 10^{-3} M respectively ATP concentration would be as little as 10^{-10} M. A living cell is a system outside of equilibrium and is capable of maintaining the ratio of ATP to ADP at a point almost ten orders of magnitude from equilibrium, with ATP concentration fivefold higher than the concentration of ADP (Atkinson et al., 1967). This displacement from equilibrium means that the hydrolysis of ATP in the cell releases a large amount of free energy, which allows ATP to be a cofactor for a huge number of reactions in the cell (Nicholls et al., 1992). B. Alberts *et al.* in their canonical textbook "The molecular biology of the cell" (Alberts et al., 1994) give a simple and powerful illustration for the reaction coupling (Fig. 1.1). In their analogy the energy stored in the ATP molecule is represented by the elevated bucket of water, which then can be used for enabling a wide variety of the chemical reactions unable to occur otherwise.

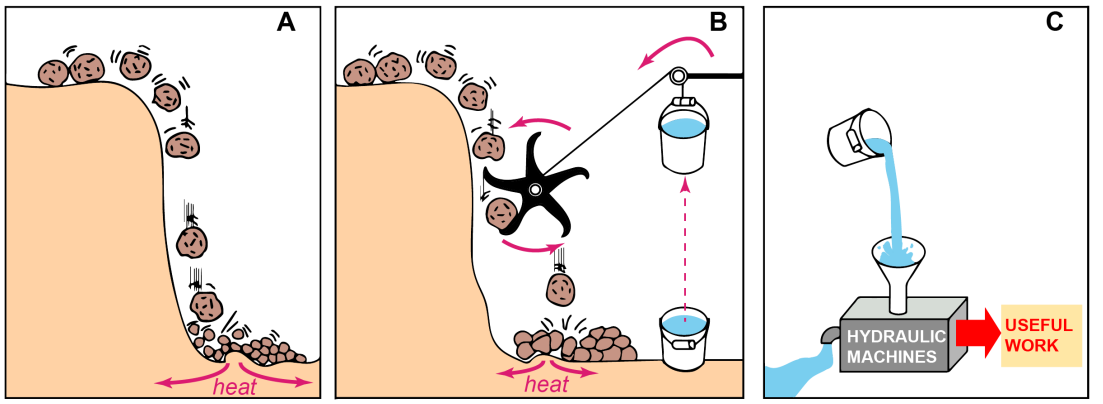

Kinetic energy transformed into heat energy only

Part of the kinetic energy is used to lift a bucket of water, and a correspondingly smaller amount is transformed into heat

The potential energy stored in the elevated bucket of water can be used to drive hydraulic machines

FIGURE 1.1: A mechanical model illustrating the principle of coupled chemical reactions. The spontaneous reaction shown in (**A**) might serve as an analogy for the direct oxidation of glucose to CO_2 and H_2O, which produces heat only. In (**B**) the same reaction is coupled to a second reaction; the second reaction might serve as an analogy for the synthesis of ATP. The more versatile form of energy produced in (**B**) can be used to drive other cellular processes, as in (**C**). ATP is the most versatile form of energy in cells. Figure and caption are from (Alberts et al., 1994).

1.1.3 Catabolism and ATP synthesis

To use ATP as a "universal energy currency" a cell first needs to synthesise it. Being a reverse reaction of ATP hydrolysis, ATP synthesis yields $\Delta G > 0$ and requires an energy input. This input is represented in Fig. 1.1 by falling rocks giving part of their potential energy to the elevating of the bucket. In a living organism the role of falling rocks is played by the food catabolism. Fig. 1.2 shows a simplified diagram of the catabolism that holds for all non-photosynthesising organisms. It can be considered as a three-stage process:

- Stage 1. Large compounds are broken down into simple molecules. This stage is mostly relevant for higher order organisms capable of digesting complex food and produces no ATP.

- Stage 2. Glycolysis and breakdown of simple molecules to acetyl coenzyme A (acetyl CoA). A small amount of ATP (2 ATP molecules per 1 glucose molecule) is generated via substrate-level phosphorylation.

- Stage 3. The Citric Acid cycle (also known as tricarboxylic acid cycle, Krebs cycle, or TCA) where the acetyl CoA is completely degraded to

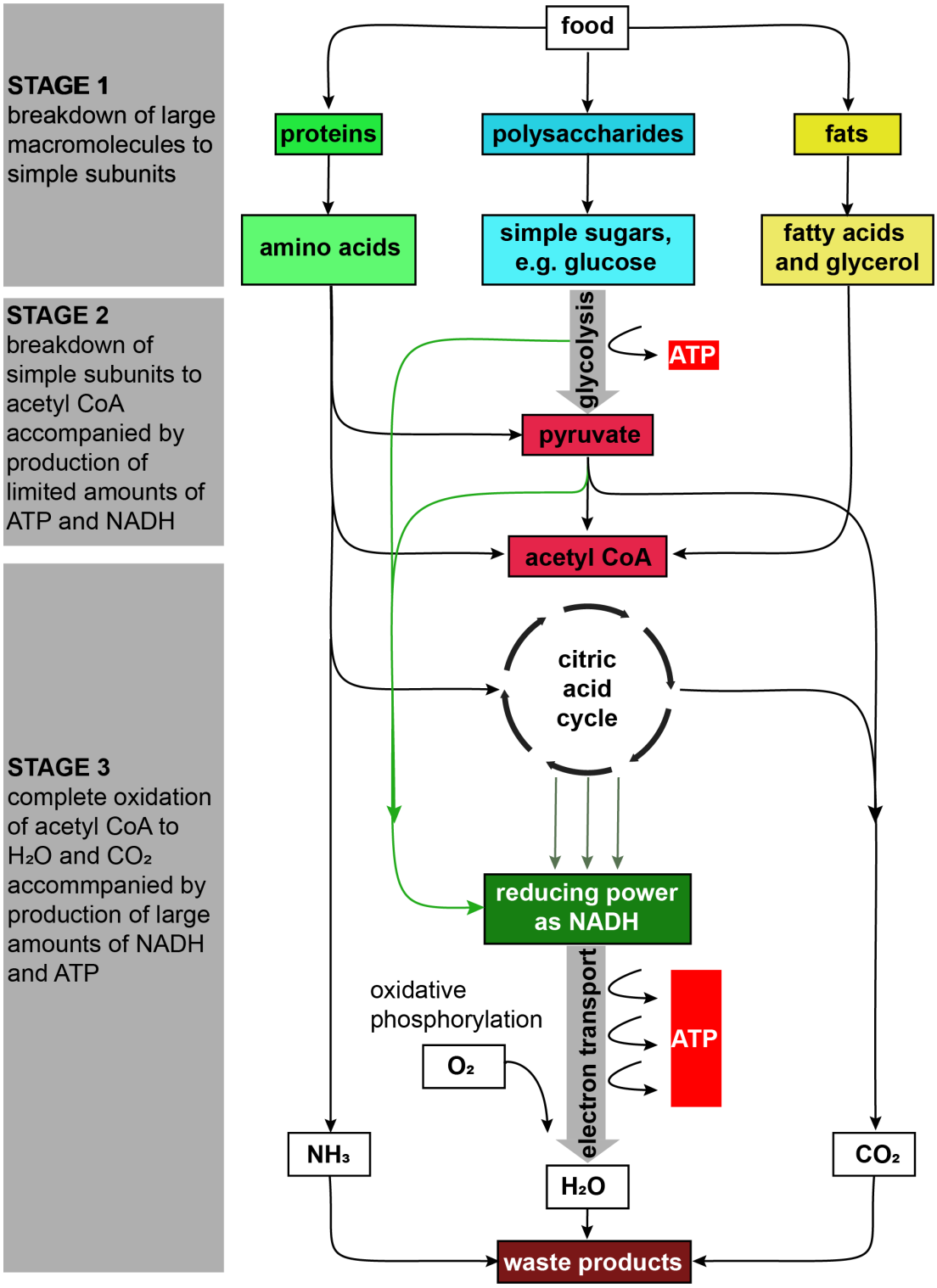

FIGURE 1.2: Simplified diagram of the three stages of catabolism that lead from food to waste products. This series of reactions produces ATP which is then used to drive biosynthetic reactions and other energy-requiring processes in the cell. Figure and caption are from (Alberts et al., 1994).

CO_2 and H_2O and oxidative phosphorylation results in a large amount of ATP production ($\sim$30 ATP molecules per 1 molecule of glucose (Berg et al., 2002))

Let us consider the last stage in more details. The illustration of the process is shown in Fig. 1.3. Acetyl groups from acetyl CoA are covalently added to the oxalacetate to form a citrate molecule. In a series of the enzymatically catalysed reactions two of the six carbon atoms are released in the form of two CO_2 molecules and the rest are used to regenerate an oxalacetate molecule at the end of each cycle. Apart from the CO_2 molecules cycle yields in 1 ATP, 3 NADH and 1 $FADH_2$ molecules. One molecule of glucose is broken down to two pyruvates and, consequently, can power up two rounds of the TCA cycle. Hence, after undergoing the glycolysis and two TCA cycles each glucose molecule brings 4 ATP (2 in glycolysis + 1 per each TCA cycle), 10 NADH (4 in glycolysis + 3 per each TCA cycle) and 2 $FADH_2$ (1 per each TCA cycle). NADH and $FADH_2$ molecules thus formed then enter the electron transport chain (TCA), where $\sim$30 more ATP molecules are produced as a result of the oxidative phosphorylation.

NADH and $FADH_2$ play a role of the protons and electrons carriers. By entering the ETC they transfer the electrons to its final acceptor, oxygen, in a series of consequent oxidation reactions. The energy released in these reactions is used to pump protons out through the inner membrane of a bacterium or a mitochondrion. This results in a formation of an electrochemical gradient of protons across the membrane, which is referred to as a proton motive force, or PMF (Mitchell, 1961). The PMF then powers up the ATP production by the F_1F_o ATP synthase. The ATP synthase allows the passive flux of protons across the membrane down their electrochemical gradient and uses the energy released by the transport reaction to form ATP. The ATP synthesis can be reversed if necessary to restore the proton gradient.

1.1.4 Proton motive force

The PMF accumulated during the third stage of the catabolism as a result of the electron transport chain activity is another key intermediate in biological energy conversion. In addition to being employed in ATP synthesis, it's also used by various membrane bound proteins to drive the transport of sugars, amino acids and other substrates across biological membranes (Mitchell, 1961;

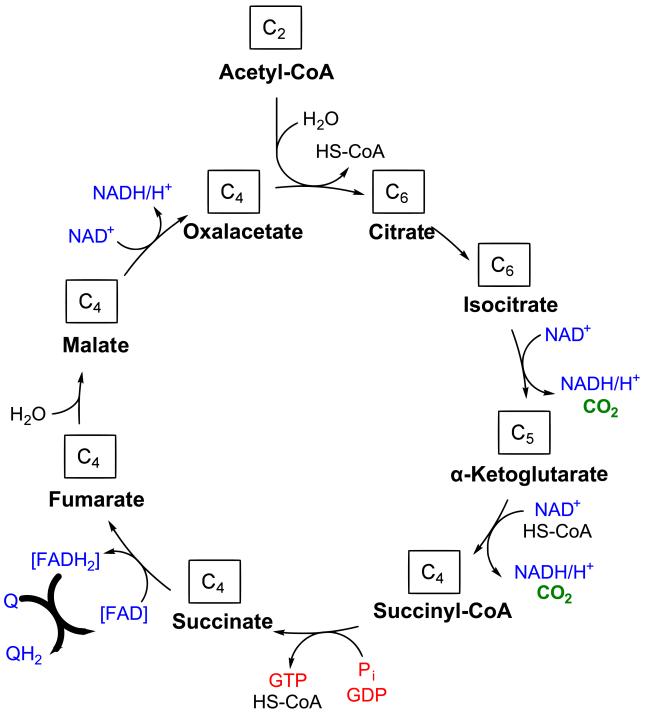

FIGURE 1.3: In aerobic bacteria acetyl CoA is produced from the pyruvate and enters the citric acid cycle where it gets further oxidised. The carbon atoms of the acetyl groups are converted to the CO_2 and the hydrogen atoms are transferred to the carrier molecules NAD^+ and FAD. The number of carbon atoms at each step of the cycle is shown in boxes.

Nicholls et al., 1992) and powers up bacterial motility (Manson et al., 1980; Matsuura et al., 1977; Meister et al., 1987; Fung et al., 1995), Fig. 1.4.

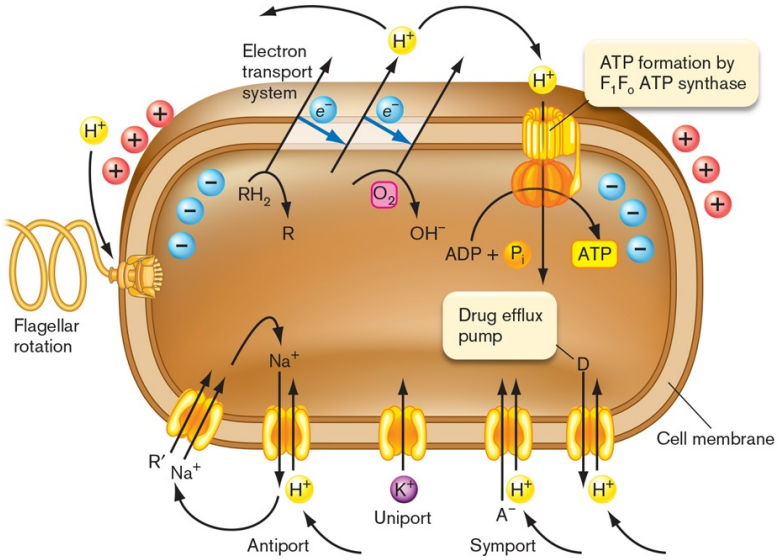

FIGURE 1.4: Processes driven by proton motive force. Processes powered by proton potential include ATP synthesis through the F_1F_o ATP synthase, flagellar rotation, uptake of nutrients, and efflux of toxic drugs. "R" refers to an organic nutrient. Figure and caption are from (Slonczewski et al., 2017).

There are two forces acting on the protons separated by the membrane: one arises from the difference in proton concentrations in the inner and outer compartments of the cell, and the other is due to the electrostatic potential across the membrane. In the absence of the membrane potential (V_m=0) the ΔG released from the translocation of 1 mol of protons down the concentration gradient (from the outside to the inside of the cell) is given by:

$$\Delta G = RTln\frac{[H^+]_{in}}{[H^+]_{out}}, \tag{1.2}$$

where R is a gas constant, T is temperature, $[H^+]$ is a concentration of protons and ΔG is in kJ·mol^{-1}.

The other extreme case, the translocation of 1 mol of protons down an electrical potential in the absence of the concentration gradient, results in a free energy change:

$$\Delta G = FV_m, \tag{1.3}$$

where F is the Faraday constant.

The forces are additive and in the general case of non-zero concentration gradient and membrane potential ΔG becomes:

$$\Delta G = FV_m + RT \ln \frac{[H^+]_{in}}{[H^+]_{out}}, \tag{1.4}$$

The concept of the proton motive force was introduced by Peter Mitchell in his chemiosmotic hypothesis (Mitchell, 1961). This hypothesis was the first to suggest that the electrochemical gradient of the protons was required for ATP synthesis. Mitchell defined proton motive force as $PMF = -\Delta G_{H^+}/F$. Combining (1.4) with the conventional measure of the proton concentration ($pH = -log_{10}[H^+]$) we get the expression for the proton motive force:

$$PMF = -V_m + 2.303\frac{RT}{F}\Delta pH, \tag{1.5}$$

where $\Delta pH = pH_{in} - pH_{out}$. In the literature PMF is often used with the negative sign for better comparison with the negative membrane potential, in this case it's defined as $PMF = V_m - 2.303\frac{RT}{F}\Delta pH$. We will use this definition in Chapter 4 where PMF and V_m are used interchangeably. We have thus established that the proton motive force is a potential acting on the proton gradient across the cell membrane, which comprises the contributions of the concentration and electric charge differences between membrane separated compartments.

1.2 Measurements of the bacterial energetics

The major sources of the readily available free energy in the cell are ATP and PMF. The ability to measure these parameters can lead to an understanding of the fundamental features of the cell operation. Scientists have been searching for the best and most reliable techniques of the energetics components measurements for decades. In the following section I provide a brief overview of the existing methods of ATP and PMF measurements available today.

1.2.1 *In vivo* ATP measurements

Early methods of ATP measurement focused on obtaining hydrolysable phosphorus from blood samples to calculate ATP content in the blood of various living species (Fiske, 1934; Kerb et al., 1935). However, these measurements

required long preparation times and large sample volumes. As long ago as 1947 a breakthrough in ATP quantification techniques was made by William McElroy who demonstrated that firefly bioluminescence is powered by ATP (McElroy, 1947). This finding made it possible to correlate the luciferin glowing parameters (time and intensity) and amount of ATP. Assays based on the firefly luciferase have been widely used since for ATP quantification (Cole et al., 1967; Ford et al., 1996) and are now commercially available. The main advantage of the method is the fact that luminescence assay does not require excitation with the light, which makes the issues with phototoxicity and bleaching, typical to the fluorescence measurements, irrelevant. Nonetheless there are a few drawbacks associated with this method. The luminescence can be quite dim and is not always suitable for single-cell measurements and its intensity does not depend on the ATP level solely but also on the luciferase and its substrates concentration. Additionally, luciferase activity is sensitive to pH. Alternative methods based on the genetically encoded fluorescent sensors have recently been developed by H. Imamura *et al.* (Imamura et al., 2009; Yaginuma et al., 2014) and named QUEEN and ATeam. Both probes employ bacterial F_1F_o ATP synthase ϵ subunit, which has high affinity to ATP and significantly changes confirmation upon ATP binding (Iino et al., 2005; Yagi et al., 2007). ATeam method of action is based on Förster resonance energy transfer (FRET). The ϵ subunit is sandwiched by the variants of cyan and yellow fluorescent proteins (CFP and YFP) separating them in the extended confirmation and bringing them close to each other in the folded ATP-bound state thus changing FRET efficiency (Fig. 1.5A). However, the group later reported an issue related to the fact that the two fluorescent proteins maturated at different rates changing FRET efficiency independently of ATP concentration and proposed an alternative sensor, QUEEN, based on a single fluorescent protein (Yaginuma et al., 2014). The QUEEN sensor has a circularly-permuted enhanced green fluorescent protein (cpEGFP) inserted between two α-helixes of F_1F_o ϵ subunit (Fig. 1.5B). Upon ATP binding the change in a protein confirmation causes a change in QUEEN's fluorescence spectrum.

Additionally, it is possible to measure ADP:ATP ratio with another fluorescent reporter, Perceval, based on the competitive binding of ADP and ATP to the probe (Berg et al., 2009; Tantama et al., 2013). Perceval is engineered as a fusion of the yellow fluorescent, circularly permuted monomeric Venus (cpmVenus) and GlnK1 proteins. GlnK1 is a trimeric intracellular protein that

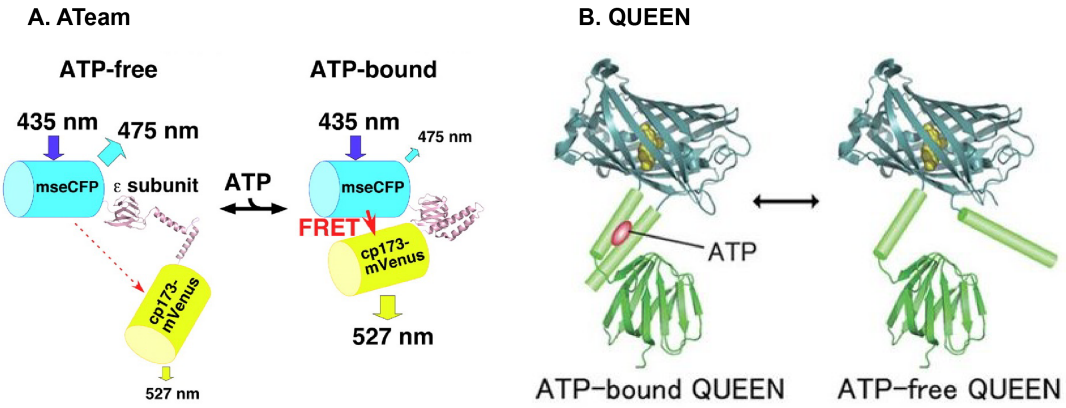

FIGURE 1.5: Genetically encoded fluorescent ATP sensors ATeam (**A**) and QUEEN (**B**). (**A**) Schematic drawing of AT1.03 probe. Variants of CFP (mseCFP) and YFP (cp173-mVenus) were connected by the ϵ subunit of *Bacillus subtilis* F_oF_1-ATP synthase. In the ATP-free form (left), extended and flexible conformations of the ϵ subunit separate the two fluorescent proteins, resulting in low FRET efficiency. In the ATP-bound form, the ϵ subunit retracts to draw the two fluorescent proteins close to each other, which increases FRET efficiency. Figure and caption are from (Imamura et al., 2009). (**B**) Schematic illustration of the ATP sensing mechanism of QUEEN. Figure and caption are from (Yaginuma et al., 2014).

regulates ammonia transport associated with the synthesis of glutamine and has an affinity to both ATP and ADP. The binding to ATP (but not ADP) results in a dramatic conformational change of the GlnK1 protein, which leads to a change in Perceval's fluorescence spectrum. At the physiological ATP concentration Perceval sensitivity capacity is saturated, however the competitive binding of ADP allows one to use it as an ADP:ATP ratio sensor.

1.2.2 *In vivo* PMF measurements

Proton motive force is a sum of two components: membrane voltage and the pH difference between the cytoplasm and the external environment. Thus, it is possible to measure PMF indirectly by separately probing each of its components (Zilberstein et al., 1984; Kashket, 1985).

To calculate ΔpH one needs to know the values of both extra- and intracellular pH. For simplicity I do not consider here cell surface charge and the local pH changes but assume that the external pH is simply equal to the pH of the environment. While the environment pH can be calculated based on the chemical composition of the solution, measured with a pH meter or indicator paper

and adjusted to the desired value, the intracellular pH is not that easily manipulated. There are various techniques enabling cytoplasmic pH measurements. In Chapter 3 I give an overview of these techniques and in detail discuss the use of genetically encoded ratiometric pH sensors in *E. coli*.

The history of membrane voltage (V_m) measurements began with a famous work by Hodgkin and Huxley on the giant axon of a squid (Hodgkin et al., 1939). The field was further expanded to smaller neuron cells (Ling et al., 1949). These early works were based on the direct measurements of the potential with the microelectrodes filled with the conductive solution. Since then the patch clamp technique has become an important tool in studying the excitable cell systems such as neurons or cardiomyocytes (Hodgkin et al., 1952; Richardson et al., 2010). In the case of bacteria with their small size, the patch clump becomes applicable only when the cells are artificially enlarged and the cell envelope is removed (Ruthe et al., 1985; Martinac et al., 1987). Other methods of the V_m measurement include membrane-bound probes that change their optical properties due to the potential change, or freely moving Nernstian dyes that accumulate in the cell according to the Nernst potential (Ehrenberg et al., 1988; Prindle et al., 2015; Kralj et al., 2011; Peterka et al., 2011). An example of membrane-bound probe in *E. coli* is a PROPS sensor (Kralj et al., 2011), where the protein acts as a reversed green-absorbing proteorhodopsin using V_m to induce a color shift. The Nernstian probes used in bacteria include rhodamine 123, positively charged carbocyanines such as 3,3- dihexyloxacarbocyanine iodide ($DiOC_6(3)$), 3,3-diethyloxacarbocyanine iodide ($DiOC_2(3)$), and 3,3'-dipropylthiadicarbocyanine iodide ($DiSC_3(5)$, Thioflavin T (ThT), tetramethylrhodamine (TMRM), and the negatively charged bis-(1,3-dibutylbarbituric acid) trimethine oxonol ($DiBAC_4(3)$) (Lo et al., 2007; Breeuwer et al., 2004; Prindle et al., 2015).

To be used as a voltage sensor a Nernstian probe has to meet the following requirements: it should (i) freely diffuse across the cell membrane, (ii) not bind to the membrane or other cellular components, (iii) be biologically inert (i.e. should not be metabolised by the cell or be toxic) and (iv) be detectable at sufficiently low concentrations (Lolkema et al., 1982). The correct use of the Nernstian dyes for the V_m measurements in bacteria is being discussed in a soon-to-be-published work by Mancini *et al*. The authors show that there is a trade-off between the probe's fluorescence intensity and its toxicity, originating from the fact that positively charged dye molecules neutralise the membrane

potential, leading to a complete membrane depolarisation at high concentrations, and the consequent cell death (Mancini et al., 2018).

1.3 Bacterial flagellar motor for PMF measurements

The alternative way of measuring proton motive force is via changes in bacterial flagellar motor rotational speed. As mentioned before, the motor rotation in *E. coli* is powered by the PMF. The rotation speed is proportional to the PMF value ((Fung et al., 1995; Gabel et al., 2003) and Chapter 5), which makes flagellar motor a good indicator of the total PMF in *E. coli*.

1.3.1 Bacterial swimming

E. coli is a motile bacterial species that swims by propelling itself through the environment with the rotating flagellar filament bundle (Berg et al., 1973). Each flagellum consists of the long thin helical filament (10 μm x 20 nm) attached to a rotary motor with a flexible hook (Sowa et al., 2008). Bacteria move by performing a random walk consisting of periods of running and tumbling (Berg et al., 1972). The "running" mode corresponds to the case when all 6-8 flagella rotate counter-clockwise (CCW, viewed from filament to motor) and form a stable bundle. The bundle falls apart if one or more flagella switches its rotation to clockwise (CW), which leads to the cell tumbling and changing its swimming direction (Turner et al., 2000). The length of running and tumbling intervals (equivalent to the CCW and CW motor rotation periods) is regulated by the chemotactic system in bacteria. This system is required to navigate bacteria in the liquid environment towards the nutrients and away from toxins (Adler, 1975). An example of an *E.coli* cell with fluorescently labelled filaments performing the random walk is given in Fig. 1.6.

1.3.2 Flagellar motor structure

The filaments are put in motion by the unique example of a naturally occurring nano-machine —- rotary bacterial flagellar motor (BFM). A schematic of the BFM structure in comparison to a cryo-EM reconstruction is given in Fig. 1.7. The basal body of the motor consists of several protein rings that protrude

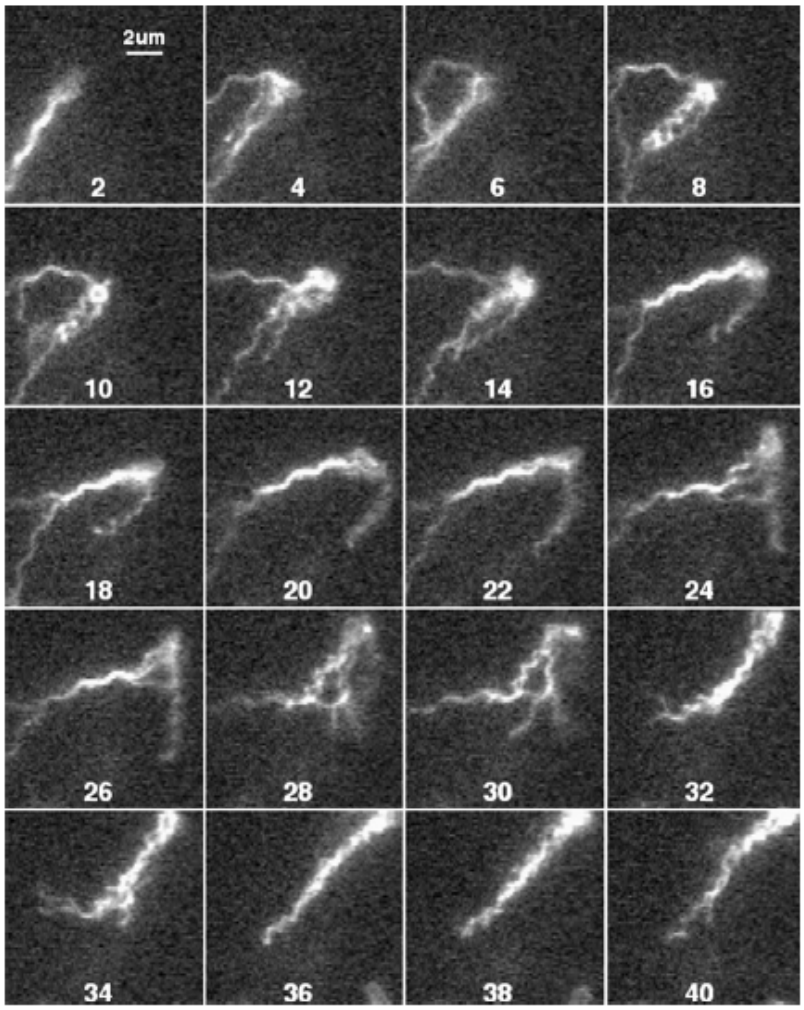

FIGURE 1.6: *E. coli* cell with a normal bundle that transforms to a mixed waveform, where again filaments leave and rejoin the bundle. Every other field is shown, the frame numbers are shown in each figure. Figure and caption are from (Turner et al., 2000).

through both the inner and the outer cell membranes as well as through the cell wall (Berg, 2003; Sowa et al., 2008; Nirody et al., 2017). BFM, like the macroscopic motor, has a rotor and a stator. The rotor consists of the cytoplasmic (C) and the membranous/supramembranous (MS) rings. Its rotation is driven by the stator, consisting of a varying number of MotA/MotB units (Kojima et al., 2004; Reid et al., 2006; Lele et al., 2013; Tipping et al., 2013; Nord et al., 2017). The L and P rings are thought to be embedded in the outer lipopolysaccharide membrane and peptidoglycan cell wall respectively, however it's not known whether they rotate relative to the cell envelope (Sowa et al., 2008; Nirody et al., 2017).

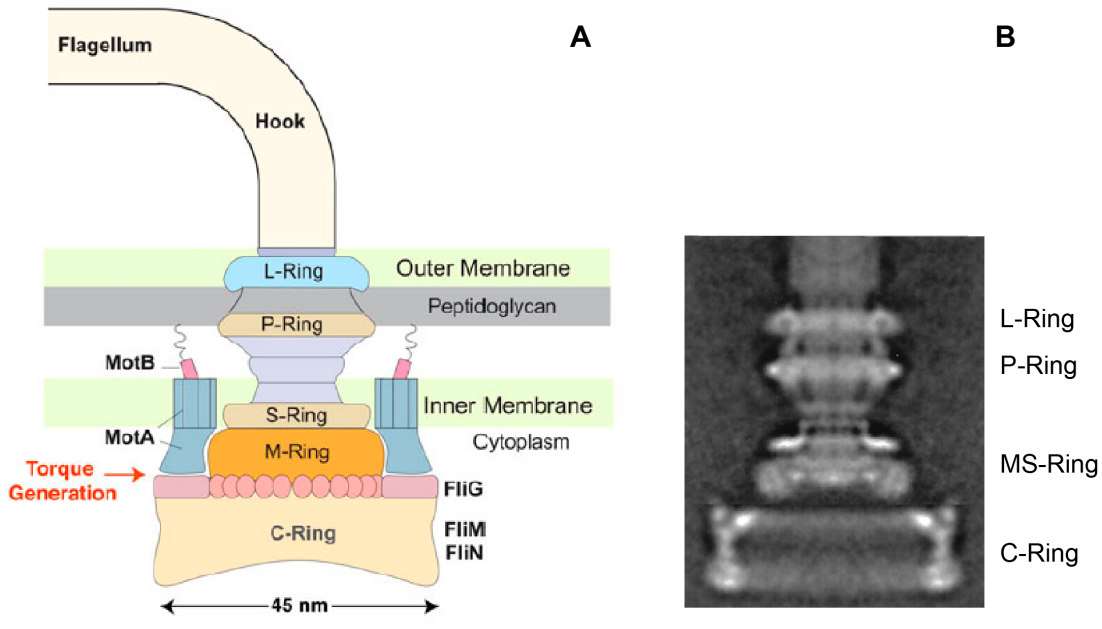

FIGURE 1.7: A schematic diagram of the flagellar motor compared to a rotationally averaged reconstruction of images of hook-basal bodies seen in an electron microscope. (**A**) Rotation of a bacterium's flagellum is driven by a rotary motor attached to its base by a flexible hook. The rings of the flagellar motor's basal body are called the rotor. FliG proteins are placed around the periphery of the rotor's C-ring. These interact with the loops of the stator-units to generate torque and rotate the flagellum. Each stator unit is composed of MotA and MotB proteins, the latter of which attaches the stator to the peptidoglycan layer, allowing for torque generation via the MotA–FliG interaction. A motor maintains up to 11 engaged stator units, depending on the load. Figure and caption are from (Nirody et al., 2017). (**B**) The general morphological features are C-ring, MS-ring, P-ring, L-ring, hook, hook-associated proteins (which include the distal cap), and filament. MotA, MotB, and components of the transport apparatus do not survive extraction with detergent and, therefore, are not shown. This reconstruction is derived from rotationally averaged images of about 100 hook–basal body complexes of *Salmonella* polyhook strain SJW880 embedded in vitreous ice (Francis et al., 1994). The radial densities have been projected from front to back along the line of view, so this is what would be seen if one were able to look through the spinning structure. Connections between the C-ring and the rest of the structure appear relatively tenuous. Figure and caption are adapted from (Berg, 2003).

The torque generation by the stator is powered by the ion motive force arising from the transit of ions (protons in the case of *E. coli* or *S. typhimurium*, or sodium for *Vibrio alginolyticus* and *Vibrio cholera*) across the cellular membrane.

The rotational frequency of the *E. coli* motor has been shown to be linearly dependent of the PMF up to 150 mV and independently of the stator unit number and the external load (Fung et al., 1995; Gabel et al., 2003). The applicability and origins of this linear relationship is a topic of a more detailed discussion in Chapter 5.

1.3.3 Motor speed measurements

Since the motor speed is proportional to the PMF it can be used as an indicator of the total PMF as an alternative to the methods discussed above. There are several ways to measure the speed of the BFM that I will consider here (Fig. 1.8).

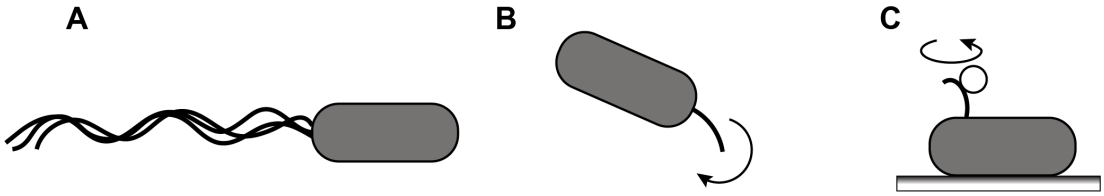

FIGURE 1.8: Methods of BFM speed measurements with swimming bacteria (**A**), tethered cells (**B**) or a bead attached to a flagellum (**C**).

Swimming speed

The relationship between the swimming speed of a bacterium and the rotational speed of the motor has been shown to be roughly linear (Magariyama et al., 1995; Magariyama et al., 2001), which makes the swimming speed of bacteria an equivalent PMF indicator. It is possible to track single bacteria (Berg, 1971; Liu et al., 2014; Taute et al., 2015) or consider the averaged speed of the population (Wilson et al., 2011; Martinez et al., 2012b). The biggest advantage of these methods is the fact that they do not require any special preparation of the bacterial culture. It is however not possible to quickly exchange the media in the tracking system when bacteria are not attached. This means that the method is only applicable for steady or slowly changing conditions and cannot be used for studying rapidly changing environments (e.g. an osmotic shock). The method also requires a differentiation of running and tumbling modes, which in the case of the population measurements presents a challenge.

Tethered cells

Tethered cells were used to confirm the prediction that the movement of flagella was indeed a rotation and not a propagation of the helical waves (Berg et al., 1973; Silverman et al., 1974). In this experiment cells were attached to the glass coverslip by a flagellum to demonstrate the motor-driven rotation of the cell body relative to the attachment point. The tethered cells were further used for investigation of the torque-speed relation of the BFM (Meister et al., 1987) and for the demonstration of speed proportionality between fast and slow motors and the PMF (Gabel et al., 2003). While preparation of the cell culture for the tethered cell experiment is quite straightforward, it does not allow the control of the attachment geometry. This, together with the inhomogeneity of cell sizes, causes deviations in the effective load on the motor and results in the huge spread of rotational speeds seen by Gabel and Berg (Gabel et al., 2003). Additionally, the speed of the tethered cells does not exceed a few hertz (Meister et al., 1987; Fung et al., 1995; Gabel et al., 2003) due to the high motor load, which compromises the sensitivity of the method.

Bead attached to a flagellum

To obtain higher rotational speeds and gain better control of the load on the motor, it has been suggested to use polystyrene beads as markers for a motor rotation (Silverman et al., 1974). However, it was quite difficult to achieve a good attachment of the bead to a flagellum. The issue was resolved when the "sticky" filament phenotype was obtained in 1988 as a by-product of experiments aimed to acquire a minimum-size functional flagellum (Kuwajima, 1988). The bead assay has since become a well established tool for studying BFM (Ryu et al., 2000; Berg et al., 1993; Chen et al., 2000; Sowa et al., 2008; Nirody et al., 2017). The speed of the bead can be measured with high speed cameras (Nord et al., 2017), or using back-focal-plane (BFP) interferometry (Rosko et al., 2017; Lo et al., 2013; Tipping et al., 2013; Bai et al., 2010), described in "Materials and Methods" (Section 2.4). BFP interferometry provides high resolution (up to 0.5 ms (Pilizota et al., 2007)) whilst permitting rapid media exchange (Rosko et al., 2017). However, it is only possible to target a single motor per experiment, thus the throughput is very low.

1.4 Thesis motivation and overview

The work presented in this thesis is a part of a bigger project aimed at understanding the free energy coordination of *E. coli* in a variable environment. Groups from three different Universities (The University of Edinburgh, UK; Peking University, China; and National Central University, Taiwan) are working in collaboration to develop a biophysical single-cell assay for the direct measurements of the PMF and ATP dynamics under stress conditions. The project aims to uncover the fundamental principles behind the preservation of free energy, explore the possibility of the existence of universal mechanisms of free energy coordination under stressed conditions, and to offer an operational definition of "dead" and "alive" grounded in the biophysics of free energy flows.

In this thesis I focus on measurements of the two components of the cellular energetics: the proton motive force and the ΔpH.

The thesis opens with the "Materials and Methods" section (Chapter 2) introducing the techniques developed and used in the project. These include the molecular biology methods for the construction of the *E.coli* strains as well as the steps required for alignment of a custom-made microscope and all experimental protocols.

Chapter 3 focuses on single-cell measurements of the internal pH of *E. coli*. The Chapter includes an overview of the history of pH measurements and existing techniques, the characterisation of the several genetically encoded fluorescent pH sensors and a discussion of the issues related to their calibration.

In Chapter 4 I combine internal pH measurements with the PMF measurements in order to obtain an electrochemical profile of an *E. coli* cell under various stresses. Making an analogy between a bacterial cell and electric circuit, I use this mathematical framework to relate the stress amplitude and the change in the cell's physiology. I apply this approach to a range of different stresses to uncover the nature of the damage induced by each stress.

In addition, in Chapter 5 I re-visit the PMF-motor speed relation and find its limitations. I show that the motor speed fails to stay proportional to the PMF when the load on the motor is large and the PMF high. The current understanding of the BFM operation is not enough to explain this phenomena and I therefore propose the alternative hypotheses and outline future experiments to test them.

I conclude this thesis with Chapter 6 where I sum up the main results obtained in this work and give an overview of the potential future directions.

Chapter 2

Materials and Methods

2.1 Strains construction

2.1.1 List of strains and plasmids

For simultaneous PMF and intracellular pH measurements a number of strains have been constructed. Plasmids and strains used in this work are listed in Tables 2.1 and 2.2 respectively. List of the primers used for the strains construction can be found in Table A.1.

TABLE 2.1: List of plasmids used in this work.

Plasmid name	Features	Source
pFD313	amp^R, pBR322 (Bolivar et al., 1977) based plasmid which contains a deletion of 171 nucleotides in the central region of *fliC*	(Kuwajima, 1988)
pkk223-3-pHluorin	amp^R, pkk223-3 (Brosius et al., 1984) based plasmid which contains *pHluorin*(M153R) gene	(Morimoto et al., 2011)
pTOF24	cm^R, kan^R, levansucrase encoding *sacB*, temperature sensitive replication initiator protein $repA^{ts}$	(Merlin et al., 2002)
pTOF-fliC^{sticky}	cm^R, pTOF24 derivative, kan^R is replaced by *fliC^{sticky}* flanked by *fliA* and *fliD* homology regions	this work

pTOF-pHluorin	cm^R, pTOF24 derivative, kan^R is replaced by $pHluorin$ under P_{tac} flanked by *att*Tn7 site homology regions	this work
pTOF-pHluorin+*V.h.* prom	cm^R, pTOF24 derivative, kan^R is replaced by $pHluorin$ under cytochrome C oxidase promoter from *Vibrio harveyi* flanked by *att*Tn7 site homology regions	this work
pWR20	kan^R, *EGPF* gene under cytochrome C oxidase promoter from *V. harveyi*	(Pilizota et al., 2012)
pWR-cpYFP	kan^R, pWR20 derivative, *cpYFP* gene under cytochrome C oxidase promoter from *V. harveyi*	this work
pWR-pHRed	kan^R, pWR20 derivative, *pHRed* gene under cytochrome C oxidase promoter from *V. harveyi*	this work
pWR-PkatG	kan^R, pWR20 derivative, *EGFP* gene under P_{katG} promoter	this work
pWR-PsoxS	kan^R, pWR20 derivative, *EGFP* gene under P_{soxS} promoter	this work
pRSET-B	amp^R, bacteriophage T7 promoter for high-level expression	(Schoepfer, 1993)
pRSET-pHluorin-his	amp^R, pRSET-B derivative, His-tagged *pHluorin* under T7 promoter	this work
pRSET-pHRed	amp^R, pRSET-B derivative, *pHRed* under T7 promoter	this work
pBAD18-Cm	cm^R, pkk223-3 derivative, arabinose PBAD promoter	(Guzman et al., 1995)
pBAD18-pHRed	cm^R, pBAD18-Cm derivative, *pHRed* under arabinose PBAD promoter	this work

TABLE 2.2: List of strains used in this work.

Strain name	Description	Source
MG1655	*E.coli* K-12, F- *λ*- *ilvG*- *rfb*-50 *rph*-1	(Guyer et al., 1981)
BW25113	*E.coli* K-12, Δ*(araD-araB)567* Δ*lacZ4787*(::rrnB-3) F- *λ*- *rph*-1 Δ*hsdR514 (rhaD-rhaB)568*	(Datsenko et al., 2000)
BL21	*E.coli* K-12, F- *dcm ompT hsdS*(rB- mB-) *gal*	(Studier et al., 1986)
EK01	MG1655 *fliC* replaced with $fliC^{sticky}$	this work
EK02	BW25113 *fliC* replaced with $fliC^{sticky}$	this work
EK03	EK01 with pkk223-3-pHluorin plasmid	this work
EK04	EK02 with pkk223-3-pHluorin plasmid	this work
EK05	EK01 with *pHluorin* under P_{tac} promoter on *att*Tn7 site	this work
EK06	MG1655 with *pHluorin* under cytochrome C oxidase promoter from *V. harveyi* on *att*Tn7 site	this work
EK07	EK01 with *pHluorin* under cytochrome C oxidase promoter from *V. harveyi* on *att*Tn7 site	this work
EK08	EK01 with pWR-cpYFP	this work

2.1.2 Replacement of the *fliC* gene with *fliC*^{sticky} in MG1655 and BW25113

For bead assay motor speed measurements *fliC* gene encoding flagellar filament was replaced by its "sticky" derivative (Kuwajima, 1988) in *E.coli* K-12 MG1655 and BW25113 strains. Resulting strains were named EK01 and EK02 respectively. The replacement was performed by plasmid mediated gene replacement technique (PMGR) (Merlin et al., 2002; Link et al., 1997). The method is based on RecA-mediated recombination occurring between homologous regions on the chromosome and plasmid-mediator.

A pTOF24 plasmid was chosen as a backbone for the plasmid-mediator constructs for having following important features: (1) a temperature sensitive replication initiator protein with permissive temperature being 30°C and non-permissive being 42°C (*repA*^{ts}), (2) a chloramphenicol resistance as a positive selection marker (*CmR*) and (3) a negative selection marker *sacB* encoding levansucrase, which makes *E.coli* cells sensitive to sucrose (Fig. 2.1A). A pTOF24 backbone was digested with *PstI* and *SalI* restriction enzymes to cut *KanR* gene out and pTOF-*fliC*^{sticky} derivative was constructed using Gibson assembly reaction (Gibson et al., 2009). The plasmid map is shown in Fig. 2.1B. *fliC*^{sticky} gene is flanked by ∼400 bp fragments homologous to the chromosome regions surrounding *fliC* gene (called *fliA* and *fliD* shoulders). For fragments amplification primers listed in Table A.1 were used . NEB DH5α competent cells (NEB, USA) were transformed with the assembly mix according to NEB protocol. Colonies were tested for kanamycin sensitivity and for the presence of the desired mutation in *fliC* gene by PCR (primers are listed in Table A.1). MG1655 and BW25113 strains were then transformed with the resulting plasmid purified with the Qiagen (Germany) Plasmid Purification Kit.

For getting chromosomal alteration in MG1655 and BW25113 the PMGR protocol described in (Merlin et al., 2002) was followed . Schematic of the protocol is shown in Fig. 2.2: transformation was followed by incubation at 30°C to ensure autonomous plasmid replication. Successful transformants were selected using chloramphenicol resistance marker. Several colonies were streaked on a fresh chloramphenicol plate and left at 42°C overnight to select for strains with a plasmid integrated into the chromosome by one of the homologous arms. This step was repeated once more to ensure the purity of

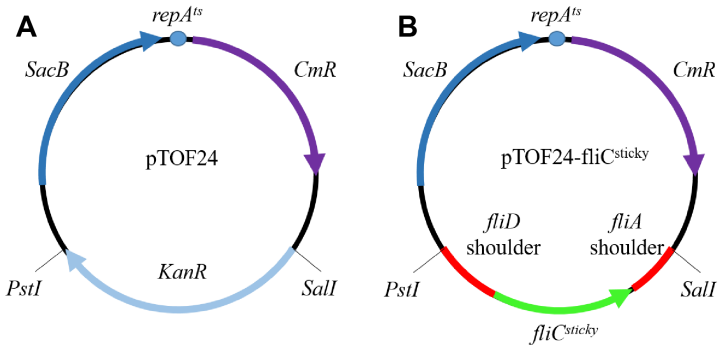

FIGURE 2.1: Plasmid maps. (**A**) pTOF24 plasmid is used as a backbone vector for the PMGR plasmids-mediators constructs. Temperature sensitive replication system is labelled $repA^{ts}$, *KanR* and *CmR* represent kanamycin and chloramphenicol resistances respectively; *SacB* encodes levansucrase, which converts sucrose into a product toxic for *E.coli* making it negative selection marker. (**B**) pTOF-$fliC^{sticky}$ is a pTOF24 derivative with *KanR* replaced with $fliC^{sticky}$ flanked by two regions (sim400 bp each) of homology to the part of the chromosome surrounding *fliC* gene (called here *fliA* and *fliD* shoulders).

integrants. Plasmid removal from the chromosome was done by growing individual colonies non-selectively with shaking at 30°C overnight in a liquid culture. The mixture containing both cells that lost or retained a plasmid, was diluted to 10^{-5} and 100 μl of a dilution were plated onto LB plate with 5% sucrose. The step worked as a negative selection, cells containing a full copy of a plasmid in their chromosome were sensitive to sucrose. Plate was incubated at 30°C overnight. As sucrose sensitivity is not as great as to antibiotics, cells were also tested for chloramphenicol sensitivity. The presence of the desired mutation in strains growing in the presence of sucrose but sensitive to chloramphenicol, was confirmed with PCR and, later, by sequencing (sequence is given in the Appendix A.3). The resulting strains were named EK01 (MG1655 derivative) and EK02 (BW25113 derivative).

2.1.3 *pHluorin* under different promoters

For simultaneous measurements of cytoplasmic pH and motor speed EK01 and EK02 strains were transformed with pkk223-3-pHluorin(M153R) plasmid from (Morimoto et al., 2011) containing pHluorin(M153R) under IPTG inducible P_{tac} promoter and ampicillin resistance marker (Fig. 2.3A). M153R mutation in original pHluorin (Miesenböck et al., 1998) improves stability of its fusion

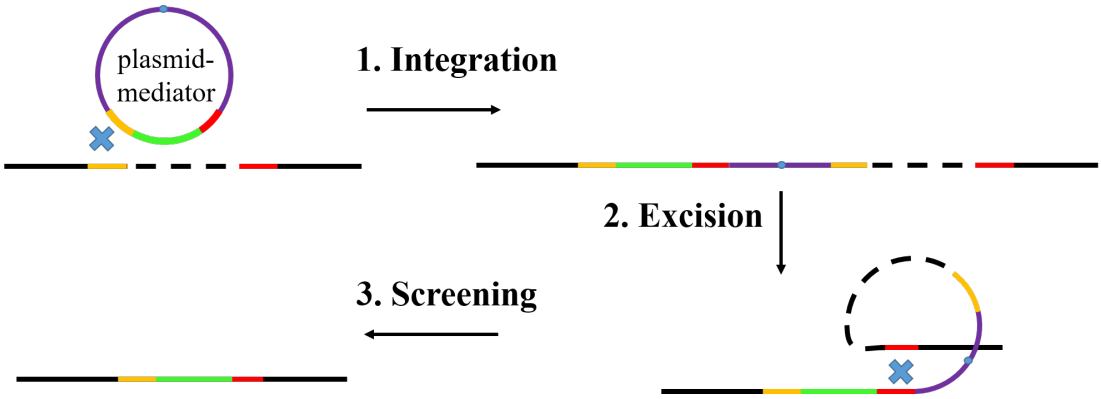

FIGURE 2.2: Key stages of the PMGR protocol. **1. Integration:** pTOF24-based plasmid-mediator is integrated into the chromosome by RecA-mediated homology recombination. Regions of homology are labelled with the same colour, blue cross represents recombination event. At this stage integrants are selected at 42°C on Cm plates. **2. Excision:** vector is excised from the chromosome when cells are grown in non-selective media at 30°C and negatively selected for sucrose sensitivity. **3. Screening:** colonies are checked for Cm sensitivity and mutation is confirmed by colony PCR. Successful clones will have the gene of interest (green) inserted between chromosomal regions pre-defined by the plasmid-mediator design (orange and red).

proteins without changing other properties of the pH sensor (Morimoto et al., 2011). For the simplicity of reading from here further I will refer to it as pHluorin, always meaning pHluorin(M153R) version. EK01 and EK02 strains with pkk223-3-pHluorin plasmids were called EK03 and EK04 respectively.

As the project suggested treatment bacteria with the variety of external stresses it had been decided to place *pHluorin* gene onto the chromosome. That way the resulting strain would contain no antibiotic resistance marker and, thus, set no limits for the stresses that could potentially be applied. Having the strain with a single copy of *pHluorin* gene and no antibiotic marker would also mean the minimal possible alteration of a wild type parent strain allowing simultaneous pH and PMF measurements. For the gene insertion *att*Tn7 site was selected. *Att*Tn7 is a unique attachment site of Tn7 transposon (Bolton et al., 1984) located downstream of highly conserved glutamine synthetase (*glmS*) gene. This site was chosen for being "neutral": e. g. causing no disruption of gene expression or any known negative effects on a host cell (Peters et al., 2001). The same PMGR approach was used to place *pHluorin* gene onto the chosen chromosomal site. The map of plasmid-mediator is shown in Fig. 2.3B. *pHluorin*-containing fragment with the P_{tac} promoter was amplified from the

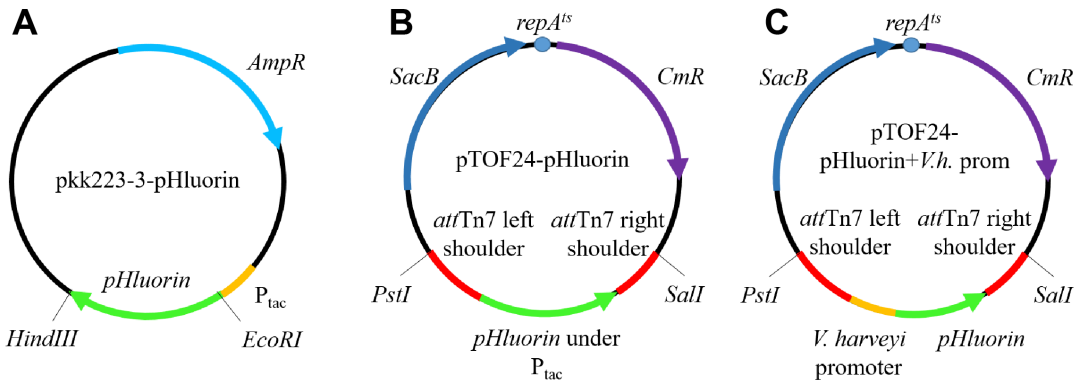

FIGURE 2.3: *pHluorin*-containing plasmids maps. (**A**) pkk223-3-pHluorin contains *pHluorin* under IPTG inducible P_{tac} promoter and ampicillin resistance gene *AmpR*. (**B**) pTOF-pHluorin is a pTOF24 derivative with *KanR* replaced with *pHluorin* under P_{tac} promoter flanked by *att*Tn7 site homology regions. (**C**) pTOF-pHluorin+*V.h.* prom is a pTOF24 derivative with *KanR* replaced with *pHluorin* under the cytochrome C oxidase promoter from *V. harveyi*, flanked by the same *att*Tn7 site homology regions as pTOF-pHluorin.

pkk223-3-pHluorin plasmid using primers listed in Table A.1. *Att*Tn7 homology regions were amplified using MG1655 chromosome as a template. EK01 and MG1655 strains were transformed with the resulting plasmid-mediators and PMGR protocol was performed to get EK05 and EK06 strains respectively. The colonies were then checked for the insert presence with PCR and further tested for fluorescence.

To achieve higher pHluorin expression levels P_{tac} promoter was later replaced with the strong constitutive promoter of *V. harveyi* cytochrome C oxidase from pWR20 plasmid (Pilizota et al., 2012). The plasmid-mediator pTOF-pHluorin+*V.h.* prom (Fig. 2.3C) was constructed as described above using Gibson assembly of four fragments amplified with primers from Table A.1. EK01 strain was transformed with pTOF-pHluorin+*V.h.* prom followed by the PMGR protocol. Colonies that showed the presence of the correct insert after the colony PCR were taken for the fluorescence test. The resulting strain was named EK07. EK07 strain expresses pHluorin from the chromosome and has *fliC* gene replaced with $fliC^{sticky}$.

2.1.4 cpYFP plasmid construction

Plasmid pShuttle-CMV_mt-cpYFP carrying *cpYFP* was received from Prof. Dr. Markus Schwarzländer. pShuttle-CMV is a system for mammalian expression containing pUC origin and kanamycin resistance gene for propagation and selection in *E.coli* (He et al., 1998). The plasmid could be replicated and stored in *E.coli*, however *cpYFP* gene could not be expressed and required additional cloning into a vector suitable for bacterial expression. *cpYFP* was transferred to pWR20 plasmid (Pilizota et al., 2012) to replace *EGFP* by amplification of both a backbone and an insert with primers listed in Table A.1 followed by the digestion with *NdeI* and *AvrII* restriction enzymes and ligation with T4 DNA ligase. NEB DH5α competent cells were transformed with the ligation mix according to the NEB protocol and incubated overnight on the kanamycin-containing plate. The clones were checked for the insert presence by PCR with the primers used for initial *cpYFP* amplification. Resulting plasmid map is shown in Fig. 2.4.

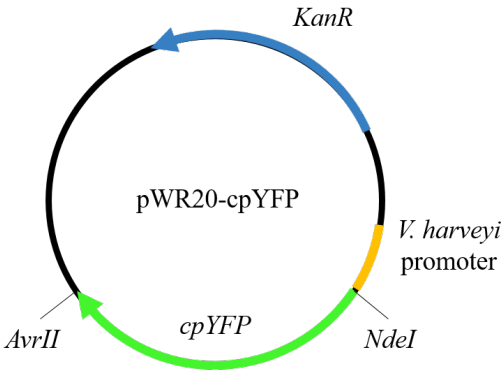

FIGURE 2.4: pWR20-cpYFP. *cpYFP* is inserted between *NdeI* and *AvrII* restriction sites under control of the cytochrome C oxidase promoter from *V. harveyi*. Vector contains kanamycin resistance gene *KanR*.

The successful colonies were tested for fluorescence. The EK01 was transformed with the resulting plasmid to obtain EK08 strain.

2.1.5 pHRed under different promoters

pRSETB-pHRed (referred to as pRSET-pHRed, Fig. 2.5) plasmid was acquired from Addgene.

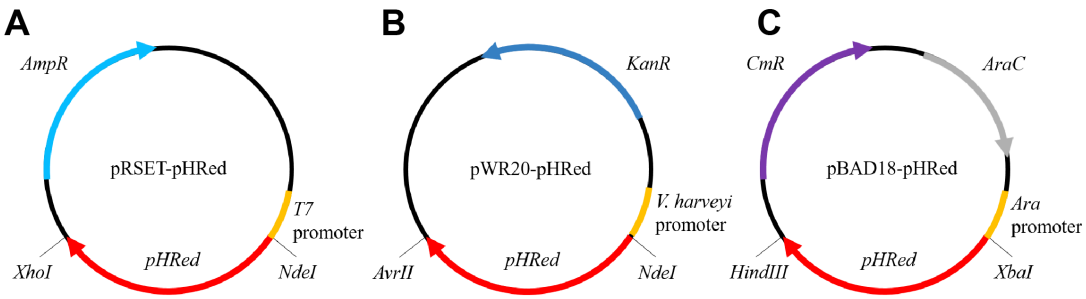

FIGURE 2.5: *pHRed*-containing plasmids maps. (**A**) pRSET-pHRed contains *pHRed* under T7 promoter and ampicillin resistance gene *AmpR*. (**B**) pWR20-pHRed is a pWR20 derivative with *EGFP* replaced with *pHRed*. (**C**) pBAD-pHRed is a pBAD18-Cm derivative with *pHRed* inserted into multiple cloning site between *XbaI* and *HindIII* restriction sites.

For pWR20-pHRed construction, pWR20 backbone and *pHRed* insert were amplified with primers from Table A.1 containing *AvrII* and *NdeI* restriction sites. Amplification was followed by the digestion with corresponding restriction enzymes. For pBAD18-based construct *pHRed*-containing plasmid and pBAD18 backbone were digested with *XbaI* and *HindIII* restriction enzymes and purified by extracting the bands of the desired size from 1% (m/v) agarose gel. Purified plasmids were then ligated with T4 DNA ligase. NEB DH5α competent cells were transformed with the ligation mix according to NEB protocol and incubated overnight on the kanamycin (for pWR20) or chloramphenicol (for pBAD18) containing plate. Next day colonies were checked for the insert presence by PCR with the primers used for initial amplification. Plasmid maps are shown in Fig. 2.5B and C. pBAD-pHRed was then transferred into BW25113 strain lacking *araBAD* operon (Datsenko et al., 2000) enabling inducible expression from *Ara* promoter upon addition of L-arabinose.

2.1.6 His-tagged pHluorin for purification

pRSET backbone and *pHluorin* insert were amplified with primers listed in Table A.1 containing *AvrII* and *XmaI* restriction sites. Forward insert primer contained the sequence encoding 6 *His* residues. The amplified fragments were then digested with the corresponding restriction enzymes and ligated with T4 DNA ligase followed by NEB DH5α competent cells transformation with the ligation mix. Next day colonies were checked for the insert presence with the

colony PCR. The resulting plasmid (Fig. 2.6) was then transferred into BL21 strain (Studier et al., 1986) for the overexpression of His-tagged pHluorin.

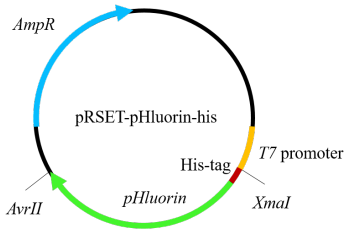

FIGURE 2.6: pRSET-pHluorin-his plasmid containing ampicillin resistance gene *AmpR* and his-tagged *pHluorin* under T7 promoter. Sequence encoding six histidine (*His*) residues is located upstream of the *pHluorin* encoding region to create a His-tag on the N-terminus of pHluorin protein.

2.1.7 Strains for oxidative damage characterisation

Plasmids for the oxidative damage (Fig. 2.7) were constructed as follows: pWR20 backbone and the insert (P_{katG} or P_{soxS}) were amplified with primers listed in Table A.1. The fragments were then assembled together in the Gibson assembly reaction. NEB DH5α competent cells were transformed with the assembly mix and plated onto the kanamycin-containing LB plates. Next day the colonies were tested by PCR with forward primer being the same as for the initial insert amplification and reverse primer (EGFP contr rev) designed for the control of the *EGFP* presence (Table A.1). The strains containing pWR20-PkatG and pWR20-PsoxS were subsequently tested for the specific H_2O_2 induction.

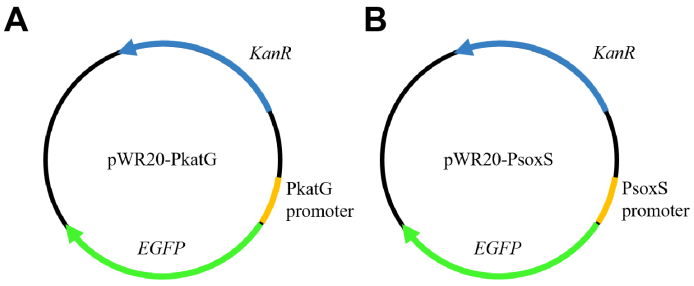

FIGURE 2.7: Strains for oxidative damage detection. pWR20 plasmid containing kanamycin resistance gene *KanR* was modified to have *EGFP* encoding gene under inducible P_{katG} (**A**) or P_{soxS} (**B**) promoter.

2.2 Protein purification

The purification was performed in The Edinburgh Protein Purification Facility (EPPF) with the help and supervision of Dr Matthew Nowicki.

2.2.1 Protein purification buffers

Buffers used for the purification protocol:

- Gel Filtration buffer: 20 mM HEPES, 150 mM NaCl, pH 7.5 adjusted with 0.1 M NaOH
- Lysis/Wash buffer: 50 mM HEPES, 250 mM NaCl, 5 mM imidazole, pH 7.5 pH 7.5 adjusted with 0.1 M NaOH
- Elution buffer: 50 mM HEPES, 250 mM NaCl, 500 mM imidazole, pH 7.5 pH 7.5 adjusted with 0.1 M NaOH

Buffers were filtered and degassed with 0.22 μm filter before use.

2.2.2 Cell culture preparation

Stabbed overnight culture of BL21+pRSET-pHluorin-his was prepared from the frozen stock in 5 ml of LB+ampicillin (100 μg/ml) in 50 ml falcon tube. The culture was incubated at 37°C while being shaken at 220 rpm. The next day, culture (5 ml) was transferred into 500 ml of fresh LB in a 2 L conical flask. At OD 0.6 1 ml of 0.5 M IPTG was added to the medium to final concentration 1 mM. The culture was then grown overnight at 37°C while being shaken at 220 rpm. Next morning, cell culture was spun down in a centrifuge pre-chilled to 4°C with JLA8.1000 rotor at 5000 g for 45 minutes. After the centrifugation supernatant was discarded and pellet was snap frozen in liquid nitrogen in 50 ml Falcon tubes for further use.

2.2.3 Purification procedure

The cell pellet prepared as described above was thawed on ice, 30 ml of Lysis/Wash buffer was added together with 1 tablet of Pierce Protease Inhibitor Tablets (Thermo Fisher Scientific Inc., USA). Solution was mixed on vortex to

homogeneous state. Cells were then lysed with a Cell Disruptor (Constant Systems, UK) at 25 kPSI. Soluble proteins fraction was separated by centrifugation of the cell lysate in JA-25.50 rotor at 25000 g for 45 min and filtered with 0.22 μm filter. ÄKTA™ Laboratory-scale Chromatography System (GE Healthcare Life Sciences, UK) was used for affinity chromatography purification with affinity column (HiTrap IMAC FF 1 ml) charged with nickel (100 mM $NiSO_4$). Elution buffer was used for this step. The sample was then gel filtered in the Gel Filtration buffer with a size exclusion column HiLoad 16/60 Superdex 75 prep grade. Protein gels were run as follows: ready-made SDS page (Sigma-Aldrich, USA) was loaded with samples after their denaturation at 100°C for 2-3 minutes. Gels were placed into a gel chamber, filled with 1xTris/Glycine/SDS buffer (pH 8.3), and run for 30 minutes with 200 V applied. Resulting gels showing samples after the affinity chromatography (**A**) and after the gel filtration (**B**) are shown in Fig. 2.8. Expected protein weight was 27 kDa. The purification yielded in 20 mg of pHluorin protein in ~1 mg/ml concentration.

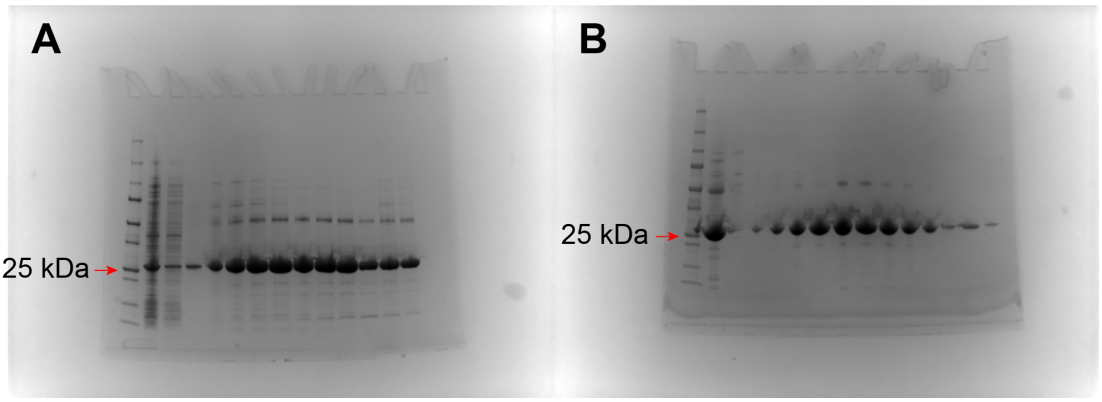

FIGURE 2.8: Protein gels after affinity chromatography (**A**) and gel filtration (**B**). (**A**) From left to right: molecular weight marker, sample before purification, flow-through, purified protein samples. (**B**) From left to right: molecular weight marker, sample after affinity chromatography only, gel filtered protein samples.

2.2.4 Cytoplasm purification

Non His-tagged cpYFP for *in vitro* tests (Fig. 3.13) was extracted together with the soluble part of the EK08 cytoplasm. The EK08 strain was grown in 250 ml of LB overnight, and subsequently pelleted at 9000 RPM for 30 min in Heraeus™ Megafuge™ (Thermo Fisher Scientific, UK) with HIGHConic III Fixed Angle

Rotor. The pellet was then resuspended in the 20 ml of the ice cold HEPES buffer with the half of Pierce Protease Inhibitor Tablet. Cells were disrupted with the sonicator (MSE (UK) Ltd Soniprep 150, 4 consequent 30 second pulses 10 μm amplitude with 30 seconds intervals). The disrupted cells were centrifuged again and the supernatant was filtered with 0.22 μm filter to obtain the soluble cytoplasmic fraction.

2.3 Customised microscope

Pilizota's lab custom-made microscope included bright field, position detection and optical trapping capabilities. To allow simultaneous measurements of the cytoplasmic pH and flagellar motor speed with the bead assay I complemented it with the epifluorescence capabilities. The layout of the microscope after the implemented modifications is shown in Fig. 2.9.

2.3.1 Bright field

The bright field illumination was aligned as described in (Rosko, 2017) and its optical path is shown as solid grey line in Fig. 2.9. Briefly: the light from the white LED (Luxeon Star, USA) with a current source (A011-D-V-700 FlexBlock-TM, Luxdrive, USA), controlled by custom written LabView program, passes through a f5=12.7 mm lens followed by neutral density (ND) filter with a 100-fold attenuation, which focuses the image of the LED onto the back focal plane of the condenser (Nikon, Japan; NA 1.4). After passing the condenser light is defocused to create a Köhler illumination of the sample plane.

2.3.2 Optical trap and position detection

The optical trap principle is based on the work of Ashkin *et al.* (Ashkin et al., 1986). The trap is formed by a 855 nm continuous wave diode laser beam (Blue Sky Research, USA) tightly focused in the sample plane. For position detection purposes the beam intensity is reduced by a factor of $1.55 \cdot 10^3$ with two ND filters (ND2 in Fig. 2.9). The beam is then expanded 4 times in cross section after passing through a telescope formed with f1=25 mm and f2=100 mm lenses and focused in the sample plane by Nikon CFI Plan Apochromat Lambda 100x objective with an NA of 1.45. After being scattered by

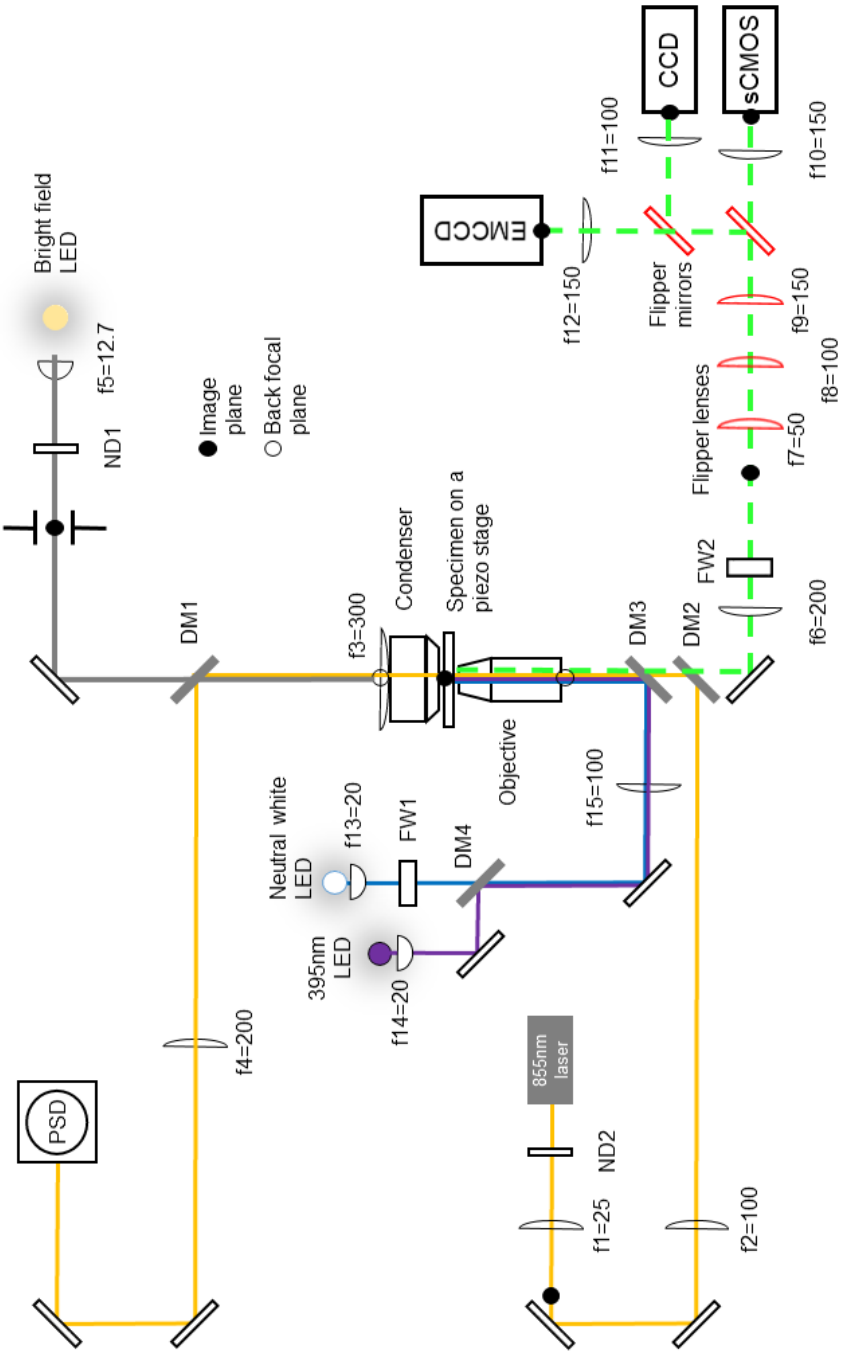

FIGURE 2.9: Full microscope layout. Polychroic mirrors are labelled "DM", lenses are labelled "f=xx", where xx is a lens focal distance in mm. "FW" stands for filter wheel, and neutral density filter is denoted with "ND". Coloured lines represent optical paths: bright field illumination (grey), epifluorescence illumination (purple and blue) optical trap laser (yellow), image (dashed green).

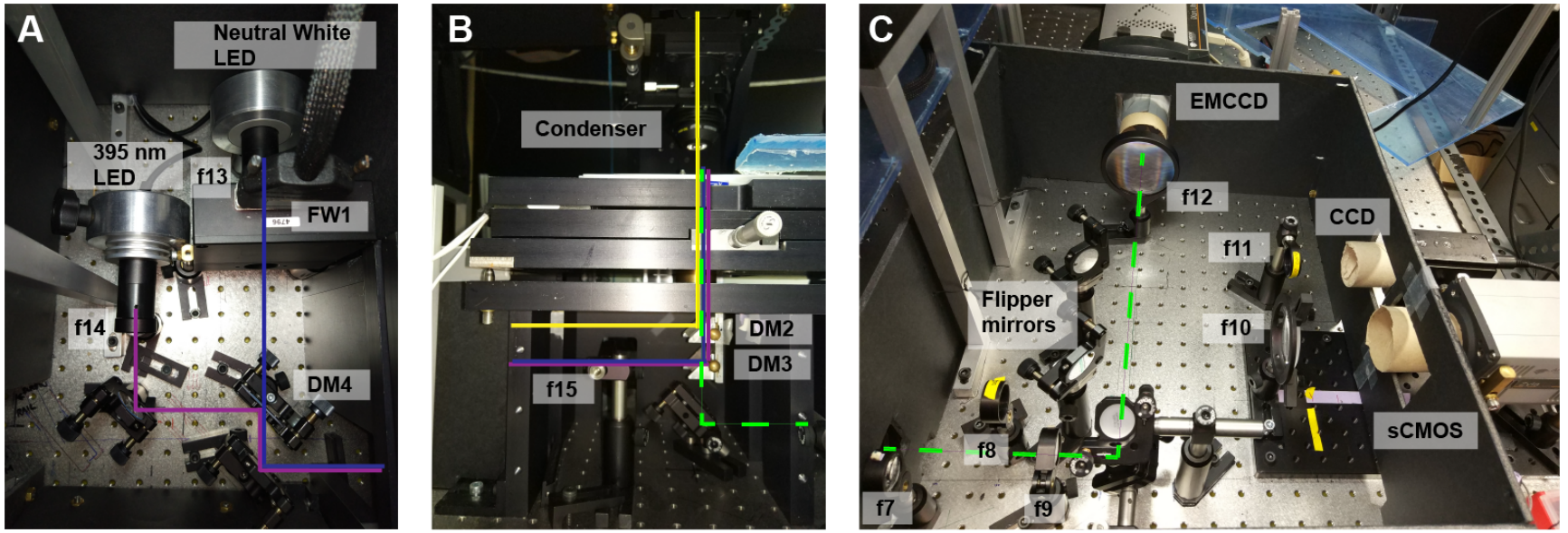

FIGURE 2.10: Images of the microscope parts added to initial design to allow epifluorescence imaging. (**A**) Neutral white and 395 nm LEDs for epifluorescence illumination. Light from Neutral white LED passes through filter wheel (FW1) containing optical filters to cut out desired part of the spectrum followed by the dichroic mirror (DM4) transparent for wavelength longer than 410 nm. 395 nm LED emitted light joins the Neutral white LED emitted light after being reflected by the DM4. Light is then redirected towards the objective. (**B**) Light from either of the two LEDs from **A** is focussed in the back focal plane of the objective by f15 lens. It passes through the objective after being reflected from the polychroic mirror DM2 (mirror is selected based on the application) and passing through DM1 shortpass filter used for the reflection of 855 nm laser beam. Green dashed line shows the optical path of the image coming from the sample plane to one of the three cameras. (**C**) CCD, Zyla sCMOS and EMCCD cameras with their infinity lenses f10, f11 and f12 respectively. The image from the objective passes through one of the flipper telescope lenses (f7, f8 or f9, for different magnifications) and gets focused on the camera chip after being reflected by the flipper mirror. Green dashed line represents the optical path for the configuration shown in the picture: image passes through the lowest magnification lens f9 and is focused onto EMCCD camera chip as both flipper mirrors are lifted.

the sample the laser beam passes through the condenser, gets reflected by the shortpass (800 nm) dichroic mirror DM1 and focused onto position sensitive detector (PSD Model 2931, New Focus, USA) by f4=200 mm. The interferometry pattern formed by scattered and unscattered parts of the beam is highly sensitive to the position of the sample. The change in the pattern intensity allows position sensitive detector to record a time course of the sample movement (Gittes et al., 1998; Farré et al., 2012). Sample position (x,y) is calculated from photocurrents $I_1 - I_4$ as $(I_1 + I_3 - (I_2 + I_4))/(I_1 + I_3 + I_2 + I_4) = 2x/L$ and $(I_1 + I_2 - (I_3 + I_4))/(I_1 + I_3 + I_2 + I_4) = 2y/L$, where L is the PSD detector side length (Fig. 2.13A).

2.3.3 Epifluorescence

The OptoLED (Cairn Research, UK) unit capable to independently drive two LEDs was chosen as an epifluorescence illumination source for having an optical feedback circuit for maintaining constant power, which allowed an excellent wavelength and intensity stability. In addition, it could be easily controlled with NI LabView, our chosen programming package. LED was chosen over the lamp-based sources for its low heat output and longer lifetime. The optical paths of light beams emitted by the two LED heads were joined together with the dichroic mirror (Fig. 2.10A) in order to get a spectrum wide enough for chosen fluorescent indicators, 375-750 nm (Fig. 2.11).

A holder for two polychroic mirrors was designed to allow simultaneous use of the optical trap and fluorescence (Fig. 2.10B). It provided an easy access to the mirrors and the possibility of changing them when needed in the limited space under the stage. The drawing of the two-level mirror mount is given in Appendix B.

For the fluorescence imaging single-photon sensitive iXon Ultra 897 EMCCD camera (Andor, UK) was infinity corrected with f12=150 mm lens and installed in addition to Zyla 5.5 sCMOS (Andor, UK) and AVCAM 405 CCD (Brian Reece Scientific Ltd., UK) cameras. Switching between three cameras is achieved by changing the position of the flipper mirrors (Fig. 2.10C). EMCCD camera was used for all the fluorescence imaging, while CCD camera served as an auxiliary tool for spinner finding in speed measurement experiments.

To control the microscope hardware I wrote several LabView scripts driving EMCCD camera, filter wheels and the LEDs.

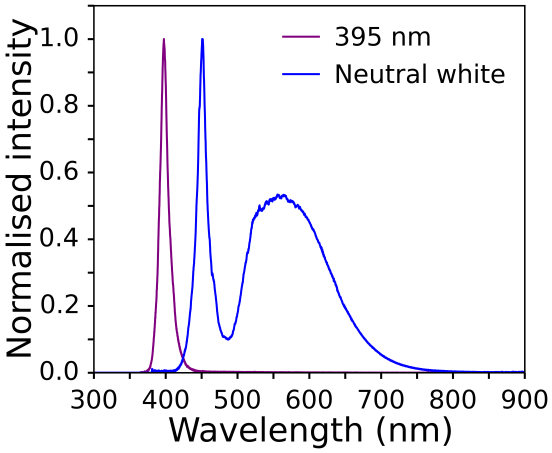

FIGURE 2.11: Combined spectra of the two LEDs. Normalised intensity is plotted against wavelength. Purple line is for 395 nm LED, blue line — for Neutral white.

2.4 Experimental procedure

2.4.1 Cell culturing and media

Media used for culturing and imaging:

- Lysogeny broth (LB): 10 g tryptone, 5 g yeast extract, 10 g NaCl per 1 l, pH 7.0 (not adjusted)
- Modified Minimal medium (MM9): aqueous solution of 50 mM Na_2HPO_4, 25 mM NaH_2PO_4, 8.5 mM NaCl and 18.7 mM NH_4Cl with added 0.1 mM $CaCl_2$, 1 mM KCl, 2 mM $MgSO_4$ and 0.3% glucose, adjusted to pH 7.5 with 0.1 M NaOH
- Phosphate buffered saline (PBS): aqueous solution of 154 mM NaCl, 5 mM Na_2HPO_4 and 1.5 mM KH_2PO_4, adjusted to pH 7.5 with 0.1 M NaOH
- Berg's motility buffer (BMB): aqueous solution of 6.2 mM K_2HPO_4, 3.8 mM KH_2PO_4, 67 mM NaCl, and 0.1 mM EDTA, supplemented with 20 mM glucose, pH 7.02
- Calibration buffer: 100 mM MES, 100 mM HEPES, 100 mM AMPSO, varied pH adjusted with 0.1 M NaOH or 0.1 M HCl

Cells for the simultaneous PMF and pH measurements were diluted from the overnight culture to 1:2000 ratio in fresh LB and grown at 37°C with continuous shaking (220 rpm) to OD=2.0 (Fig. 3.4). After growth cells were sheared and washed (see next Section) into MM9 or PBS.

2.4.2 Samples preparation

Cells were "sheared" as described previously (Bai et al., 2010; Rosko et al., 2017; Rosko, 2017) by passing the culture 80 times through the device consisting of two 1 ml plastic syringes with 26 gauge needles connected by narrow tubing. Cells were then washed 3 times by centrifugation at 8000 g for 2 min into MM9 or PBS. Two types of microscopy slides were used. For experiments requiring fast media exchange (butanol/indole treatment, pH calibration) I used tunnel-slide (Fig. 2.12A) produced as described in (Rosko et al., 2017; Rosko, 2017). Microscope slide with two parallel bands of double-sided sticky tape at $\sim$5 mm distance from each other was covered with cover glass creating a tunnel of $\sim$10-15 μl volume. For experiments requiring long imaging of a single slide and, thus, constant supply of nutrients and oxygen, flow-cells were manufactured by drilling two 1.8 mm holes on opposite ends of the microscope slide and attaching Tygon® Microbore tubing (Saint Gobain Performance Plastics, France). The flow-cell was then created by attaching the gene frame (Fisher Scientific Ltd, USA) to the slide and covering it with a cover glass (Fig. 2.12B). Slides were coated with 1% poly-L-lysine (PLL) by flushing PLL through the flow-cell/tunnel-slide for $\sim$10 s followed by washing it out with the excessive volume of growth medium. Sheared and washed cells were then loaded into the flow-cell/tunnel-slide and incubated for 10 min to allow attachment. Excessive cells were washed out with the growth medium. Subsequently, 0.5 μm in diameter (if not stated otherwise) polystyrene beads (Polysciences, Inc, USA) were added to the flow-cell/tunnel-slide and incubated for 10 min with consequent washing out of the non-attached beads.

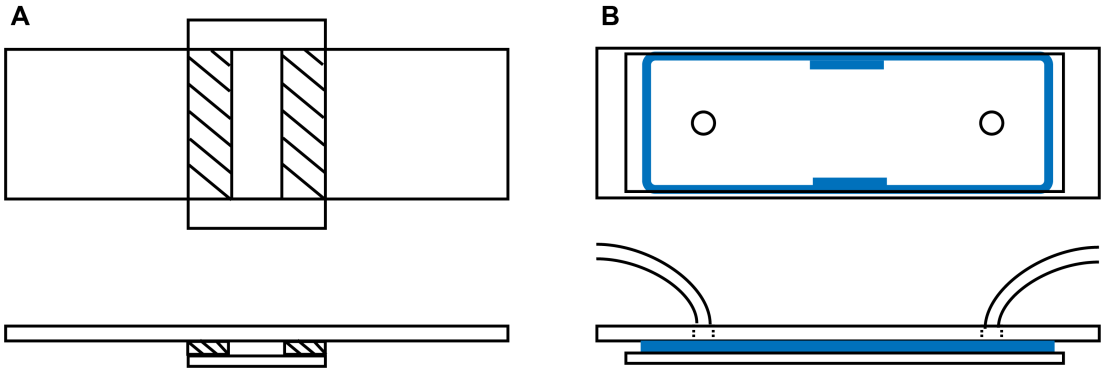

FIGURE 2.12: A cartoon of the tunnel-slide and the flow-cell. (**A**) Top view and side view of the tunnel-slide used for fast flush experiments (indole/butanol treatment, pH calibration): double sided sticky tape forms a channel and is sandwiched between the microscope slide and the cover glass. Overall volume of the tunnel-slide is ∼10-15 μl (26 mm x ∼5 mm x ∼0.1 mm). (**B**) Top view and side view of the flow-cell used for photodamage experiments: two 1.8 mm holes are drilled in the microscope slides and connected to the tubing. The experimental chamber is formed by the gene frame and 22x60 mm cover glass. Overall volume of the flow-cell is ∼175-200 μl

2.4.3 Data collection

Back-focal-plane interferometry

Back-focal-plane interferometry (Denk et al., 1990; Svoboda et al., 1993) is performed as previously described (Rosko et al., 2017; Rosko, 2017). The optical trap was used to detect the rotation of a polystyrene bead attached to a truncated flagellar filament (Fig. 2.13A). Time course of the bead rotation is recorded with the PSD at 10 kHz, and a 2.5 kHz cutoff anti-aliasing filter applied before processing. Bead position (x,y) is calculated from photocurrents $I_1 - I_4$ as described in Section 2.3.2.

Fluorescent imaging

Fluorescent images of pHluorin or cpYFP were taken with EMCCD camera. Narrow spectrum 395 nm LED was used for the excitation at 395 nm and Neutral white LED with ET470/40x filter (Chroma Technology, USA) for 475 nm excitation. Emission was collected at 520 nm using ET525/40x filter (Chroma Technology, USA). Imaging settings varied depending on the experiment.

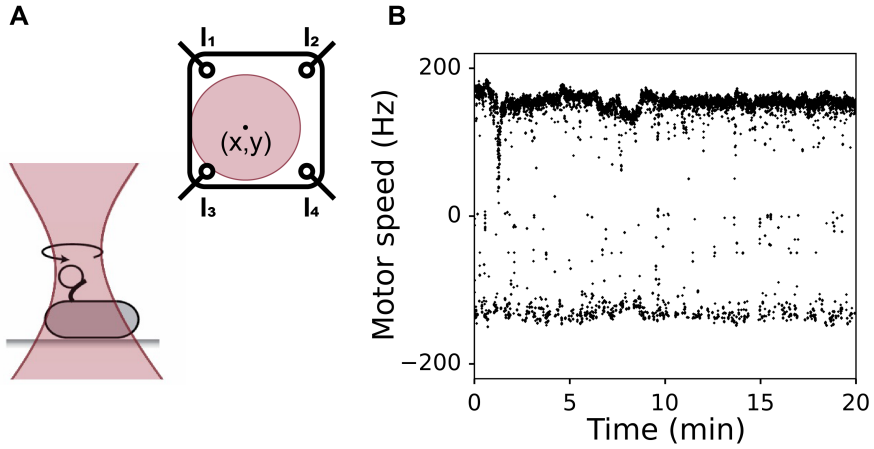

FIGURE 2.13: (**A**) Cell was attached to a cover glass with a truncated flagellar filament made "sticky" to polystyrene beads. The bead was brought into focus of a heavily attenuated optical trap and its position measured with position sensitive detector (PSD). PSD received photocurrents from the interferometry pattern formed on its surface by the rotating bead. Position of the centre of this interferometry pattern was calculated from the sum of photocurrents. (**B**) An example of raw motor speed trace recorded with BFP interferometry when no shock is applied. Here positive frequencies correspond to counter-clockwise (looking from the filament towards the motor) and negative to the clockwise rotation of the flagellar motor.

pH sensors calibration

The *in vivo* calibration of pH sensor was performed as described in (Wang et al., 2018). The mixture of 100 mM MES, HEPES and AMPSO buffers was adjusted to a set of pH values in range 5.5 - 9 and supplemented with one of the three pH collapsing agents: 40 mM potassium benzoate and 40 mM methylamine hydrochloride (Martinez et al., 2012a), 25 μM CCCP or 5 mM indole (Chimerel et al., 2012). Tunnel-slides were prepared as described above. Buffer of the known pH was flushed into a channel, incubated for 1, 5 or 15 minutes (as stated in the text), then 5 different fields of view containing in total over a 100 cells were imaged with 50 ms exposure time. The calibration curves were plotted as ratio of emission intensities for excitation at 395 nm and 475 nm against pH and fitted with the sigmoid function.

In vitro calibration was performed with the purified protein diluted into buffer of known pH in the 96-well plate (Thermo Scientific, Optical bottom). The pHluorin of cpYFP excitation spectra for 510 nm emission was measured in Spark 10M multimode plate reader (Tecan Trading AG, Switzerland). The

excitation was scanned from 380 nm to 480 nm with 5 nm step size. Additionally, the autofluorescence of the buffer with no added protein was measured and subtracted from the measured protein intensity.

For photodamage experiments the adjustment for photobleaching was done as follows: cells were prepared and attached to the flow-cell as described above, MM9 medium was supplemented with 5% ethanol to ensure cell's death, and was pumped with 10 μl/min flow rate. The imaging was performed as in the main experiments with varied exposure time and exposure rate. The photobleaching adjustments coefficients for each time point and for each photodamage condition used were then calculated from the resulting curves assuming that change in pHluorin intensities ratio was determined only by the protein photobleaching.

Indole and butanol treatments

Butanol (1-Butanol for molecular biology, $\geqslant$99%, Sigma-Aldrich, USA) and indole (Indole, analytical standard, Sigma-Aldrich, USA) treatment was performed as follows: after 2 min preshock recording of motor speed, 20 μl of MM9 supplemented with a given concentration of butanol or indole was flushed into the tunnel-slide. Flush was done by placing a droplet of liquid on one, and collecting it with a piece of tissue paper on the other side of the tunnel (Buda et al., 2016). Duration of the flush was no longer than 10 s. 10 μl droplets of shocking solution were then placed on both side of the tunnel to minimise evaporation. The shock motor speed was recorded for 10 min, followed by a flush back into MM9 medium only. Postshock speed was recorded for 5 min. The motor speed recording was uninterrupted for the duration of the experiment (total of 17 min). For pH control experiments fluorescent images were taken every 90 seconds.

Photodamage

Photodamage experiments were performed as follows: using the flow-cell MM9 or PBS was constantly supplied at 10 μl/min rate with a syringe pump (KR Analytical Ltd., UK). Cells were sequentially exposed to the light of λ=395 nm and 475 nm. The choice of these wavelengths was determined by the pHluorin fluorescence spectrum. Speed recording started simultaneously with the light

exposure. The exposure time and exposure rate were controlled with a custom written LabView program.

Camera exposure times were set in LabView same for both wavelength ($t_{exp,cam}$). The time light was on was supposed to be approximately the same as camera exposure time. Figure 2.14 shows the fragment of a custom written LabView program performing imaging with the EMCCD camera. LED was switched on just before the imaging and off straight after the acquisition was finished. The same procedure was then repeated with the other LED. However, I noticed that the software was adding a delay and light was on for longer time than expected. Surprisingly, the delay was different for the first (with 475 nm exposure) and second (395 nm) acquisitions. After replacing the acquisition commands with the standard LabView "Wait (ms)" VI, which allows a user to manually set a delay, the LED's time spent on returned to an expected value. Thus, I confirmed than the issue was in the Andor's camera drivers rather than in LEDs. The hypothesis is that the delay was caused by the "keep clean" cycle, which camera runs while idle to keep the chip free of charge. When "Start Acquisition.vi" is called camera must wait for the cycle to complete before proceeding to the acquisition. Thus, for two wavelength average time light was on was $t_{exp,light}$=225 ms+$t_{exp,cam}$ for 475 nm and $t_{exp,light}$=55 ms+$t_{exp,cam}$ for 395 nm. Actual light exposure times and rates were recorded with the same LabView program for calculation of the effective light power (P_{eff}) as the total energy delivered divided by the total length of the individual motor speed recording. Total energy delivered was estimated by measuring the illumination power in the sample plane multiplied by the total time of light exposure per 1 cm^2. The illumination area, estimated by photobleaching part of the slide and measuring the diameter of the bleached region ($\sim$220 μm).

$$P_{eff} = \frac{E_{total}}{t_{total}} = \frac{P_{LED} \cdot t_{exp,light} \cdot n_{flashes}}{S \cdot t_{total}} = \frac{P_{LED} \cdot t_{exp,light} \cdot f_{light}}{S}, \qquad (2.1)$$

where P_{LED} is the LED power, f_{light} is the frequency of the light flashes and S illumination area.

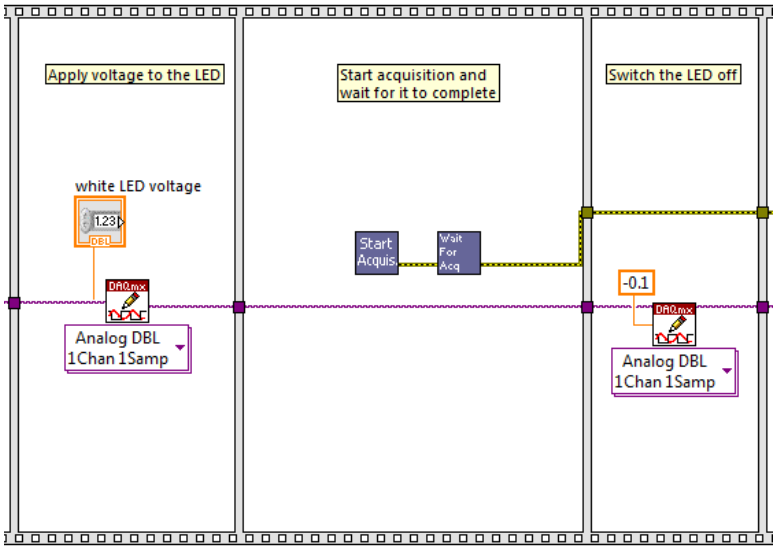

FIGURE 2.14: A fragment of a LabView program driving EMCCD camera.

2.5 Data analysis

2.5.1 Image analysis

Image analysis for calculation of cells internal pH was performed in Python as follows. The first image of the fluorescence time series was taken for the identification of cell's location assuming that field of view was not moving. The image (512x512 pixels) was divided into four squares and the background intensity was calculated for each as an average of intensity of 3x3 pixels box surrounding the pixel of minimal intensity, the single value of the background intensity was then obtained by averaging. Flat (well attached) cells were manually selected for the analysis. The coordinates of the selection were propagated through the image stack. Manually selected boxes containing one cell per box were cropped out from the image. To create a cell's mask the Otsu threshold (Otsu, 1979) followed by binary erosion and binary dilation was applied to each box. The cropped image was multiplied by the mask and the mean value of non-zero pixels was calculated. To get cell intensity I subtracted the background from the obtained value. The intensities for blue (475 nm) and UV (395 nm) channels were thus found and the ratio obtained for each image couple in a time series.

For calibration experiments intensity ratio $R_{395/475}$ was plotted against pH and fitted with a sigmoid function: $R_{395/475} = \frac{a_1 e^{k(pH-pH_0)}+a_2}{e^{k(pH-pH_0)}+1}$, where a_1, a_2, k, pH_0

are fitting parameters. The same function with the fitting parameters found was then used to convert ratios to pH values in the experiments.

2.5.2 Motor speed traces analysis

A flat top discrete Fourier transform (16384 window size with dt=0.01 s) was applied to x and y coordinates of bead position recorded by PSD to obtain a motor speed time series. The resulting speed traces are further referred to as raw traces (example in Fig. 2.13B). For further analysis speed traces were processed as follows: (a) absolute values were taken, (b) values below 10 Hz were removed and 50 Hz AC frequency values disregarded, (c) remaining data points were median filtered with 201 points moving window. To calculate mean speeds I applied a 10 s moving window on the speed traces processed as above.

Photodamage traces were normalised before fitting. The trace fragment consisting of the first 30 s of the recording was split into 60 windows containing 50 points each. The mean of maximum values found within each window was calculated and considered initial speed value, by which the rest of the trace was normalised. Each normalised trace was fitted with a single parameter exponential: $y = e^{-\alpha x}$. All fittings were performed in Python (SciPy module, curve fit optimization) with maximum number of calls to the optimization function taken as 20000.

Chapter 3

Cytoplasmic pH measurements with genetically encoded fluorescent probes

3.1 Introduction to pH sensors in bacteria

In chemistry, potential of hydrogen, or pH, is a measure of acidity or basicity of an aqueous solution and is defined as the negative of the base 10 logarithm of the activity of the hydrogen ion, $pH = -log_{10}(a_{H^+})$. Activity here is the *effective concentration* of a species in a mixture (Lewis, 1907). For simplicity we will further use terms "activity" and "concentration" interchangeably assuming that the solutions are close to ideal.

Cytoplasmic pH is a crucial parameter of bacteria physiology. It plays an important role in cellular energetics as one of the two components of the proton motive force (see Chapter 1), while also influences protein stability and enzymatic activity in the cell (Bearne, 2014). Neutrophilic bacteria, like *E. coli*, can survive in a range of pH starting as low as pH 2 in human stomach and up to pH 9, while maintaining internal pH in a relatively narrow range of 7-8 (Gorden et al., 1993; Lin et al., 1995; Slonczewski et al., 2009; Zilberstein et al., 1984; Slonczewski et al., 1981; Lund et al., 2014). The change in cytoplasmic pH can be caused by the external stress, such as acid or osmotic shocks (Slonczewski et al., 1981; Martinez et al., 2012a; Chakraborty et al., 2017). For some species acidification of the cytoplasm has been shown to be related to a

pathogenicity (Miller et al., 1989; Choi et al., 2016), which makes bacterial pH homoeostasis an interesting and relevant topic to study.

The history of the intracellular pH measurements began over a century ago. First attempts were made by Michaelis and Davidoff in 1912 and Michaelis and Kramsztyk in 1914 with a mammalian cells lysate tested with platinum/hydrogen electrode (Caldwell, 1956). Later, non-invasive methods were developed including radiolabeled membrane-permeant probes (Zilberstein et al., 1984; Kurkdjian et al., 1989), phosphorus-31 nuclear magnetic resonance (^{31}P NMR, (Moon et al., 1973; Ackerman et al., 1996)), microelectrodes (Thomas, 1974; Schwiening, 2007) and fluorescent probes (Kurkdjian et al., 1989; Slonczewski et al., 2009; Miesenböck et al., 1998; Schwiening, 2007; Han et al., 2010). The occurrence of the fluorescent probes and the development of the microscopy allowed pH measurements to reach single-cell resolution. Fluorescent probes could be divided into two categories: externally added dyes and genetically encoded proteins. The variety of dyes includes fluorescein-based dyes (BCECF, BCPCF, fluorescein), benzoxanthene dyes (SNAFLs, SNAFRs, SNARFs), cyanine-based indicators and more (Han et al., 2010). The main challenge in using exogenous probes is to deliver the dye into the cell cytoplasm in a concentration non-toxic to the cell so that it remains intact (Slonczewski et al., 2009). The delivery is not an issue for the genetically encoded probes, fluorescent pH sensitive proteins, such as pHluorins (Miesenböck et al., 1998) or other GFP derivatives (Kneen et al., 1998; Robey et al., 1998), cpYFP and its derivatives (Schwarzländer et al., 2014; Matlashov et al., 2015) or mFruit series (Shaner et al., 2004; Li et al., 2012).

Among the pH sensitive fluorescent proteins there is a class of ratiometric indicators that deserve special attention. These proteins can usually be excited at two different wavelengths and the emission intensity depends on the pH. The advantage of using emission ratios rather than absolute intensities is, first of all, the fact that the readings are not influenced by the number of proteins in the cell. The photobleaching is also not an issue when absolute intensities are not used as the illumination power can be adjusted such that two wavelengths bleach with the same rate, keeping the ratio constant.

In this chapter I test different genetically encoded ratiometric pH sensors, carefully examine *in vivo* calibration protocols and report how cytoplasmic pH of *E. coli* depends on the media and the stage of growth.

3.2 Extending the range of pH measurements

3.2.1 pHluorin

The most commonly used ratiometric fluorescent pH indicator for bacterial measurements is a GFP derivative pHluorin (Miesenböck et al., 1998). It has been used at least in *Escherichia coli*, *Bacillus subtilis* (Martinez et al., 2012a) and *Salmonella enterica* (Morimoto et al., 2011). The working principle of pHluorin is based on the existence of two stable confirmations of the GFP. The chromophore in its protonated state can be excited at 395 nm, and in deprotonated at 475 nm (Cubitt et al., 1995). Emission spectra does not significantly change and peaks at ~509 nm. When GFP is in its native form the spectrum is independent of the pH in range 5.5-10 (Miesenböck et al., 1998), implying that chromophore is shielded from the environment. pHluorin contains mutations that loosen the protonation reaction constrains by making chromophore more exposed to the environment. The probabilities of chromophore being in protonated or deprotonated state in pHluorin depend on pH, thus, making its spectrum pH sensitive (Fig. 3.1A).

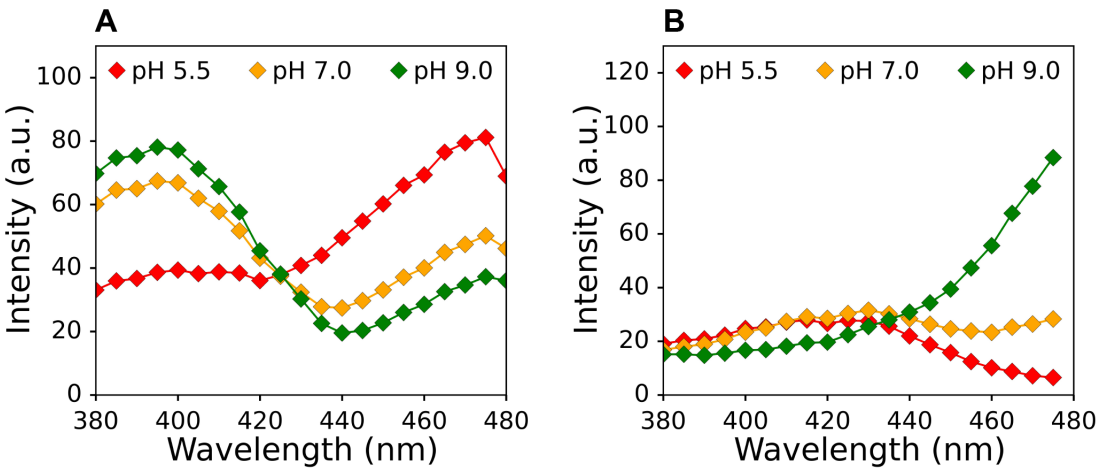

FIGURE 3.1: Excitation spectra of purified pHluorin (**A**) and cpYFP (**B**) at pH values 5.5 (red), 7.0 (yellow) and 9.0 (green). Emission is collected at 510 nm.

The plasmid containing *pHluorin* with M153R mutation (Morimoto et al., 2011) was kindly provided by Tohru Minamino. Based on this plasmid I constructed several strains with both plasmid and chromosomal expression of the

pHluorin (see Section 2.1.3). EK05 and EK06 strains contained a copy of *pHluorin* gene on the *Att*Tn7 site of the chromosome under control of the inducible P_{tac} promoter.

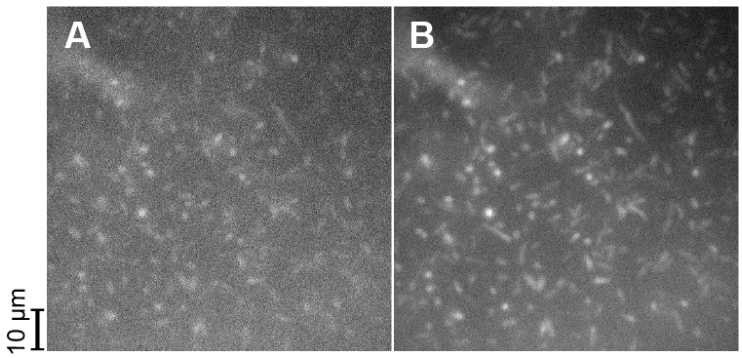

FIGURE 3.2: EK05 strain fluorescence test with 475 nm excitation and 510 nm emission. Overnight culture of EK05 cells with 1 mM IPTG added was washed 3 times in 10 mM sodium phosphate buffer and attached to the tunnel slide with poly-L-lysine. Cells were imaged with Andor EM-CCD camera with 0.5 sec exposure time and gain 300 (**A**) or 2 sec exposure time and 150 gain (**B**). Scale bar is 10 μm.

Tac promoter is a hybrid of *trp* and *lac* promoters (Boer et al., 1983). It is repressed by *lac* operon repressor *lacI* and derepressed by isopropyl β - D - 1 - thiogalactopyranoside (IPTG). For a finely tunable induction of *tac* promoter, the construct should be put into a $lacI^q$ mutant strain, which overexpresses *lacI* that consequently represses P_{tac} (Arfman et al., 1992). In the wild type strains (such as MG1655) background induction of P_{tac} is high and only increases about 2-fold upon IPTG addition. Fig. 3.2 shows the fluorescence images of EK05 strain expressing pHluorin controlled by P_{tac} promoter from the chromosomal copy of the gene. The fluorescence of the strains was too weak to be used for analysis even at exposure times as high as 2 seconds. It was suggested that P_{tac} promoter was not strong enough. As an alternative, EK07 strain with strong constitutive pHluorin expression was constructed (see Section 2.1). The fluorescence of the EK07 strain is shown in Fig. 3.3.

The growth curves of the EK01 (non-fluorescent), EK03 (expressing fluorescent protein from the plasmid) and EK07 (expressing fluorescent protein from the chromosome) strains in comparison with the wild type MG1655 were taken (Fig. 3.4). While the EK03 strain containing a plasmid exhibits a slight slowdown of the growth compared to the parent strain, both EK01 or EK07 demonstrate the same growth rate as the wild type. Thus, constructed EK07

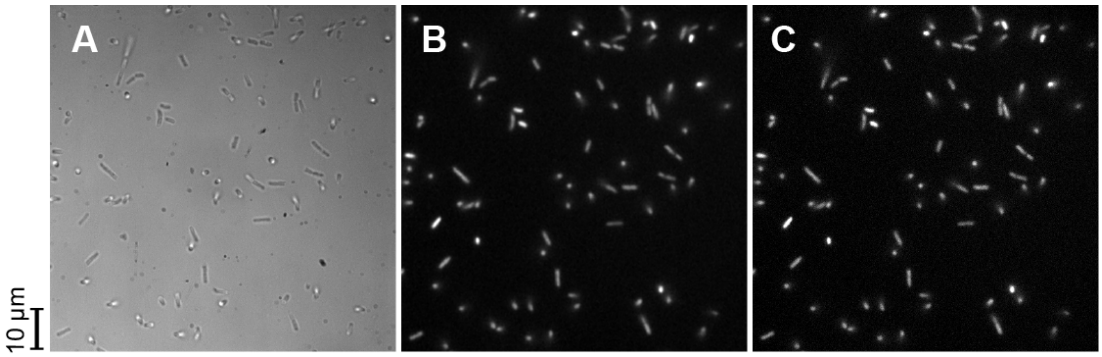

FIGURE 3.3: EK07 strain fluorescence test: (**A**) bright field image; (**B**) 475 nm excitation and 510 nm emission, 50 ms exposure time and 100 gain; (**C**) 395 nm excitation and 510 nm emission, 50 ms exposure time and 100 gain. Scale bar is 10 μm.

strain does not contain any antibiotic resistances, does not require induction for pHluorin expression and has the same growth rate as the parent MG1655 strain. It is MG1655 derivative that underwent only minimal necessary changes to allow simultaneous use of a bead assay and fluorescence imaging for the pH measurements. The strain was used for most of the experiments described further.

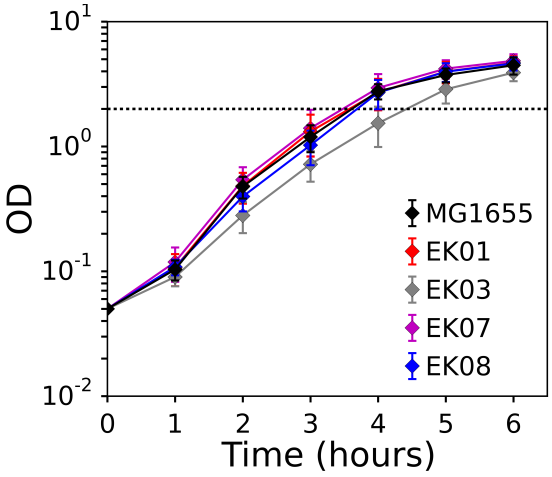

FIGURE 3.4: MG1655, EK01, EK03, EK07 and EK08 growth curves in LB diluted from the overnight culture to the initial OD 0.05. Cells were grown in 25 ml volume of medium in the 250 ml flasks at 37°C while shaken at 220 rpm. Dotted line indicates OD=2, at which EK07 cells were taken for the PMF measurements described in Chapter 4. Error bars show standard deviation for at least tree independent measurements.

When the strains had been constructed I calibrated the pH sensor and found that pHluorin reached the highest sensitivity in the range of pH 6.0-8.0 (Fig. 3.5).

To explore the possibilities of widening the range of pH measurements both to lower and to higher values I tested two more ratiometric pH sensors reported previously: cpYFP and pHRed.

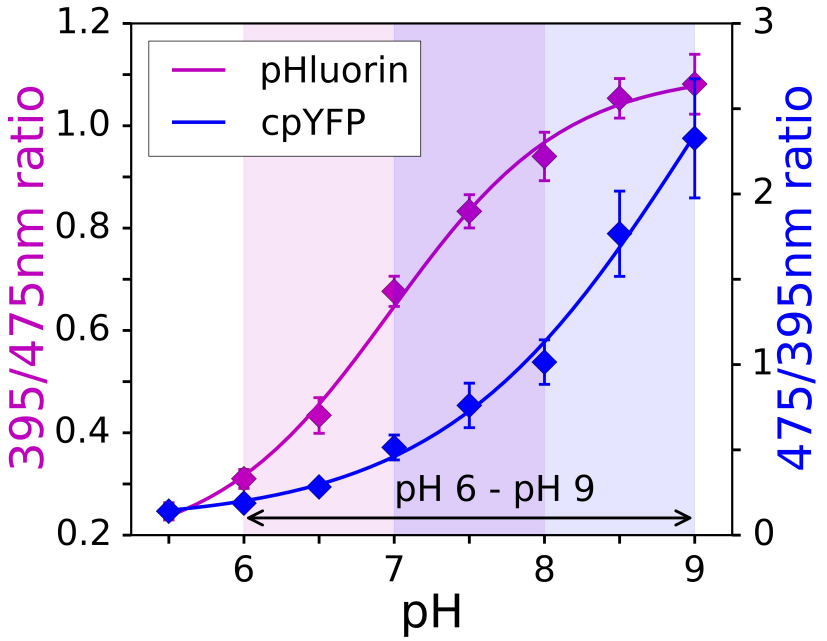

FIGURE 3.5: Calibration curves of pHluorin (magenta) and cpYFP (blue) are plotted together to illustrate the total sensitivity range. For the simplicity of comparison pHluorin and cpYFP curves are plotted in inverted axes: 395/475 nm intensity ratio for pHluorin (left axis) and 475/395 nm (right axis) intensity ratio for cpYFP

3.2.2 cpYFP

Circular permuted yellow fluorescent protein, or cpYFP, was first developed as a part of a Ca^{2+} sensing complex in eukaryotic cells where it was fused to calmodulin (CaM), a calcium-modulated protein, and M13, a 26-residue peptide derived from the CaM-binding region of the skeletal muscle myosin light-chain kinase (Nagai et al., 2001). It was later used as a sensor for superoxide in mitochondria (Wang et al., 2008; Shen et al., 2014), which, however, was demonstrated to be misleading as cpYFP was shown to be responsive to the pH change rather than superoxide presence ((Schwarzländer et al., 2014) and Fig. 3.1B). While cpYFP was previously used only in mammalian and plant cells, in this project I constructed a strain for cpYFP use in bacteria. For cpYFP-expressing strain (EK08) construction see Section 2.1.4. EK08 fluorescence is

shown in Fig. 3.6. The expression of cpYFP does not slow down bacterial growth rate, which stays roughly similar to that of the wild type MG1655 (Fig. 3.4).

cpYFP is most sensitive in a pH range 7.0-9.0 (Fig. 3.5). Thus, total pH range one can cover with pHluorin and cpYFP goes from pH 6 to pH 9. The two could be used as a control for each other in range of *E. coli*'s physiological pH (7.0-8.0), Fig. 3.5.

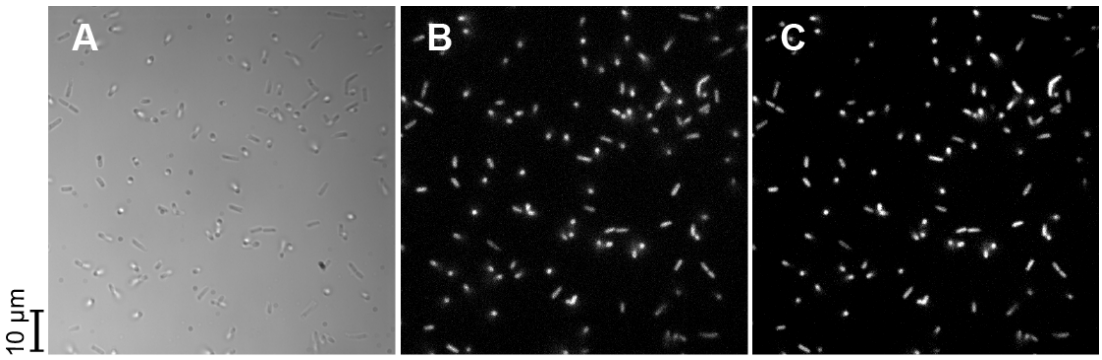

FIGURE 3.6: EK08 strain containing pWR20-cpYFP plasmid was tested for fluorescence: (**A**) bright field image; (**B**) 475 nm excitation and 510 nm emission, 50 ms exposure time and 100 gain; (**C**) 395 nm excitation and 510 nm emission, 50 ms exposure time and 100 gain. Scale bar is 10 μm.

3.2.3 pHRed

pHRed was developed for pH measurements in mammalian cells in the pH range 5.5-7.5 (Tantama et al., 2011). I tested the possibility of pHRed use in a bacterial cell.

The first system I tested was a pRSET-based vector for protein overexpression. Expression from the pRSET-pHRed plasmid required placing it into BL21 strain containing bacteriophage T7 RNA polymerase that enables transcription from T7 promoter after IPTG induction of T7 RNA polymerase expression.

Though cells were bright enough for analysis, there were inclusion bodies in the majority of cells visible both under the bright field illumination and in epifluorescence (Fig. 3.7). The cells would also lose their fluorescence upon re-culturing presumably due to the loss of the plasmid. It was decided to transfer *pHRed* gene into a different expression system. Both constitutive (pWR20) and inducible (pBAD18) expression systems were tested.

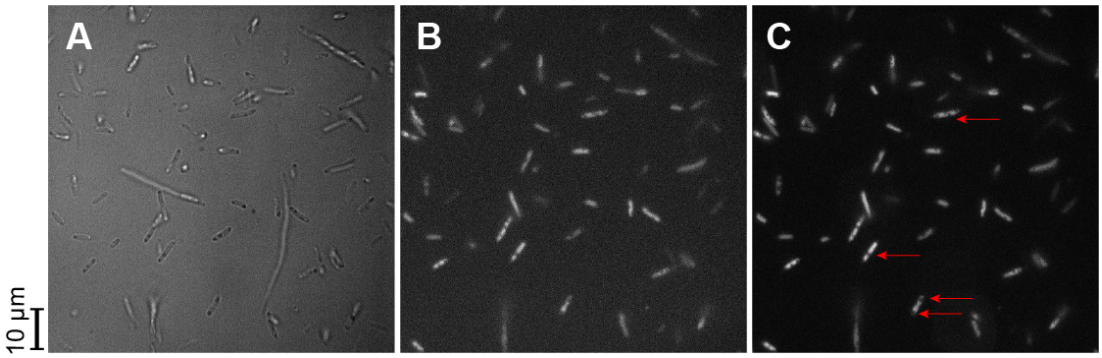

FIGURE 3.7: BL21 strain containing pRSET-pHRed plasmid was tested for fluorescence: (**A**) bright field image; (**B**) 440 nm excitation and 620 nm emission, 50 ms exposure time and 300 gain; (**C**) 580 nm excitation and 620 nm emission, 50 ms exposure time and 300 gain. Red arrows indicate location of inclusion bodies in the cell cytoplasm. Scale bar is 10 μm.

For strains construction see Section 2.1.5. pHRed-expressing strains were tested for the ability to fluoresce in the epifluorescence microscope. pWR20-pHRed did not exhibit any fluorescence. pBAD18-pHRed was induced with 0.02, 0.1 and 0.2% L-arabinose. The cells however exhibited only a weak level of fluorescence even at a highest concentration of the inducer tested (Fig. 3.8).

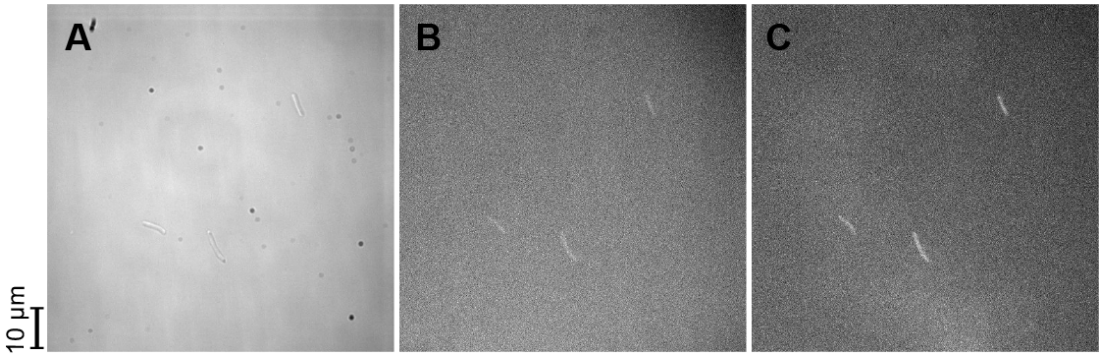

FIGURE 3.8: BW25113 strain containing pBAD-pHRed plasmid was tested for fluorescence after the induction with 0.2% L-arabinose: (**A**) bright field image; (**B**) 440 nm excitation and 620 nm emission, 50 ms exposure time and 300 gain; (**C**) 580 nm excitation and 620 nm emission, 50 ms exposure time and 300 gain.Scale bar is 10 μm.

The suggested explanation of the phenomenon was the following. pHRed being not a native protein for *E.coli* cells fails to properly fold and forms the aggregates that are visible as the inclusion bodies in the fluorescent cells. The presence of protein aggregates induces cell dormancy and inhibits the growth (Pu et al., 2018), which explains the loss of the *pHRed*-containing plasmid upon

re-culturing in inducible expression systems (pRSET) and the absence of fluorescence in the constitutive expression systems (pWR20). At the low level of expression (pBAD) pHRed production can be maintained but the fluorescence signal is too weak to be analysed. Thus, we concluded that pHRed was not suitable for pH measurements in *E. coli* cells.

3.3 Calibration *in vivo* and *in vitro*

For getting reliable *in vivo* calibration curves for the pH sensors I compared three different ΔpH collapsing agents: known protonophore carbonyl cyanide m-chlorophenylhydrazone, or CCCP (Cavari et al., 1967); the combination of weak acid potassium benzoate and weak base methylamine hydrochloride (Martinez et al., 2012a), which I will further refer to as PBMH; and indole, which has recently been proven to be a protonophore (Chimerel et al., 2012). The calibration buffers of known pH were supplemented with one of the three agents (pH was confirmed to be unchanged) and the calibration was performed as described in Section 2.4. Briefly, cells attached to the PLL-coated tunnel-slide were flushed with buffer of known pH, incubated for 1 min and imaged. The buffer was than exchanged for a next one with the different pH. The protocol was repeated for 8 buffers in the pH range 5.5-9. More than 100 individual cells were analysed for each pH value and for each uncoupling agent. The calibration curves for all three pH collapsing agents are shown in Fig. 3.9.

Though pH curves looked similar for all three agents, there was slight difference in the ratio values, which resulted in the fact that fitted curves could give an error in future pH readings $\sim$0.3 units for lower pH values and up to 0.5 units for high pH values. The spread would, thus, compromise accuracy of the potential pH measurements. The difference persisted in cases of both pHluorin and cpYFP (Fig. 3.9), though in cpYFP it influenced mostly higher pH values.

To understand the origin of this difference I checked if the incubation time was enough for the ΔpH to collapse (Fig. 3.10). The protocol was repeated as before with images taken after 1, 5 or 15 minutes incubation with each of the pH collapsing agents. From Fig. 3.10 it is clear that there is no significant dynamics of intensity ratio after the first minute of incubation and the difference in calibration curves in Fig. 3.9 cannot be explained by the incomplete pH collapse.

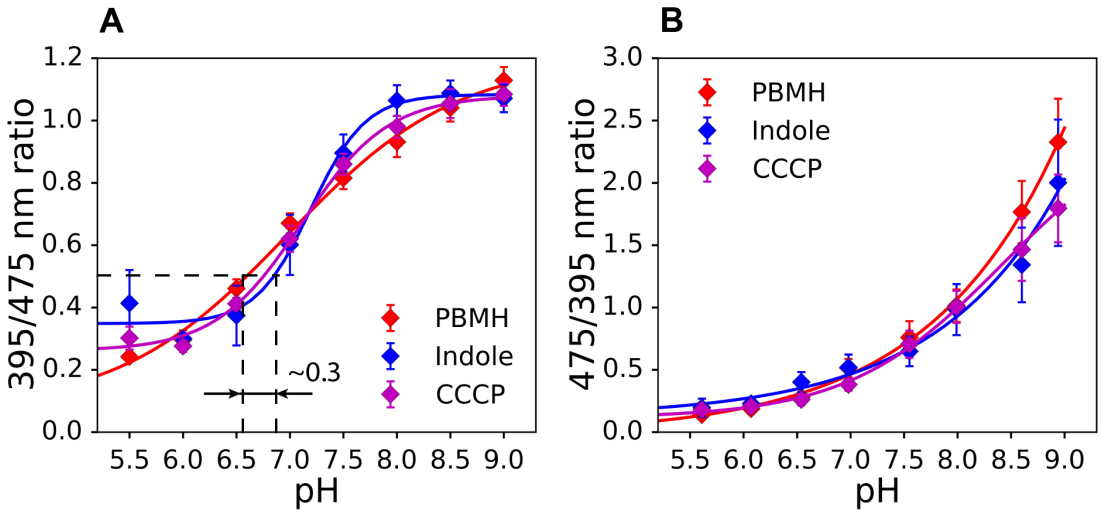

FIGURE 3.9: *In vivo* calibration curves of pHluorin (**A**) and cpYFP (**B**) with 40 mM PBMH (red), 5 mM indole (blue) or 25 μM CCCP (magenta) as ΔpH collapsing agents. Dashed lines with an arrow illustrate how difference in calibration curves can influence pH readings: for pHluorin's 395/475 nm intensity ratio of 0.5 the pH reading changes in 0.3 units range depending on the curve. Error bars show standard deviation.

After identifying that insufficient incubation time was not the issue causing difference in pH sensors calibration curves with different agents, I decided to purify pHluorin and compare *in vivo* and *in vitro* curves, while simultaneously check if pHluorin could be directly affected by the pH collapsing agents. For protein purification protocol see Section 2.2.

The purified pHluorin was diluted in buffers of known pH to 100 μg/ml concentration and imaged in the epifluorescence microscope as a uniform fluorescent field. Addition of collapsing agents did not change the calibration, which indicated that pHluorin's performance was not directly affected by any of the agents (Fig. 3.11).

The *in vitro* calibration of pHluorin could not explain the difference observed in the *in vivo* curves, and it is still not understood what caused it. However, I was able to compare the calibrations and identify the best candidate for the future experiments (Fig. 3.12) — a combination of potassium benzoate and methylamine hydrochloride (PBMH). Note, that on Fig. 3.12 the values of intensity ratio are different from those shown in Fig. 3.9. The reason is a microscope re-alignment that happened between the corresponding experiments and resulted in an increased UV light intensity in the sample plane.

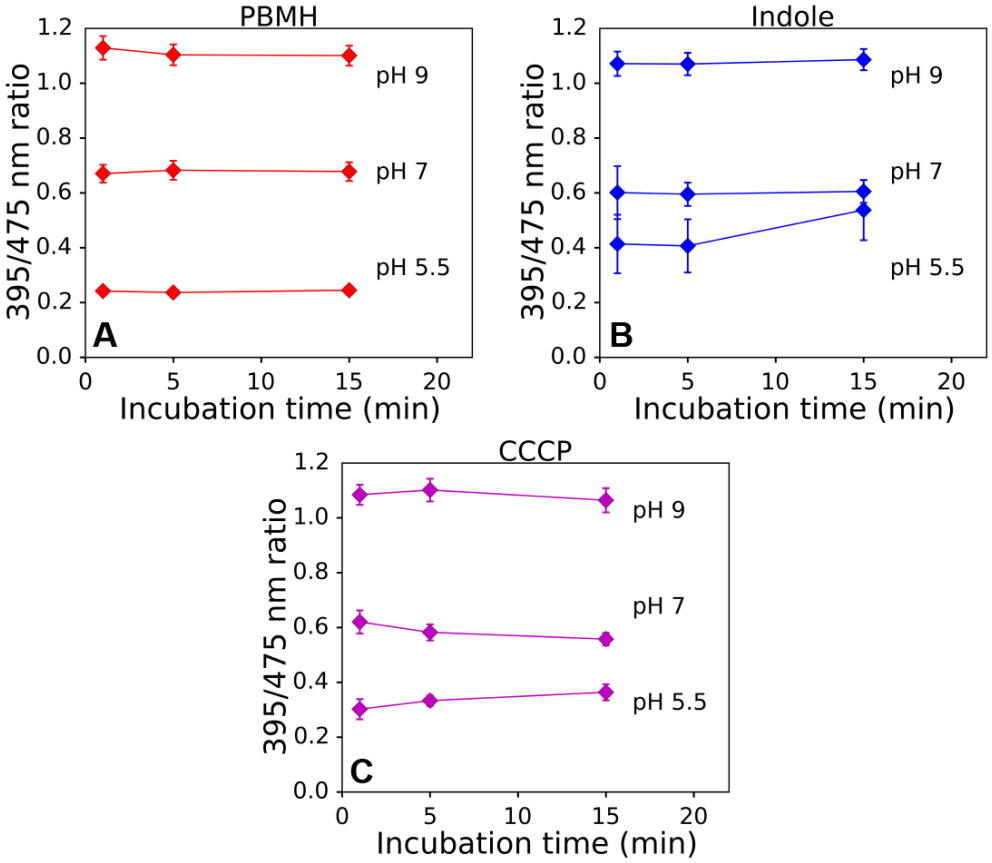

FIGURE 3.10: Dependence of pHluorin intensities ratio on the incubation time for different pH values (5.5, 7 or 9). EK07 cells pH are treated with one of the uncoupling agents and images are taken after 1, 5 and 15 minutes of incubation. Ratios in presence of PBMH are shown in red (**A**), in presence of indole in blue (**B**), in presence of CCCP in magenta (**C**), which corresponds to the colours in Fig. 3.9. Error bars are standard deviation for a population of cells.

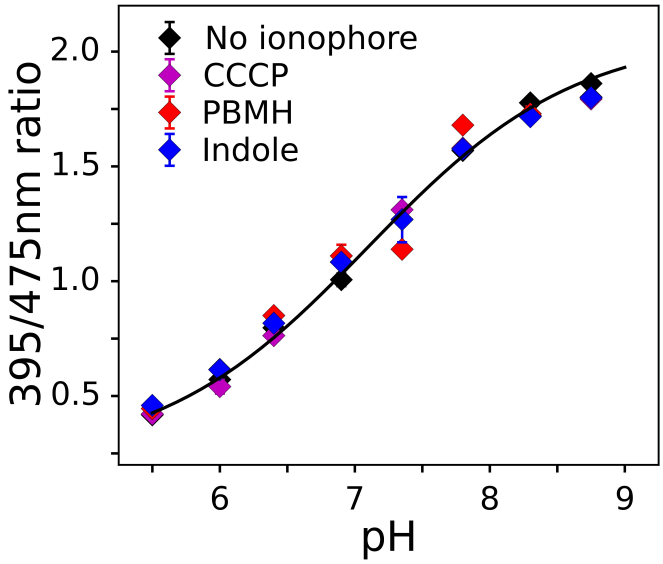

FIGURE 3.11: *In vitro* calibration curve of pHluorin with and without pH collapsing agents present. Black curve shows a true pHluorin calibration curve in buffer with no supplements. Coloured diamonds show intensity ratios measured in presence of 40 mM PBMH (red), 5 mM indole (blue) or 25 μM CCCP (magenta). Error bars show standard deviation.

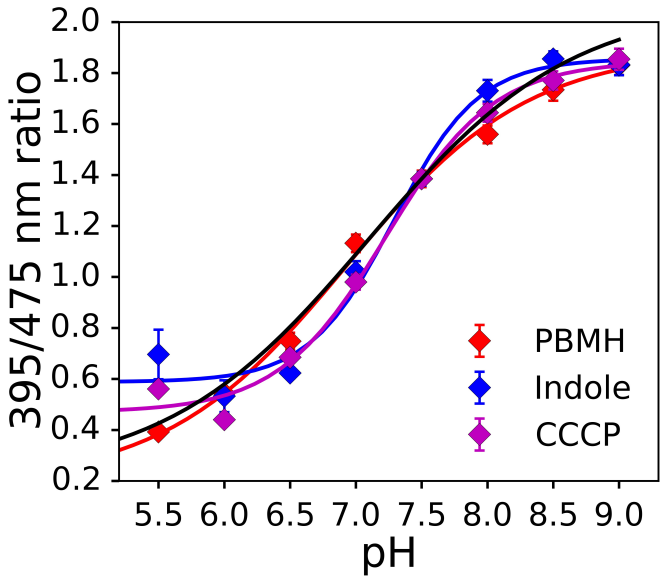

FIGURE 3.12: Comparison of *in vivo* and *in vitro* calibration curves. Black curve shows a true calibration curve of purified pHluorin in buffer with no supplements. Coloured lines show the *in vivo* curves for 40 mM PBMH (red), 5 mM indole (blue) or 25 μM CCCP (magenta) used as ΔpH collapsing agents. Error bars show standard deviation.

3.4 pHluorin and cpYFP in presence of antibiotics

To use the pH sensors to study cell's response during antibiotic or other stresses, I made sure its readings wouldn't be influenced by the stress. I tested purified pHluorin and cpYFP behaviour in presence of a variety of antibiotics (Fig. 3.13A and B). Butanol, used as a stress inducer in Chapter 4, was also checked with pHluorin (Fig. 3.13C).

The tested antibiotics included ampicillin (Ap), kanamycin (Kan), chloramphenicol (Cm), spectinomycin (Sp), nigericin (Ng) and valinomycin (Val) in the concentrations 10-20 times higher than their corresponding minimum inhibitory concentration (Salmon et al., 2000).

Purified pHluorin was diluted in the buffers of known pH (supplemented with antibiotics or 1 % butanol) to 100 μg/ml concentration and the emission intensity was measured at 510 nm for 395 nm and 475 nm excitation in Spark 10M multimode plate reader. pH of the buffers in presence of antibiotics or butanol was confirmed to be unchanged with pH meter FE20 FiveEasy^{TM} (Mettler-Toledo International Inc, Switzerland). The EK08 cytoplasm containing cpYFP was purified as described in "Materials and Methods" (Section 2.2). The cpYFP containing mixture was diluted 1:10 in the buffers of pH 5.5, 7.0 or 9 and, as for the pHluorin, antibiotics were added into the solution. Fluorescence intensity was measured at 510 nm emission for 410 nm and 475 nm excitation wavelengths.

None of the tested antibiotics were shown to influence pHluorin or cpYFP readings at any pH. Butanol, however, lowered intensity ratio at pH 7 and pH 9. For pH 7 the error was not significant considering the steepness of the calibration curve in that region, but for pH 9 located in the less sensitive part of the curve this change would need to be taken into account.

3.5 Photobleaching adjustments for fluorescent sensors

One of the advantages of the ratiometric sensors over other fluorescent probes is their insensitivity to photobleaching. Once the illumination power is adjusted so that the protein bleaches equally fast on both excitation wavelength, the ratio stays constant in time. In our setup the power was adjusted so that

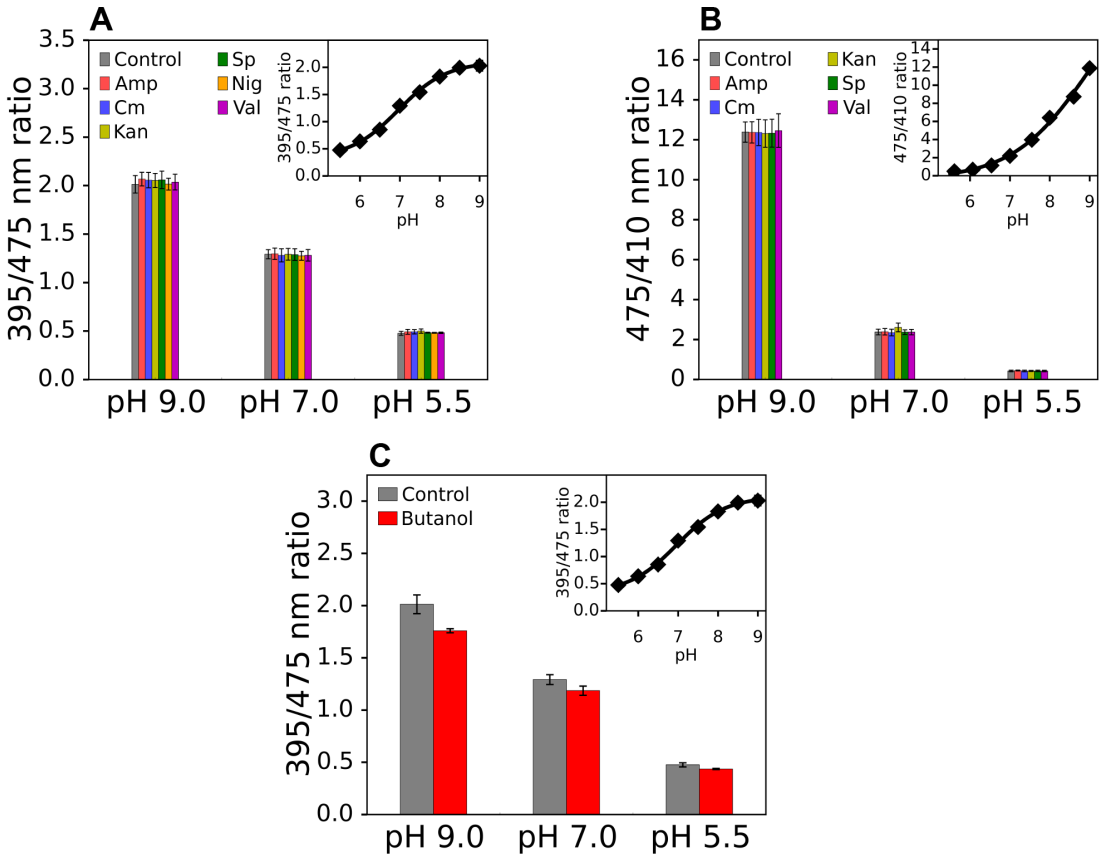

FIGURE 3.13: pHluorin (**A**) and cpYFP (**B**) performance is unaffected by the presence of antibiotics. Fluorescence intensity ratios of the purified proteins are plotted for 3 different pH values with (coloured bars) and without (grey bars) antibiotics. Error bars represent standard deviation for at least 3 independent experiments. Inlet shows the calibration curve of purified protein obtained with the plate reader. (**C**) 395/475 nm emission intensity ratio of purified pHluorin in presence of butanol at different pH. Inlet shows the calibration curve of the purified pHluorin in the plate reader. The sensitivity range of the protein goes from pH 5.5 to 8.5. pH 7 is located on the steepest part of the curve, thus, the error introduced by the presence of butanol does not change pH readings around pH 7 significantly. Error bars show standard deviation.

at 25 ms exposure time the ratio was constant. However, as discussed in Section 2.4, due to the software issues, the actual time of sample exposure to light was the sum of two components: camera exposure time and a software delay, different for the first (225 ms) and the second (55 ms) snaps. For that reason the photobleaching profiles were slightly different for different camera exposure times (Fig. 3.14) and had to be accounted for.

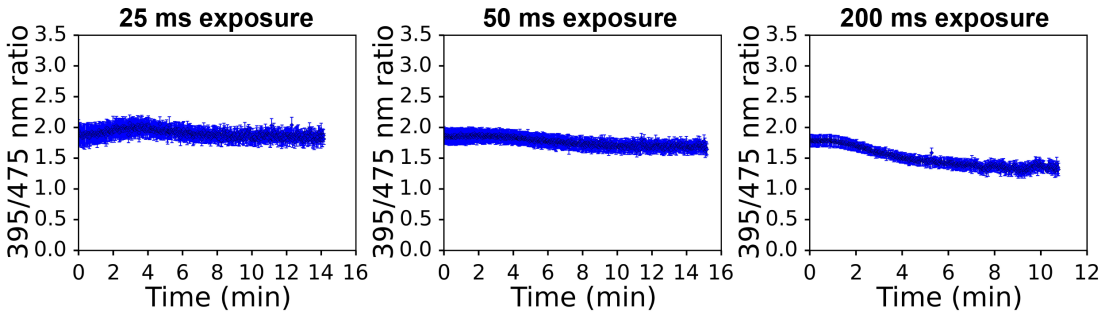

FIGURE 3.14: pHluorin intensity ratio change in time for different camera exposure times: 25 ms, 50 ms, 200 ms. Cells expressing pHluorin are treated with 5 % ethanol to collapse ΔpH and the change of the ratio intensity is defined by the photobleaching only.

To account for photobleaching, cells expressing pHluorin were treated with 5% ethanol and imaged with different exposure times in the flow-cell (Fig. 3.14). MM9 medium supplemented with 5% ethanol was constantly supplied with the syringe pump at 10 μl/min flow rate. The change in pHluorin intensities ratio was assumed to be determined by the photobleaching only as the environment stayed unchanged and cells were dead during the experiment. The bleaching adjustments coefficients were then calculated for each condition.

3.6 Cytoplasmic pH distribution in *E. coli* cells

Internal pH of *E. coli* cells is known to be maintained in a relatively narrow range of neutral pH, 7.2-7.8 (Zilberstein et al., 1984; Slonczewski et al., 1981). I tested how the cytoplasmic pH and its contribution to the PMF was changing depending on the media and on the stage of growth.

I first tried growing EK07 strain in the unbuffered LB medium widely used for bacterial studies, starting from 1:2000 dilution. The role of carbon source in LB is played by catabolisable amino acids and not sugars. It has been reported that in LB *E. coli* cells sequentially metabolise L-serine, L-aspartate,

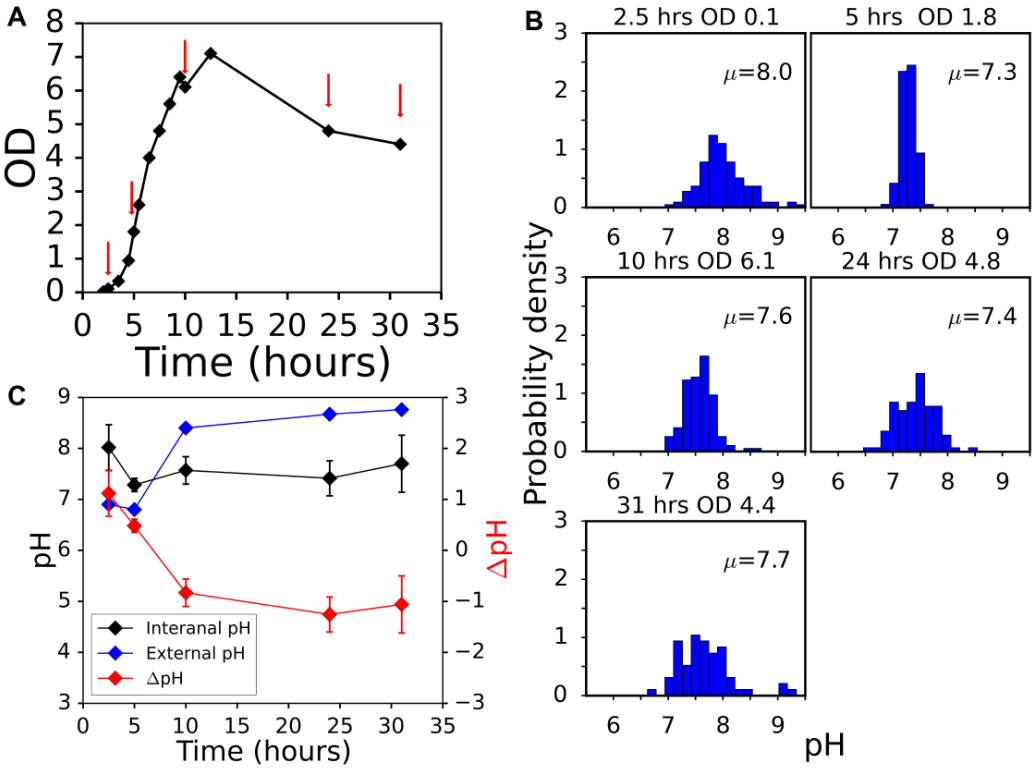

FIGURE 3.15: The intracellular pH of the EK07 strain was measured during the growth in LB medium. (**A**) Growth curve of the EK07 in LB at 37°C. Red arrows mark OD points where the cells were taken out for the intracellular pH measurements. (**B**) Cytoplasmic pH distributions at different stages of growth: exponential phase (OD 0.1 and 1.8), early (OD 6.1) and late (OD 4.8 and 4.4) stationary phases. The mean of each distribution is denoted as μ and stated on each plot. (**C**) Intracellular and extracellular pH are plotted together with the ΔpH against time. The error bars represent standard deviation of the distributions shown in **B**.

L-tryptophan, L-glutamate, glycine, L-threonine, and L-alanine (Prüss et al., 1994) and are not in a steady state (Sezonov et al., 2007). Cytoplasmic pH was measured for over 500 individual cells at different points on the growth curve (Fig. 3.15A). The resulting distributions of the internal pH at each OD are shown in Fig. 3.15B. While the internal pH was kept at a relatively stable level (7.3-7.7), the external pH increased by 2 pH units, from the initial 6.7 to 8.76. The alkalinisation of the LB in stationary *E. coli* cultures has been observed previously (Lazar et al., 1998; Molina et al., 2003) and is thought to happen due to the release of the amine-containing compounds in the medium with peptides and amino acids used as main carbon sources. The ΔpH under these conditions also undergoes 2 pH unit change, switching from positive values during exponential growth to negative in the stationary phase.

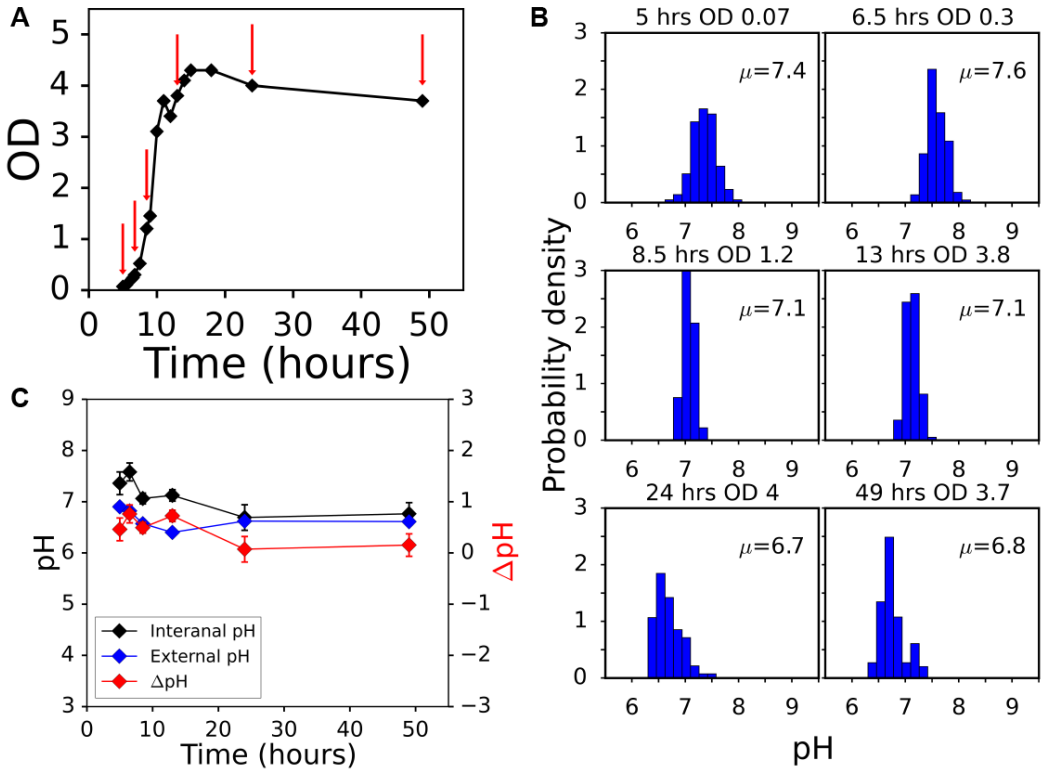

FIGURE 3.16: The EK07 intracellular pH of the EK07 strain in MM9 medium supplemented with amino acids. (**A**) Growth curve of the EK07 in MM9+aa at 37°C. Red arrows mark OD points where the cells were taken out for the intracellular pH measurements. (**B**) Cytoplasmic pH distributions of over 800 cells at different stages of growth. The mean of each distribution (μ) is stated on each plot. (**C**) Intracellular and extracellular pH are plotted together with the ΔpH against time. The error bars represent standard deviation of the distributions shown in **B**.

The same experiment was repeated for the cells growing in the buffered MM9 medium supplemented with MEM Amino Acids (Thermo Fisher Scientific Inc., USA), referred to as MM9+aa (Fig. 3.16) and unsupplemented MM9 (Fig. 3.17) with initial pH 7.

In contrast to LB, MM9 medium slightly acidified (from pH 7 to 6.6) in the course of the experiment, which was expected as the main carbon source in MM9 is glucose and the products of glucose metabolism are mainly organic acids (Bennett et al., 2009). The acidification, however, was not dramatic as the medium was buffered. While bacteria had higher growth rate and shorter lag phase in MM9+aa than in unsupplemented MM9 (Fig. 3.16A and 3.17A), the pH dynamics was similar in both media. The intracellular pH decreased by half a unit from 7.3-7.4 to 6.8-6.9 (Fig. 3.16B and 3.17B), with ΔpH almost collapsing to zero in stationary culture (Fig. 3.16C and 3.17C).

3.7 Discussion

In this chapter I examined the use of genetically encoded ratiometric pH sensors in *E. coli*.

First, I tested an existed pHluorin sensor and demonstrated that it could be used in different expression systems. In the recent work by Chakraborty *et al.* it has been pointed out that the use of inducible systems leads to the non-uniform expression of the fluorescent reporter and requires addition of the inductor to the growth medium, while constitutive expression of pHluorin results in a weak fluorescence signal (Chakraborty et al., 2017). Here, I constructed the strain that constitutively expresses pHluorin from the chromosome, does not carry an antibiotic resistance marker, has a growth rate similar to that of a wild type MG1655 and produces fluorescent intensity sufficient for single-cell pH measurements.

To extend the range of pH sensitivity to higher pH values I adapted cpYFP sensor, previously used in eukaryotic cells only, for use in bacteria. I also showed that pHRed was not suitable for the pH measurements in *E. coli* as it formed aggregates in the cell cytoplasm causing slow down of the growth rate and further loss of the plasmid. The sensors with a higher sensitivity at the lower pH values are yet to be developed.

The calibration of the sensors was performed *in vivo* and *in vitro* and three different ΔpH collapsing agents (PBMH, indole, CCCP) were compared. It

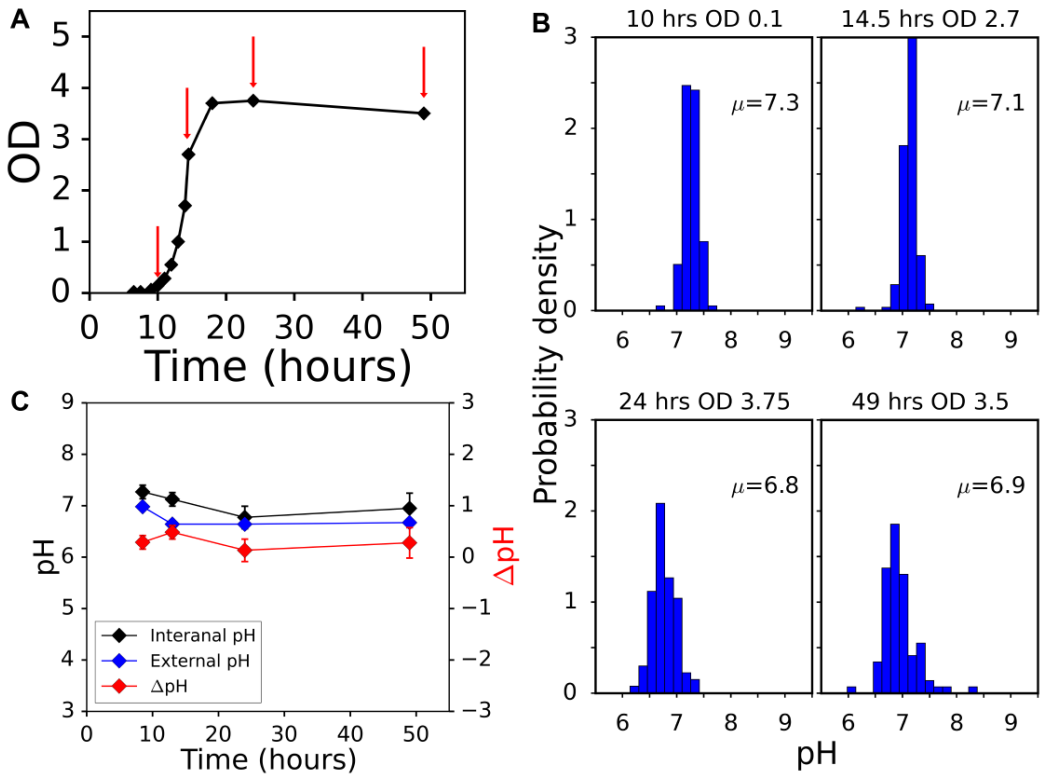

FIGURE 3.17: The EK07 intracellular pH of the EK07 strain in unsupplemented MM9 medium . (**A**) Growth curve of the EK07 in the unsupplemented MM9 at 37°C. The cells were taken out for the intracellular pH measurements at the points marked with red arrows. (**B**) Cytoplasmic pH distributions of 475 cells at different stages of growth. The means (μ) of the distributions are shown. (**C**) Intracellular and extracellular pH are plotted together with the ΔpH against time. The error bars represent standard deviation of the distributions from **B**.

was concluded that calibration with PBMH was the most accurate, though it is still not clear what causes the calibration curve deviations when other two agents are used. Additionally, both cpYFP and pHluorin were shown to be unaffected by the range of antibiotics, while butanol was demonstrated to be capable of changing pHluorin readings at higher pH values.

Finally, the cytoplasmic pH of bacteria was measured in the two most commonly used media (LB and MM9) with different primary carbon sources and different buffering capacities. Internal pH of the *E. coli* cells has been previously reported to be 7.2-7.8 (Zilberstein et al., 1984; Slonczewski et al., 1981). I tested how it changes depending on the stage of growth, starting from the early exponential phase up to a late stationary, and what it means for an overall PMF. In an unbuffered LB medium the internal pH of the cells remained stable while the external pH increased by 2 pH units making ΔpH to drop below zero. At 37°C the loss of the 2 units of ΔpH results in $\sim$120 mV loss in the total PMF. In (Lazar et al., 1998) authors suggested that the elevated pH of the LB medium in stationary *E. coli* culture was the reason of the bacterial population dying out. Indeed, the OD of the *E. coli* culture in LB dropped almost twice from the maximum value to that of the stationary culture (Fig. 3.15A). My results imply that this viability loss is accompanied by the PMF drop. It is not yet clear if the PMF loss itself could cause a cell death. Although in some cases lower energy states can enhance survival in bacteria (dormancy is one of the known mechanisms of persistence (Pu et al., 2016)), it is, however, likely that the cells with the lower PMF are more susceptible to the stresses that require active repair or pumping. This suggestion is confirmed by the fact that in the buffered MM9 medium, where ΔpH only decreases by $\sim$0.5 units ($\sim$30 mV) in stationary culture, the drop in the OD curve is much less dramatic (Figures 3.16A and 3.17A). It's also worth noticing that the average intracellular pH in stationary phase in the LB culture was $\sim$0.8-0.9 units higher than in MM9-grown culture. This indicates that though bacterium tries to minimise the negative contribution of the ΔpH to the PMF, it does not allow its cytoplasmic pH to deviate far from the range of neutral pH values. The presence of the amino acids in the medium did not influence the internal pH dynamics during the growth.

Chapter 4

Bacterial flagellar motor as a single-cell "voltmeter" reveals the mechanisms of stress induced damage

Part of the work presented in this Chapter is published as arXiv:1809.05306.

4.1 Introduction

To stay alive bacteria, like other cells, maintain adequate supplies of free energy. Under various external stresses bacteria attempt to stay viable by distributing the available energy to processes essential for coping with the challenge, while simultaneously maintaining core cellular functions. The two main sources of the free energy in the living cells are adenosine triphosphate (ATP) molecule and proton motive force (PMF). The two are interlinked, ordinarily PMF is used to synthesise ATP, but ATP can drive the production of PMF as well (Keis et al., 2006).

As early as 1791 Luigi Galvani proposed that life processes generate electricity (Galvani, 1791; Green, 1953). However, it took more than a century for Hugo Fricke to measure the capacitance of the biological membrane (Fricke, 1923) and for Peter Mitchell to explain that the PMF is an electrochemical gradient of protons across the membrane that powers the production of ATP

(Mitchell, 1961). PMF consists of the two components: pH difference between cytoplasm and environment (ΔpH=pH_{in}-pH_{out}), and the electrical potential across the membrane (V_m), which is formed by the build up of charge occurring at $\sim$ nm-thin layer close to the biological membrane (Nelson, 2003).

$$PMF = V_m - \frac{2.3RT}{F}\Delta pH \tag{4.1}$$

where R is the gas constant, T is the temperature and F is the Faraday constant.

Since life generates electricity used to power its processes and membrane acts as a capacitor, it is reasonable to represent the rest of the cell components with an electrical circuit analogy (Van Rotterdam et al., 2002; Walter et al., 2007) (Fig. 4.1). Then, proton fluxes across the membrane can be considered as currents, oxidative or substrate-level phosphorylation as an imperfect battery with non-zero internal resistance, and the membrane as resistor and capacitor connected in parallel. If external pH equals that of the bacterial cytoplasm, and for *E. coli* the latter is known ((Slonczewski et al., 1981; Zilberstein et al., 1984; Wilks et al., 2007) and Chapter 3), V_m in the circuit equals the PMF.

The circuit analogy in Fig. 4.1 gives a mathematical framework helping to understand cellular free energy maintenance in a range of different conditions. For example, it can give a prediction for changes in V_m when circuit parameters change: a battery depends on the available carbon source and internal resistance R_i increases in presence of electron transport chain inhibitors (such as sodium azide (Noumi et al., 1987)). Furthermore, if one could measure V_m with an equivalent of a "voltmeter" it would be possible to uncover the mechanism and dynamics of the damage as the cells are exposed to various external stresses, as well as obtain functional dependency between circuit parameters and the amplitude of the stress.

In this chapter I report the use of bacterial flagellar motor as such a "voltmeter" and reveal the mechanisms of the damage caused by chosen stresses, demonstrating that the approach of combining high-precision PMF measurements and the "electrical circuit interpretation" of the cell's energetics serves as a powerful tool to quantitatively describe the effect of an unknown stress on the cells' physiology.

4.2 Circuit interpretation of the *E. coli* cell

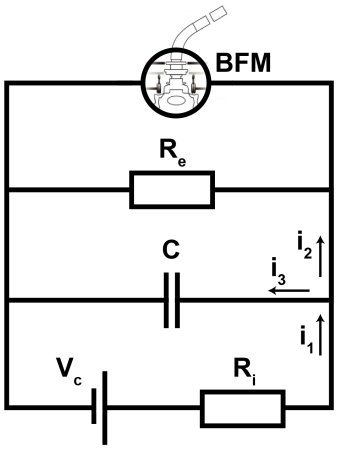

FIGURE 4.1: Electric circuit equivalent of an *E. coli* cell. Oxidative (or substrate-level) phosphorylation is shown as an imperfect battery V_c with an internal resistance R_i, and the membrane with capacitance C and resistance R_e. Arrows i_1, i_2 and i_3 represent currents in the circuit. Bacterial flagellar motor (BFM) plays a role of the "voltmeter", allowing the measurements of the electrical potential drop across the cell membrane, as its rotational speed is proportional to the PMF and its own resistance is much higher than the R_e.

The electric circuit analogy (Fig. 4.1) gives a mathematical framework needed to understand cellular free energy maintenance in a range of different conditions. For example, under given external stress it allows me to discern the affected component of the cell and predict the mechanism of damage caused by the stress in the following manner.

Membrane capacitance is set by the geometry of the lipid bilayer and unlikely to be altered on the minute-time-scale of the experiment.

I define V_c as a theoretical maximum potential a cell can generate in a given environment and from a given internalised (carbon) source. This definition suggests that the V_c is fully determined by the availability of the resources for energy production. Stress can affect V_c only by damaging specific carbon transporters and, thus, is media-dependent. Furthermore, in starvation buffer where *E. coli* uses internal carbon sources (Nyström et al., 1998) V_c will not be changed by the stress.

R_i defines the inefficiency of the catabolism, comprising the drop from V_c as a specific carbon source gets metabolised via a large number of catabolic enzymes. These enzymes are at least partially carbon source specific, thus the

stress that targets R_i will be media-dependent. Moreover, it is reasonable to assume that cells will be less sensitive to the stresses that target R_i in a less rich medium, due to the excess of the catabolic enzymes compared to the limited amount of nutrients.

Finally, while the R_e on the long time scales (during cell growth) is defined by the growth medium, just like the C, the membrane targeting stresses that influence R_e rapidly (within minutes) will be media-independent.

Once the affected component is pinned down , I employ Kirchhoff's laws to express it as a function of stress-induced membrane potential change ($V_m/V_{m,0}$), which I measure using bacterial flagellar motor (BFM) as a "voltmeter" (Fig. 4.1).

BFM is a nano-machine that enables bacterial swimming (Sowa et al., 2008) via PMF powered rotation (Manson et al., 1980; Matsuura et al., 1977; Meister et al., 1987; Fung et al., 1995). The motor speed (ω), usually reaching couple of hundred Hz (Lowe et al., 1987), varies linearly with the PMF (Fung et al., 1995; Gabel et al., 2003). While BFM can be actively slowed down, e.g. when cell enter stationary phase (Amsler et al., 1993), on shorter time scales the linearity between the motor speed and PMF allows me to use the motor speed as a PMF indicator, and when pH_{in}=pH_{out} as a V_m indicator as well. Here, unless stated otherwise, I will only consider the situation where Δ pH$\approx$0, which I set by adjusting the external pH to known internal pH of the *E. coli* (Slonczewski et al., 1981). In addition, EK07 strain I constructed (see Section 2.1) carries a chromosomal copy of the gene encoding pHluorin protein, which I use to monitor the internal pH during the experiments. I thus have:

$$\omega = \xi \cdot PMF = \xi \cdot V_m \tag{4.2a}$$

$$\frac{\omega}{\omega_0} = \frac{PMF}{PMF_0} = \frac{V_m}{V_{m,0}} = f(S,t) \tag{4.2b}$$

where I assume that ω changes as a function of stress amplitude and time $f(S,t)$, ξ is a constant and index 0 denotes the variable value prior to stress. I measure ω using back-focal-plane interferometry (Svoboda et al., 1993) and a polystyrene bead attached to a short filament stub (see Section 2.4).

Another important feature that allows flagellar motor to play a role of the "voltmeter" is that its own resistance is much higher than the overall resistance of the cell. The total resistance of the bacterial membrane is $\sim 10^8 - 10^{10}$ Ohm (Miyamoto et al., 1967; Chimerel et al., 2012), if I assume cell area to

be $\sim 10^{-7}$ cm^2. The resistance of the motor can be estimated as follows. The proton flux through the motor is found to be 1240±240 protons per revolution (Meister et al., 1987). Taking the highest values of the PMF as 200 mV and the rotational frequency as 200 Hz, I arrive to the lowest estimate of the motor resistance to be $\sim 10^{12}$ Ohm, which is at least two orders of magnitude higher than the overall resistance of the bacterial membrane.

Using equation (4.2b) and the circuit analogy I can express each circuit component as a function of stress, while measuring $f(S,t)$ via ω/ω_0. When the system is in equilibrium current trough the capacitor $i_3 = 0$. Upon application of a given stress one of the three components of the circuit change (R_i, V_c or R_e), and all three currents become non zero. Then, based on Kirchhoff's laws I have:

$$V_c = i_1 R_i + i_2 R_e, \tag{4.3a}$$

$$i_1 = i_2 + i_3, \tag{4.3b}$$

$$i_2 R_e = \frac{Q}{C}, \tag{4.3c}$$

where Q is the charge on the capacitor plates (or charge on the membrane).

I will further consider scenarios where only one circuit element changes at a time. I will first consider the case when overall membrane resistance, R_e, changes, i.e. membrane has been damaged, and R_i, V_c and C are kept fixed. To get the functional dependence of R_e on the stress amplitude I need to express it via $V_m/V_{m,0}$. Based on the Ohm's law membrane voltage can be expressed as $V_m = i_2 R_e$. Thus,

$$\frac{R_e}{R_{e,0}} = \frac{V_m}{V_{m,0}} \cdot \frac{i_{2,0}}{i_2} \tag{4.4}$$

where $i_{2,0}$ is the current through $R_{e,0}$, i.e. before R_e changed. I am now looking for expressions for $i_2(R_e, t)$ and $i_{2,0}$. The current through the capacitor is $i_3 = dQ/dt$ and thus from (4.3c) follows:

$$\frac{di_2}{dt} R_e + i_2 \frac{dR_e}{dt} = \frac{i_3}{C} \tag{4.5}$$

I express i_3 from (4.5) and i_1 from (4.3b) and apply it to (4.3a) to get the expression for $i_2(R_e, t)$:

$$\frac{di_2}{dt} + i_2 \frac{R_i + R_e + CR_i \frac{dR_e}{dt}}{CR_iR_e} - \frac{V_c}{CR_iR_e} = 0 \tag{4.6}$$

When $i_3 = 0$, $i_{2,0} = i_{1,0} = i_0$ based on equation (4.3b). By implementing it to (4.3a) I get:

$$i_0 = \frac{V_c}{R_i + R_{e,0}} \tag{4.7}$$

because V_c and R_i do not change during the application of the stress. Using (4.2b) and (4.7) I can now express (4.4) as:

$$\frac{R_e}{R_{e,0}} = f(S,t) \cdot \frac{V_c}{R_i + R_{e,0}} \cdot \frac{1}{i_2(R_e, t)}, \tag{4.8}$$

where $i_2(R_e, t)$ is a solution of (4.6). Alternatively, if the stress-affected element is R_i or V_c, equation (4.5) and (4.6) become:

$$\frac{di_2}{dt} R_e = \frac{i_3}{C} \tag{4.9}$$

$$\frac{di_2}{dt} + i_2 \frac{R_i + R_e}{CR_iR_e} - \frac{V_c}{CR_iR_e} = 0 \tag{4.10}$$

I now simplify the electric circuit by estimating the RC constant of the cell membrane. Capacitance and resistance of the bacterial membrane have been reported as C ~1 μF/cm^2 (Fricke et al., 1956; Hodgkin et al., 1952) and R_e ~10-1000 Ohm·cm^2 (Miyamoto et al., 1967; Chimerel et al., 2012), which gives RC in the range of 10^{-5} to 10^{-3} s. Thus, the current through the capacitor is zero prior to the stress application (when the system is in steady-state), as well as post stress application when $t > 1$ ms (i.e. on the time scales of my experiment). Next I consider ΔG of NADH oxidation with a stoichiometry of 6 H$^+$ per electron pair, and compute that respiratory chain can produce V_c ~-360 mV (Walter et al., 2007). Yet, physiological value of the membrane potential of respiring bacteria is approximately equal to -160-230 mV (Collins et al., 1976; Tran et al., 1998), indicating that roughly half of the membrane potential drops at the internal resistance, i.e. $R_{i,0} \approx R_{e,0}$. Taking the two simplifications into account I arrive to:

$$i_1 = i_2 = \frac{V_c}{R_i + R_e} \tag{4.11}$$

and

$$f(S,t) = \frac{V_m}{V_{m,0}} = \frac{V_c \cdot R_e}{R_i + R_e} \cdot \frac{R_{i,0} + R_{e,0}}{V_{c,0} \cdot R_{e,0}} = \frac{V_c \cdot R_e}{R_i + R_e} \cdot \frac{2}{V_{c,0}} \tag{4.12}$$

Then, if R_e is affected by the stress, $V_c = V_{c,0}$ and $R_i = R_{i,0} = R_{e,0}$

$$\frac{V_m}{V_{m,0}} = \frac{2 \cdot R_e}{R_e + R_{e,0}} = f(S,t) \tag{4.13}$$

If R_i is affected by the stress, $V_c = V_{c,0}$ and $R_e = R_{e,0} = R_{i,0}$

$$\frac{V_m}{V_{m,0}} = \frac{2 \cdot R_{i,0}}{R_i + R_{i,0}} = f(S,t) \tag{4.14}$$

Finally, if V_c is affected by the stress, $R_e = R_{e,0} = R_i = R_{i,0}$

$$\frac{V_m}{V_{m,0}} = \frac{V_c}{V_{c,0}} = f(S,t) \tag{4.15}$$

Equations (4.13)-(4.15) will now allow me to relate the observed changes in the motor speed with the changes in the circuit components. I note here that the assumption behind the current model is that there is always a component, which is affected the most providing a major contribution in the change of the proton motive force. The model does not allow me to resolve scenarios where more than one component changes at a time.

4.3 PMF dynamics analysis confirms indole is an ionophore

The proposed circuit analogy and applicability of the BFM speed as the voltmeter were first tested on a known membrane stress — a cell signalling molecule indole that at millimolar concentrations acts as an ionophore (Chimerel et al., 2012). Ionophores are molecules that carry ions across the lipid bilayer, thus the membrane resistance is expected to decrease (and ion conductance to increase) in the presence of indole in the medium. Furthermore, it has been previously demonstrated that membrane conductance depends parabolically on indole concentration assuming that indole molecules form dimers (Chimerel et al., 2012).

Fig. 4.2A shows examples of individual motor speed recordings prior, during and post treatment with a given concentration of indole. Motor speed dropped immediately with the addition of indole, and stayed at approximately the same level until indole was removed, at which point it recovered to the initial level. The speed change caused by indole was rapid (within experimental resolution of 10 ms), confirming the estimate of membrane RC constant, and justifying the assumption that the current through the capacitance in Fig. 4.1 circuit is negligible. Fig. 4.2E shows the internal pH of the cells treated with 0.5 and 2.5 mM indole respectively, confirming that during the experiment $\Delta\text{pH} \approx 0$.

Fig. 4.2B shows the mean speed traces for different indole concentrations (see Section 2.5.2 for mean speed calculation) and in Fig. 4.2C the probability densities of preshock and shock speeds are plotted. From the Gaussian fits to preshock and shock speed distributions I obtained mean shock speeds for a given indole concentration, and plotted them normalised to the preshock speed, Fig. 4.2D. I fitted the normalised speeds with hyperbolic ($y = \frac{1}{Kx+1}$) or quadratic hyperbolic ($y = \frac{1}{Kx^2+1}$) function, both of which yielded good quality fits (R^2 higher than 90%). According to (Chimerel et al., 2012) the concentrations of indole at which the quadratic dependency becomes particularly obvious are higher than 2.5 mM, where I used 0-2.5 mM range. Thus, my results are consistent with previous findings and confirm the accuracy of the proposed approach.

4.4 Butanol acts as an ionophore, changing membrane conductance linearly with concentration.

To determine the mechanism of action of an unknown stress I chose butanol. Previous work indicates that butanol interacts with cell membrane and weakens it, but the exact mechanism is unknown (Fletcher et al., 2016).

I performed the PMF measurements in *E. coli* cells treated with butanol. The experimental protocol of butanol delivery was the same as for indole. Fig. 4.3A and 4.3B show examples of raw traces and mean speed traces prior, during and post butanol shock. Fig. 4.3E shows the internal pH of the cells during

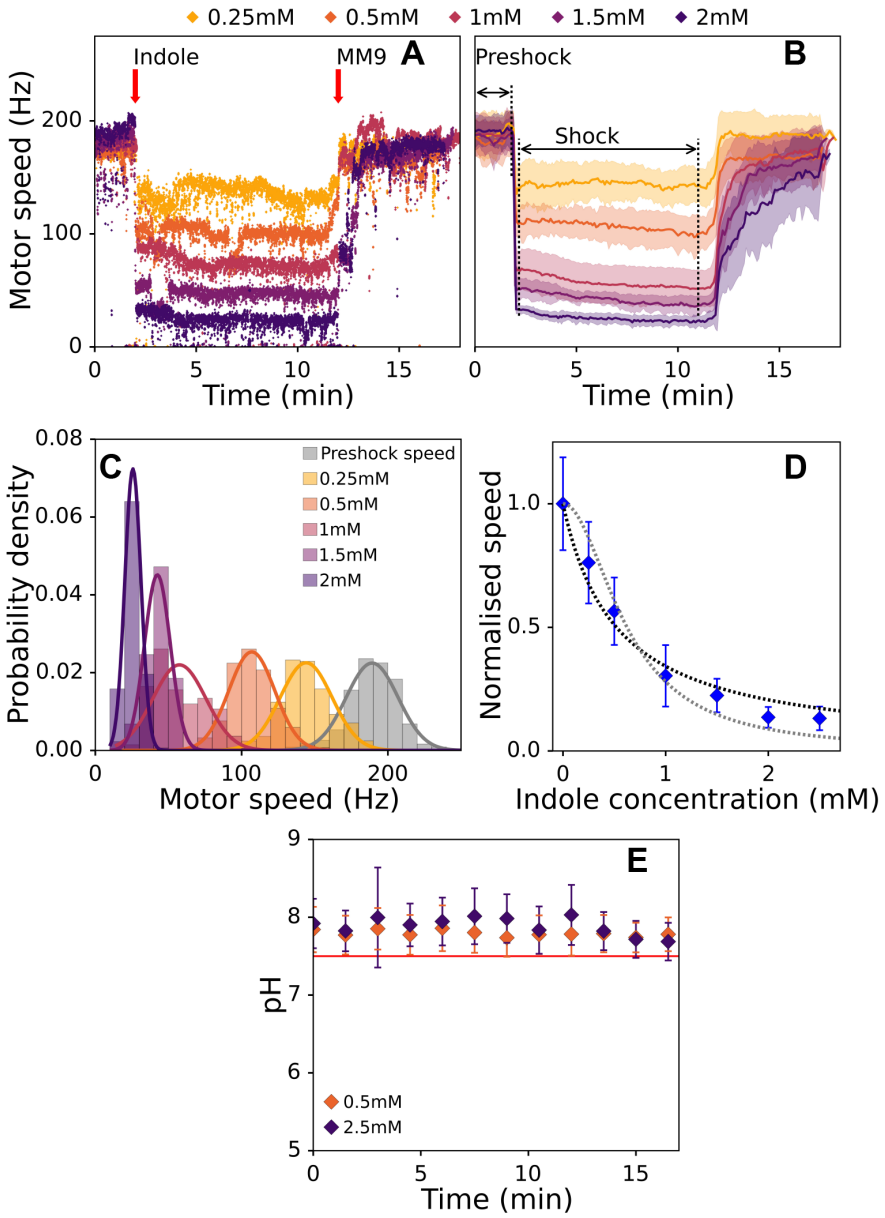

FIGURE 4.2: BFM speed drops rapidly and increasingly with increasing indole concentration (**A**) Examples of raw motor speed traces at 5 different indole concentrations. Indole was delivered into the tunnel-slide 2 min after the recording commenced, and removed after 12 min. (**B**) Mean speeds of n⩾20 motor speeds for each indole concentration are shown against time. Preshock speed was calculated for time interval between 0 and 110 s (indicated in the figure) and shock speeds from 130 to 660 s of the motor recording. Standard deviation is shown as a shaded region. (**C**) Experimental motor speed data for each indole concentration was fitted with a Gaussian probability density function using Maximum Likelihood Estimate (MLE). (**D**) Normalised BFM speeds plotted against indole concentration. Error bars represent standard deviation. Black dotted line shows hyperbolic fit and grey quadratic hyperbolic fit, $R^2 = 0.97$ and $R^2 = 0.95$ respectively. (**E**) Cytoplasmic pH measurements during treatment with 0.5 mM and 2.5 mM indole with standard deviation.

0.5% and 1% butanol treatment, which stayed approximately the same as the external medium.

As for indole, immediately upon butanol stress motor speed dropped, and upon butanol removal it recovered to the initial value, Fig. 4.3A. Motor speed distributions at a given butanol concentrations remained narrow, and I fitted them with Gaussian curves (Fig. 4.3C). Fig. 4.3D shows normalised motor speeds, calculated as mean values of the distributions given in Fig. 4.3C, and plotted against butanol concentration for both MM9 media and phosphate buffered saline (PBS).

The relative speed drop observed in the presence of butanol was media independent, and alike that observed for indole. The finding suggesting that, on the time scale of the experiment, butanol causes non-permanent membrane damage and acts as an ionophore. The normalised motor speed dependence on butanol concentration is hyperbolic. I, thus, obtain equation (4.13) for butanol and learn that butanol concentration and membrane resistance are inversely proportional:

$$R_e = \frac{R_{e,0}}{7.8 \cdot c_{but} + 1} \tag{4.16}$$

where c_{but} is a butanol concentration in percent (%) and 7.8 is a dimensionless experimental constant obtained from the hyperbolic fit and equation (4.13). It could now be estimated that the membrane potential would drop below 5% of the initial level upon addition of $\sim 5\%$ butanol.

I also observed the speed restoration after butanol removal even after multiple treatments of the same cell. Fig. 4.4 shows several consecutive butanol stresses each lasting 60 s (A) or 30 s (B). After each treatment motor speed was fully restored.

To ensure there was no unspecific response due to the media exchange I performed the control experiment flushing MM9 medium containing no butanol or indole (Fig. 4.5). The motor speed stayed constant during the control flushes indicating that the speed changes observed in the main experiments were solely due to the presence of indole or butanol in the medium.

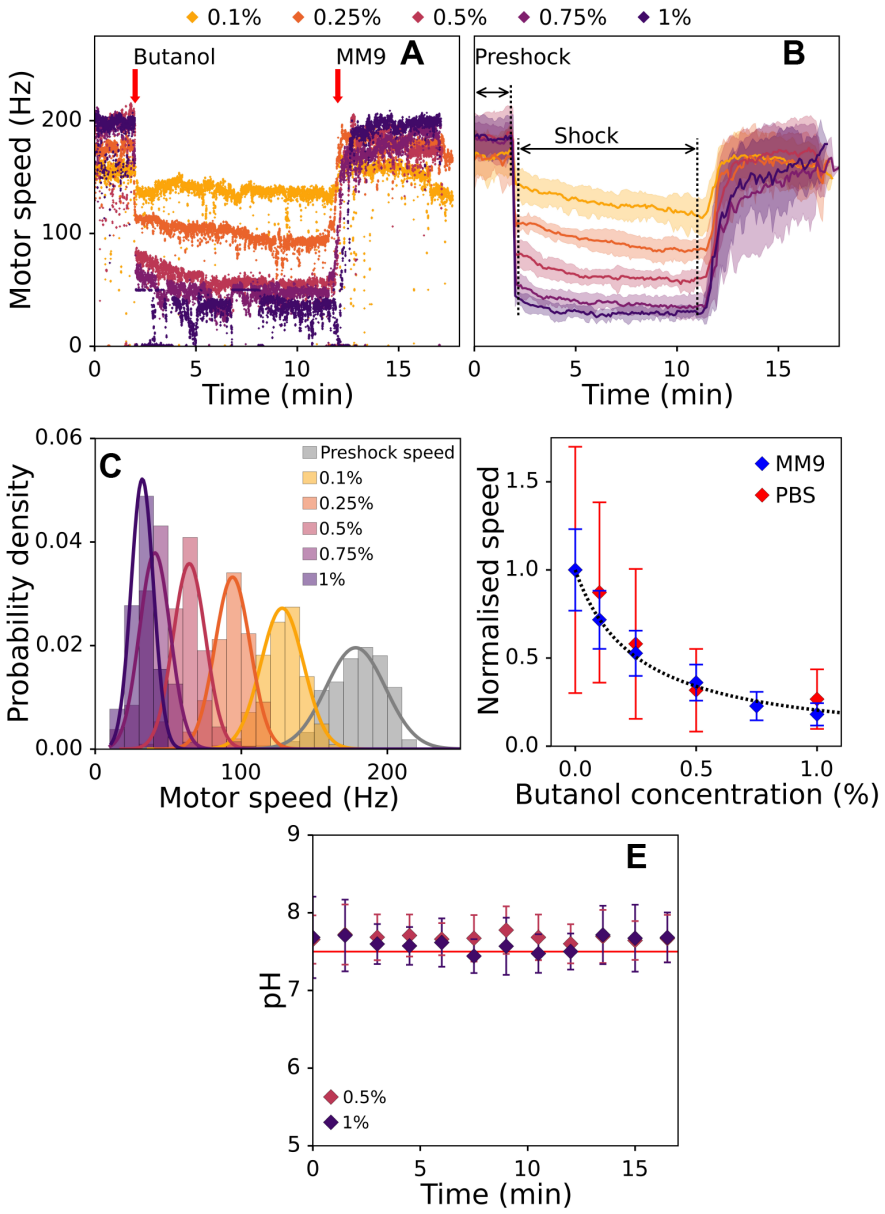

FIGURE 4.3: BFM speed dropped sharply and reversibly after butanol treatment. (**A**) Examples of raw BFM speed traces for 5 different butanol concentrations. Butanol was delivered 2 min into the recording and removed after 12 min. (**B**) Mean speeds of n⩾20 cells per different butanol concentrations are plotted against time. Preshock and shock speeds were calculated in the 0 to 110 s, and 130 to 660 s time interval, respectively. Standard deviations of the mean are given as shaded regions. (**C**) Probability densities of shock speed for each butanol concentration and the preshock speed are fitted using MLE. (**D**) Shock speeds obtained from the distributions are normalised by the preshock speed and plotted against butanol concentration. Blue diamonds show cells in MM9 media and red diamonds cells in PBS. Error bars represent standard deviation. Hyperbolic fit is given as a black dotted line (R^2 = 0.96). (**E**) Cytoplasmic pH measurements during treatment with 0.5 % and 1 % butanol. Error bars represent standard deviation.

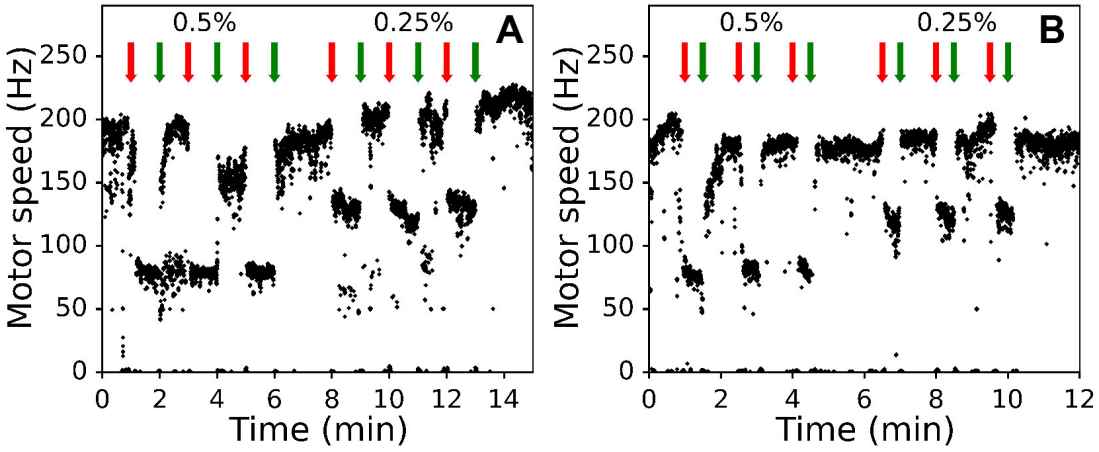

FIGURE 4.4: Motor speed was reversible during multiple butanol shocks. Butanol was flushed in at the time denoted with red, and out with green arrow. First three treatments were done with 0.5%, and subsequent three with 0.25% butanol. Intervals between butanol and MM9 flushes were of (**A**) 1 min, or (**B**) 30 s duration.

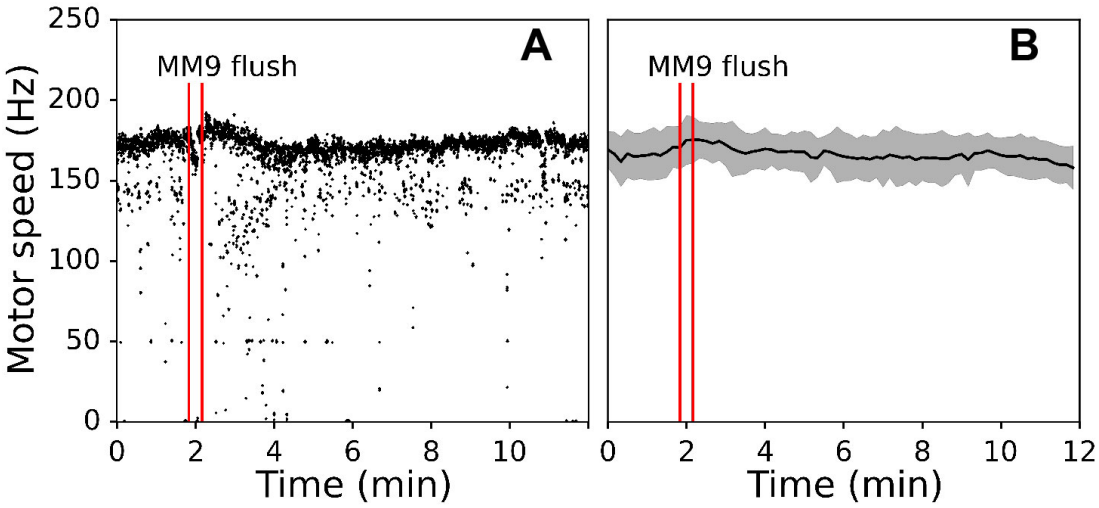

FIGURE 4.5: Solely exchanging media did not affect the motor speed. (**A**) Motor speed of a cell in the tunnel-slide was recorded for 2 min, at which point fresh MM9 was flushed into the tunnel (red vertical lines indicate the duration of the flush). (**B**) Mean trace with standard deviation (shaded) of 9 cells exposed to the MM9 exchange as in (**A**).

4.5 Photodamage increases membrane conductance that scales with the light power

Next I characterised light induced damage. While previous reports indicate that light causes wavelength dependent damage to bacterial cells (Ashkin et al., 1987; Neuman et al., 1999), they also suggest that the nature of damage is complex. Most likely the cause of the damage is the formation of reactive oxygen species (ROS) (Jager et al., 2017; Lockwood et al., 2005), which have been shown to perturb multiple components of the cell: DNA, RNA, proteins and lipids (Cabiscol et al., 2000; Zhao et al., 2014).

To apply light of a certain wavelength and intensity to bacterial cells I used a flow-cell (Section 2.4). During the light exposure cells were continuously supplied with fresh media at 10 μl/min flow rate. The light of 395 nm and 475 nm wavelengths was chosen to allow me to simultaneously measure internal pH of bacteria.

Fig. 4.6A shows example BFM speed traces during exposure to light of different effective powers. The light at 395 nm and 475 nm was applied in a series of pulses, each of a given duration and with a given interval; effective power was the sum of the two. By changing either the duration of the pulse or the interval between them, I changed the effective power (P_{eff}) delivered to cells. P_{eff} was calculated as the total energy delivered divided by the total time the light was on (Section 2.4). Fig. 4.6A shows that BFM speed gradually decreased in time during exposure to light and that the decrease rate scaled with the P_{eff}, also visible in Fig. 4.6B showing mean BFM speed traces for the same four effective powers. Fig. 4.6E shows internal pH of the cells, which stayed approximately the same as the external medium.

To identify the functional dependency of the speed decrease rate on P_{eff} I fitted individual normalised traces with the simple exponential function: $\omega/\omega_0 = e^{-\alpha t}$, with the single fitting parameter α. Mean of the fits with standard errors at corresponding four different powers are shown in Fig. 4.6C, and Fig. 4.6D shows fit coefficient α plotted against the light power. To confirm that the observed speed drop was primarily due to the changes in membrane resistance, R_e, I repeated the experiment in PBS. Unlike in MM9 medium, in PBS cells did not have any nutrients available. Consistently with that, the initial

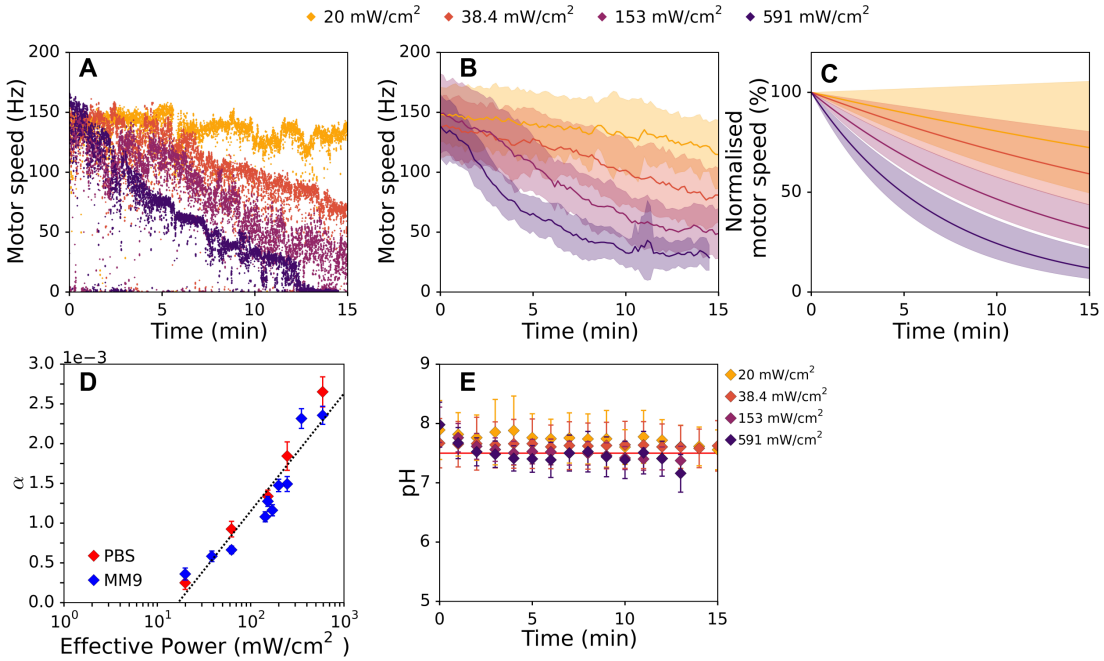

FIGURE 4.6: Rate of motor speed decay increased with the light power. (**A**) Examples of raw traces at four different effective powers, P_{eff} = 20, 38.4, 153 or 591 mW/cm^2. (**B**) Mean BFM speed at different illumination powers (21 to 34 cells are recorded per condition). (**C**) Averaged exponential fits for different illumination powers with standard deviation. Each individual motor trace was fitted with an exponential function and the mean of fitting parameter α was calculated for each P_{eff}. (**D**) Exponential fit coefficient α is plotted against illumination power. Blue diamonds show cells in MM9 media and red diamonds cells in PBS (Section 2.4). Error bars represent standard error and dotted line the logarithmic fit (R^2 = 0.906). The total number of cells in MM9 was 277 and in PBS 116. (**E**) Cytoplasmic pH measurements during the photodamage experiments. Error bars represent standard deviation, marker colours correspond to the speed trace colours in **A**.

motor speed in the PBS was approximately twice lower than in MM9. However, despite the lack of nutrients in PBS, cells coped with the light damage in the similar way as in glucose medium, in agreement with the assumption that on the times scales of my experiment light affects primarily the membrane resistance R_e. Together with the fact that the speed decrease rates stayed the same at a given P_{eff}, the finding suggested that on the time scale of the experiment there was no active membrane repair. I further confirmed this finding by measuring the motor speed after I exposed cells to the light for shorter periods of time. Fig. 4.7 shows that when the illumination ceased after 5 or 15 min the (decreased) BFM speed remained the same with no visible recovery.

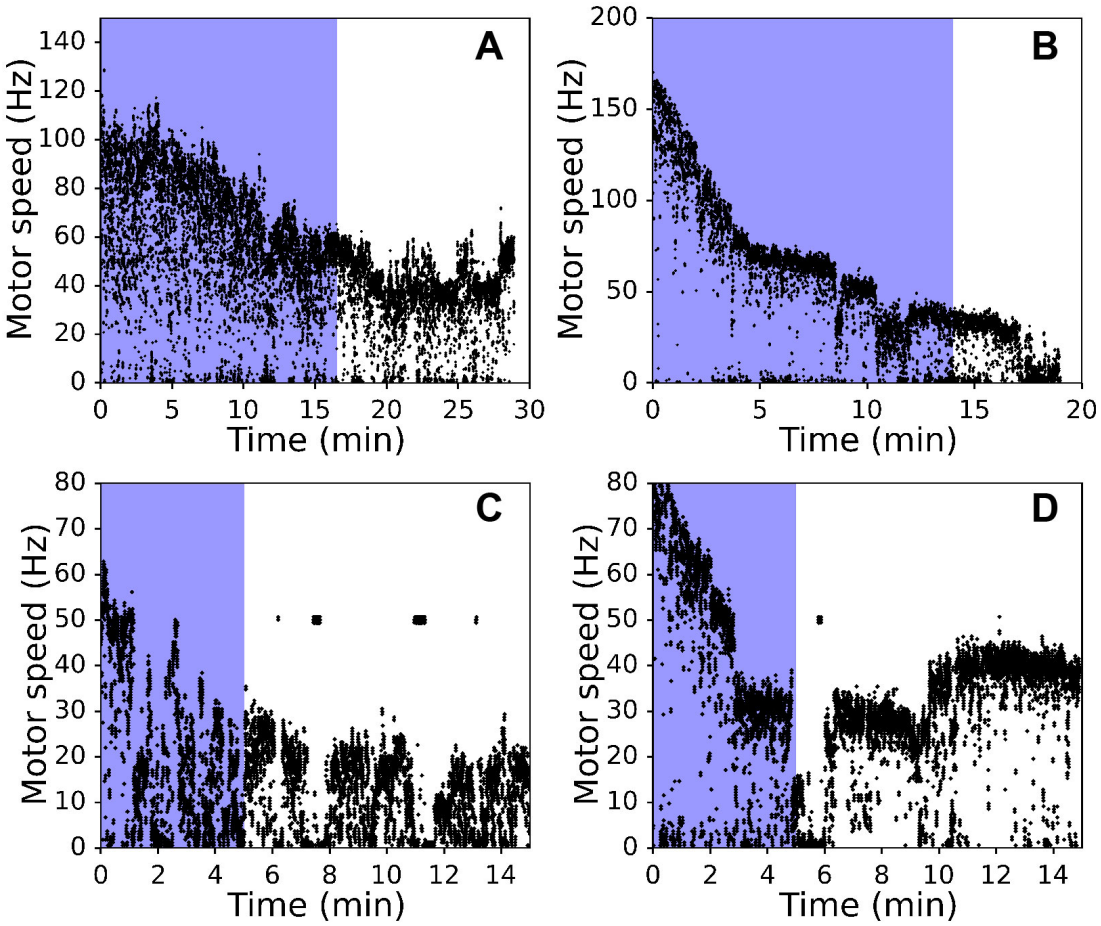

FIGURE 4.7: Raw single motor speed traces during and after light exposure showing that the damage is not reversible on the time scale of the experiment. Shaded blue regions indicate periods of time when the light was on. Cells were kept in MM9 in (**A**) and (**B**) and in PBS in (**C**) and (**D**). Effective light power was 38 mW/cm^2 for (**A**), 350 mW/cm^2 for (**B**) and 591 mW/cm^2 for (**C**) and (**D**).

I also checked that light damage was not enhanced by the presence of the fluorescent protein (pHluorin) in the cytoplasm (Fig. 4.8).

Additional control was performed to ensure that experimental conditions (surface attachment, constant flow, optical trap laser) could not cause the observed speed change. Fig. 4.9 demonstrates that motor speed remained constant for at least 20 min when no stress was applied.

Fig. 4.6D enabled me to determine functional relationship between effective power and α, which increased as a logarithm of the normalised (dimensionless) P_{eff}, i.e. $P_{eff,norm} = P_{eff}/(\text{mW}\cdot\text{cm}^{-2})$. Thus, for the initial exponential fit I obtained:

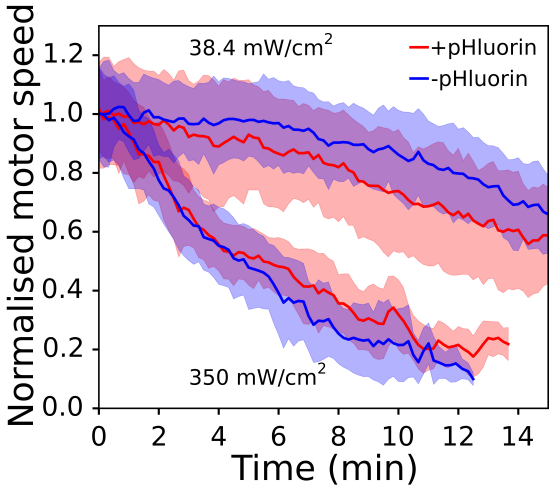

FIGURE 4.8: The presence of pHluorin did not alter the motor speed response to light induced damage. Averaged and normalised motor speed traces (n⩾20 cells) during exposure to light of 395 nm and 475 nm wavelengths with 38.4 and 350 mW/cm^2 effective power. Red traces were obtained with EK07 strain expressing pHluorin protein, and blue traces with the same strain lacking the *pHluorin* gene (EK01). Shaded regions represent standard deviations.

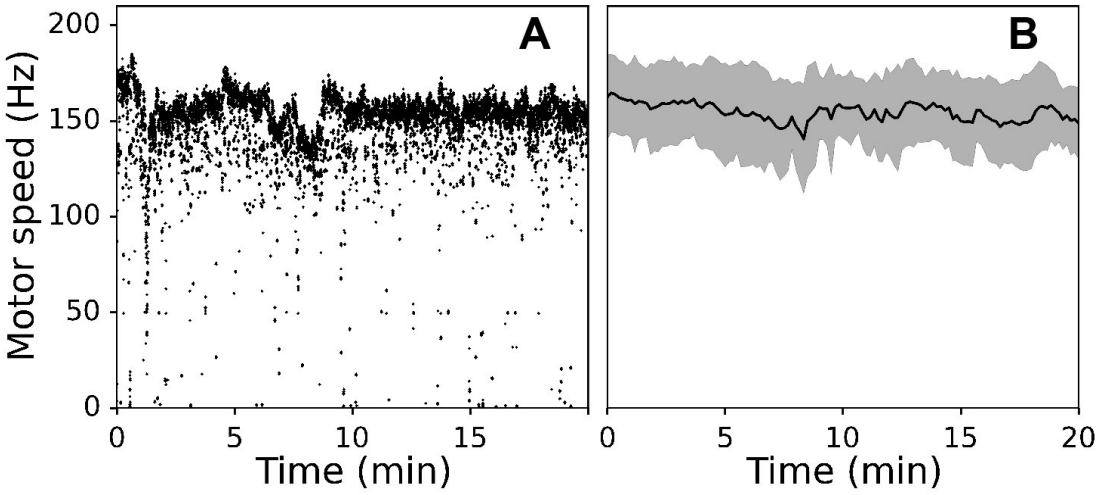

FIGURE 4.9: Experimental conditions solely did not cause PMF decrease. (**A**) Motor speed of a cell in a flow-cell with MM9 continuously exchanged at a 10 μl/min rate, recorded for 20 min. (**B**) Mean BFM speed trace of 17 cells monitored as in (**A**). Standard deviation is shown as shaded grey area. The control experiments were previously done for up to 45 min (Rosko, 2017)

$$\omega = \omega_0 \cdot e^{-(a \ln P_{eff,norm} + b)t} \tag{4.17}$$

where a and b are wavelength specific parameters, a = 0.00064 s^{-1} and b = -0.00181 s^{-1} and equation (4.17) holds for $P_{eff} > P_{eff,0}$.

The minimum power required for the damage to occur is defined as $P_{eff,0} = e^{-\frac{b}{a}}$ mW/cm^2, and for 395 nm and 475 nm this was $\sim$ 16.7 mW/cm^2. Re-writing the equation (4.17) in terms of $P_{eff,0}$ I get:

$$\omega = \omega_0 \left(\frac{P_{eff,0}}{P_{eff}} \right)^{at} \tag{4.18}$$

Finally, applying (4.18) to equation (4.13) I derive R_e functional dependency on the effective power:

$$R_e = \frac{R_{e,0}}{2 \left(\frac{P_{eff}}{P_{eff,0}} \right)^{at} - 1}, \tag{4.19}$$

where a is the fit coefficient in Fig. 4.6D.

4.6 Photodamage is oxygen-dependent

The photodamage experiment was repeated in the oxygen-limited conditions. Cells in MM9 were now attached to the tunnel-slide sealed with Vaseline and exposed to the light of the same power as in the above described experiments. Fig. 4.10A and B show raw and average BFM speed traces at 4 different illumination powers being stable for the duration of the experiment. The initial speeds of the BFM were 1.5 times lower in the sealed slide than in the flow-cell (compare $\sim$150 Hz in Fig. 4.6 and $\sim$100 Hz in Fig. 4.10), suggesting that cells were in the oxygen-depleted environment from the beginning of the recording.

To support the hypothesis that oxygen depletion was possible at the time scale of the experiment, I estimated the time required to consume all the oxygen from the medium. Given the concentration of the dissolved oxygen 0.5 mM (Rasmussen et al., 2003), *E. coli* oxygen consumption rate 0.9-23 mol·kg^{-1}·hours^{-1} (Garcia-Ochoa et al., 2010), bacterial cells density 1.105 g/ml (Martinez-Salas et al., 1981) and estimating cell concentration to be 10^8 cells/ml (50 cells per field of view, $\sim$100 μm x 100 μm, 100 μm channels height), I obtained the time of 9.5 - 240 minutes, for the extreme values of the oxygen consumption rate. It is, thus, reasonable to suggest that cells are in the anaerobic conditions in the course of the experiment.

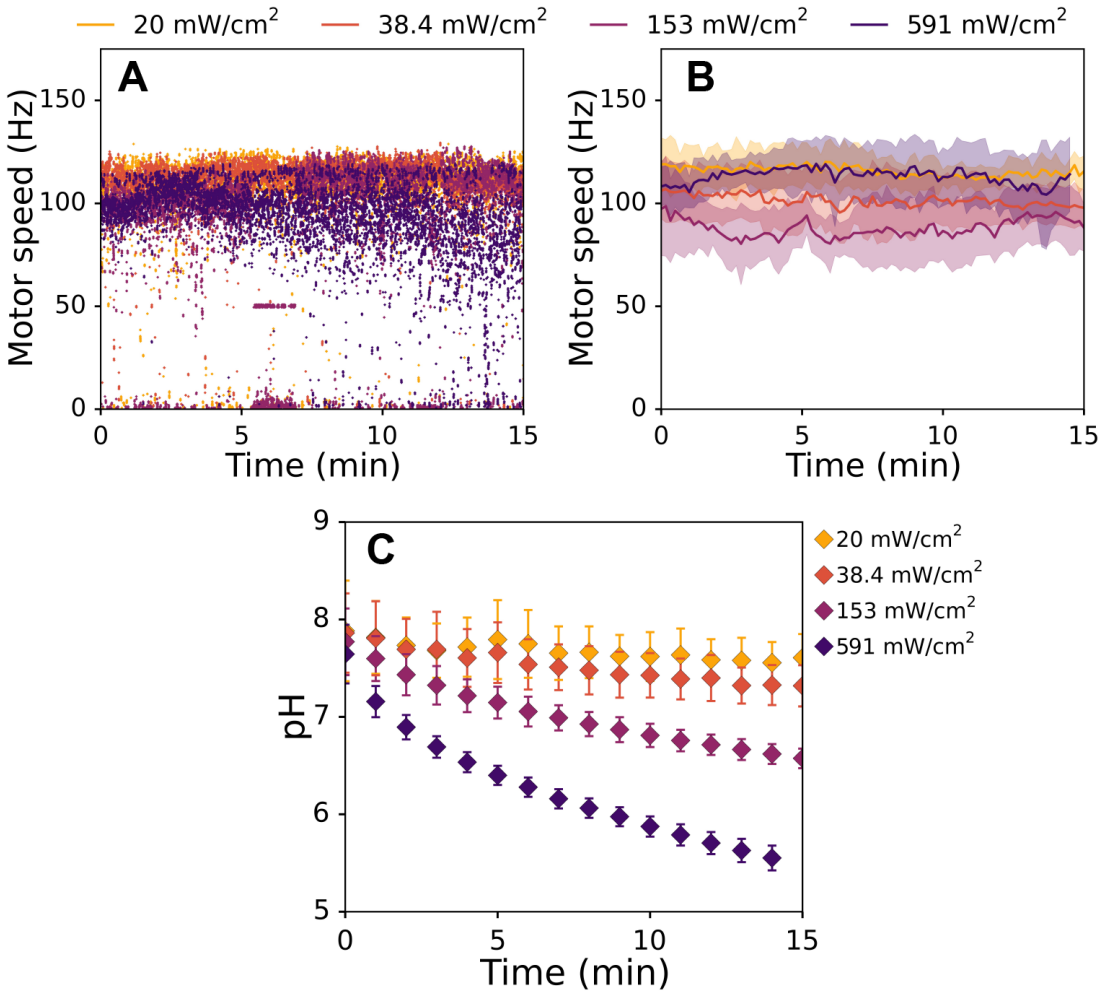

FIGURE 4.10: Motor speed remains constant under the photodamage conditions in the sealed slide in presence of glucose while the cytoplasmic pH decreases. (**A**) Raw speed trace examples at four different effective powers, P_{eff} = 20, 38.4, 153 or 591 mW/cm^2. (**B**) Mean BFM speed at different illumination powers (4 cells are recorded per condition). (**C**) Cytoplasmic pH of the cells exposed to the light with standard deviation. pH decrease scales with the light power.

Fig. 4.10C demonstrates cytoplasmic pH of the cells during the experiment. The internal pH of the cells decreases in a power-dependent manner, which was not the case for the respiring bacteria (Fig. 4.6E).

To additionally test that the decrease in pH reading was not due to the sensor degradation or photobleaching, purified pHluorin was imaged in the sealed tunnel slide in MM9 medium at the highest power used in the previous experiments, 591 mW/cm^2.

Fig. 4.11 demonstrates that pHluorin readings stay stable in the cell-free

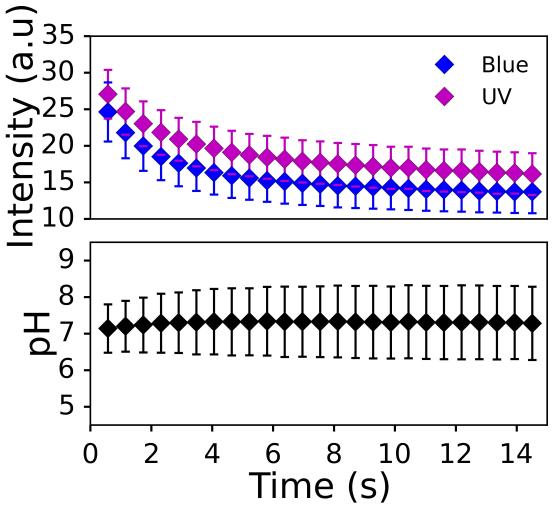

FIGURE 4.11: Purified pHluorin readings were stable in MM9 when exposed to 591 mW/cm^2 light power. Top panel shows absolute emission intensities when pHluorin is excited at 475 nm (Blue) or 395 nm (UV) with standard deviations. Bottom panel shows the pH calculated from the emission intensity ratios with standard deviations.

conditions. There are two possible explanation of the observed pH dynamics: (1) cell cytoplasm gets acidified when cells are exposed to the light in the oxygen-depleted condition with the pH decrease rate being dependent on the light power; (2) the pHluorin readings are influenced by the metabolic activity of the cell exposed to the light in the oxygen-depleted condition. Assumption (2) could be tested by using another pH sensor (cpYFP) in the same experimental conditions. This experiment is yet to be done.

4.7 Oxygen depletion causes the sharp drop in PMF

To investigate an effect of the oxygen depletion with no other stresses applied I measured BFM speed and cytoplasmic pH in the cells in a sealed tunnel-slide in the presence of glucose. It has previously been reported that the swimming speed in the dense bacterial culture drops when the oxygen is fully consumed (Schwarz-Linek et al., 2016). Fig. 4.12A shows a representative speed trace of the cell in a sealed slide. BFM speed remained steady at ∼200 Hz level until it suddenly crashed to ∼100 Hz and did not change after. Note, that ∼100 Hz is the speed of the motors in Fig. 4.10, which supports the assumption that cells

in Fig. 4.10 were depleted in oxygen. For the four spinners observed the speed drop occurred between 25 and 30 minutes of incubation. The measurements of cells internal pH were performed every 5 minutes and are shown in Fig. 4.12B. During the time of the experiment cytoplasmic pH changed from 7.8 to 7.5 units. Oxygen "crash" was observed in the Berg's motility buffer (BMB) from (Schwarz-Linek et al., 2016) (see Section 2.4).

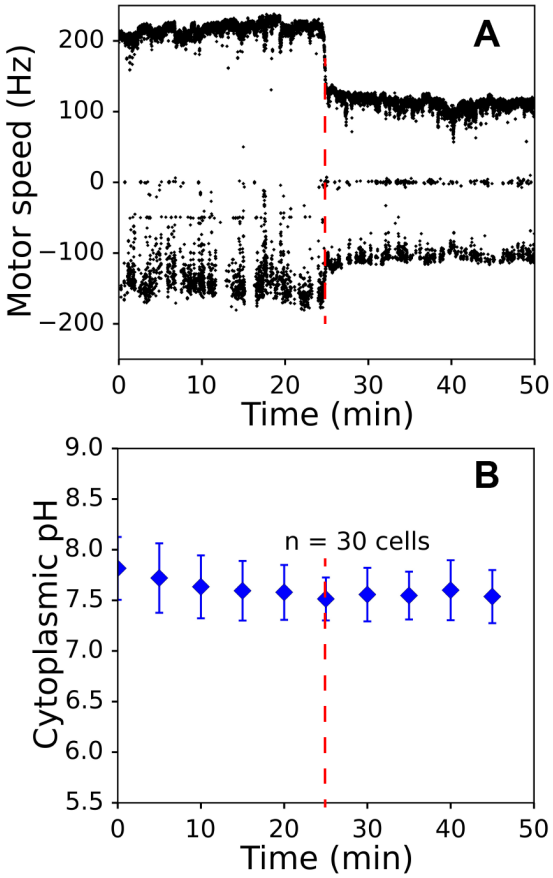

FIGURE 4.12: BFM speed "crashed" when cells ran out of oxygen. (**A**) Raw speed trace example of the cell in a sealed tunnel-slide in the presence of glucose. (**B**) Average internal pH for 30 cells with standard deviation. Red dashed lines mark the point of the oxygen "crash"

As estimated above, in my experimental condition the oxygen depletion occurs between 9 and 240 minutes depending on the actual oxygen consumption rate. This estimate fits with 25-30 minutes intervals for the speed drop observed in the experiment.

I also calculated the glucose depletion rate based on the glucose consumption rate in the oxygenated conditions $\sim 2.2 \cdot 10^{-19}$ mol/min/cell (Schwarz-Linek et al., 2016) and knowing the initial concentration of glucose in the buffer

being 20 mM to be 10^3 min or 16.5 hours. This estimate rules out the possibility of the drop being the result of the glucose limitation and further support the "oxygen crash" assumption.

The switch from the oxidative phosphorylation in the oxygen-reach environment to the substrate level phosphorylation in the absence of oxygen in our circuit analogy can be considered as a change of the battery (V_c and, potentially, R_i) with the membrane staying unmodified.

4.8 *E. coli* exhibit two-step pH response to an acid stress in the oxygen-limited condition

This section results were obtained in collaboration with Dr J Schwarz-Linek and Dr V Martinez

In (Schwarz-Linek et al., 2016) it has been shown that the swimming speed of bacteria in a closed capillary drops twice — upon the depletion of oxygen and the depletion of glucose. Whichever comes first depends on the initial concentrations. For the fully oxygenated medium with 20 mM glucose cells first run out of oxygen, as was calculated in the previous section. Dr J Schwarz-Linek and Dr V Martinez have also characterised the composition of the medium after cells motility ceased and found that it contained the variety of the organic acids (acetate, lactate, formate and succinate), products of *E. coli* anaerobic metabolism (Unden et al., 1997; Leonhartsberger et al., 2002; Vemuri et al., 2006; Meng et al., 2016), and had a pH of 5.48. Thus, at that point cells not only suffered from oxygen starvation but also experienced an acid challenge. The results shown in Fig. 4.10 and 4.12 suggest that *E. coli*'s pH regulation may be compromised in the anaerobic conditions. To establish the connection between the swimming impairment and the loss of the pH homeostasis in the absence of oxygen I looked at the motor speed and the cytoplasmic pH of the cells under the acid stress in the closed capillary.

The BMB was supplemented with 0.9 mM acetate, 3.8 mM lactate, 1.4 mM formate and 0.45 mM succinate. The "mixture" with pH 5.5 was flushed into the tunnel-slide channel 2 min after the beginning of the recording, the channel was sealed immediately after the flush. Recording continued for 30 more minutes.

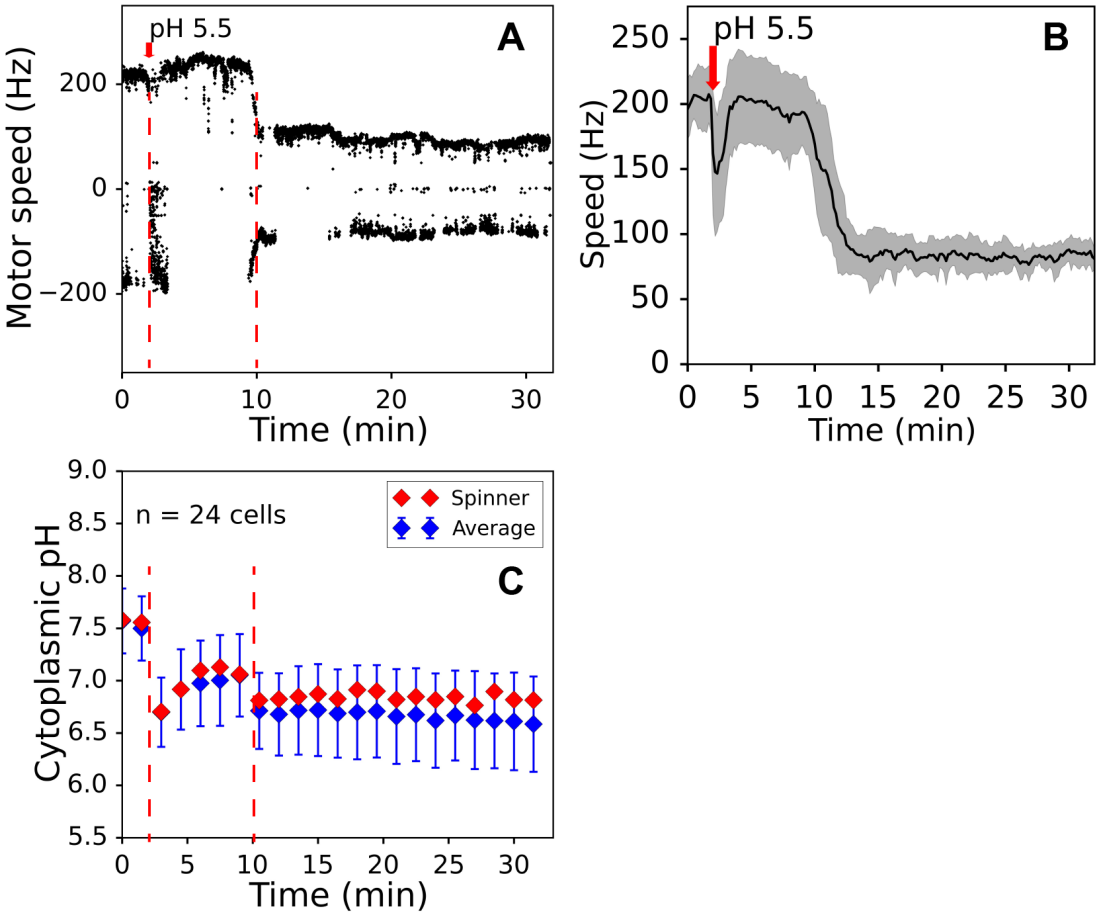

FIGURE 4.13: Oxygen depletion happened faster in an acid stress environment and caused the internal pH drop. (**A**) Raw speed trace example of the cell in a sealed tunnel-slide after the acid stress. Buffer of pH 5.5 was flushed after 2 min of speed recording, slide was sealed immediately after the flush. (**B**) Mean trace of 14 cells with standard deviations given as a shaded region. (**C**) Cytoplasmic pH of the recorded cell (red) and average of 24 cells (blue) with standard deviation. Red dashed lines mark the points of the flush and the oxygen "crash".

Fig. 4.13 shows the example of raw speed trace (A), the average of 14 traces (B) and the internal pH of the cells during the experiment (C). In Fig. 4.13A it is visible that though maximum speed of the motor did not change upon the flush, the frequency of the switches in the rotation direction temporarily increased, which caused a "dip" in the averaged trace in Fig. 4.13B. For freely swimming bacteria this frequent switches interval would mean the increased tumbling followed by the period of no tumbling (Turner et al., 2000; Sowa et al., 2008). After ∼8 min motor speed experienced a drop similar to that shown

in previous section for oxygen depletion. The internal pH underwent two-step change: first, it dropped to ∼6.5 upon the flush and recovered within few minutes, until, due to the "oxygen crash", it dropped once again to pH 6.7-6.8 with no subsequent recovery. Interestingly, the first interval of increased tumbling coincided with the first pH "dip", and the consequent pH decrease was strikingly synchronised with a BFM speed drop. Another thing to note here is how oxygen depletion time decreased from ∼30 min at normal pH to 8 min in the acidic environment, assuming that either or both of two things happened: (1) oxygen consumption rate increased, or (2) the threshold oxygen concentration for switching between respiration and fermentation increased.

4.9 Discussion

Arguably, one of the defining features of life is its ability to avoid thermodynamic equilibrium (death) by achieving a steady state supply of free energy. Chemiosmotic theory proposed by Peter Mitchell (Mitchell, 1961) explained that the production of life's energy currency, the ATP molecule, proceeds via the generation of transmembrane electrochemical potential. The ability to measure and control voltage and current across the cellular membrane with the patch-clamp technique had far reaching consequences for our understanding of cells such as neurones, where the electrical inputs govern signal transmission (Hodgkin et al., 1952). In the cases of bacteria, and their small size, it is not possible to gain the same level of control over the transmembrane currents and electrical potentials (Ruthe et al., 1985; Martinac et al., 1987). Yet, the ability to do so would open a range of currently inaccessible questions that are at the basis of bacterial free energy maintenance, and consequently, bacterial survival.

In this chapter I demonstrated the use of BFM as a fast voltmeter, enabling quantitative, *in vivo* studies of electrochemical properties of the bacterial cell. Alternative methods for measuring V_m in *E. coli* rely on fluorescent readout ((Ehrenberg et al., 1988; Prindle et al., 2015; Kralj et al., 2011) and Chapter 1). However, nernstian dyes (Ehrenberg et al., 1988; Prindle et al., 2015) sometimes fail to penetrate *E. coli*'s membrane (Lo et al., 2007), can be a substrate for the outer membrane efflux system TolC (Mancini et al., 2018) and in external conditions where they do equilibrate across the membrane, they do so on the time scales of minutes (Lo et al., 2007; Winkel et al., 2016). Voltage sensitive

membrane proteins that can be used in *E. coli* require delivery of light of high power (Kralj et al., 2011). BFM, on the other hand, is native to *E. coli* and expressed in a range of conditions (Cremer et al., 2018). Speed measurements via back-focal-plane interferometry or fast cameras do not rely on fluorescent illumination and offer high time resolution (in this work I used 10 ms resolution, but reported previously up to 0.5 ms (Pilizota et al., 2007). Here I worked with cells grown into late exponential phase in LB to maximise the experimental yield. The approach is, however, more widely applicable as BFM is expressed in a range of other conditions (with the exception of late stationary phase cells (Amsler et al., 1993; Cremer et al., 2018)), where the BFM bead-assay yield is expected to somewhat vary with the condition. It is possible that cells grown to early or mid exponential phase, or cells grown to steady state in different growth media, will have different electrochemical properties, which can be measured with the proposed approach in the future.

In the experiments presented in this chapter I mostly worked in the conditions that satisfy ΔpH$\approx$0, and thus V_m was the only contribution to the PMF. However, BFM speed measurements can be extended to conditions where ΔpH contribution to the PMF is not negligible, V_m in this case can be calculated from (4.1). Extending the use of BFM as the voltmeter for long term measurements (into hours and days) is possible. However, on the longer time scales motor can be actively slowed down via YcgR protein (Boehm et al., 2010; Paul et al., 2010), and such long term measurements would likely require YcgR deletion background.

The use of BFM as the cell's voltmeter is based on the proportionality between motor speed and PMF, measured first more than 20 years ago (see Chapter 5 and (Fung et al., 1995; Gabel et al., 2003)). Recent experiments show that BFM also exhibits mechanosensing (Lele et al., 2013; Tipping et al., 2013), where stator unit incorporation depends on the motor torque. These recent findings indicate an intriguing control mechanism, where mechanosensing and the ion flux combined result in the characteristic proportional relationship between the BFM speed and PMF. In the following Chapter I test the applicability and universality of this PMF-motor speed relationship.

Using the electric circuit analogy for the membrane fluxes, and BFM as the cell's "voltmeter" I demonstrated the effect of different stresses on the cell's physiology. As a proof of concept I used a known stress, indole, and confirmed it was an ionophore. For the first unknown stress I tested, butanol,

I showed that its presence decreases membrane resistance, inversely proportional to the butanol concentration. Based on the similarity of the speed traces during butanol and indole treatment, fast dynamics of the response, the reversibility of BFM speed changes and, importantly, an independence of the media I assumed that butanol affected the membrane resistance and not the battery. Thus, I concluded that, in the concentration range tested and on the 15 min time scale, butanol behaved as an ionophore in a manner similar to that of indole or CCCP (Chimerel et al., 2012). With analysis alike I presented, butanol action can be characterised further, e. g. defining the minimum concentration and incubation time required for the effect to become irreversible.

For the light of short wavelengths, I showed that the induced membrane damage can be functionally described, in relation to time and P_{eff}. I demonstrated that the rate of photodamage does not depend on the carbon source, confirming the assumption that the battery was not affected and the membrane did not recover on the time scales of the experiments. Light-induced changes in membrane permeability have been reported in artificial planar lipid bilayer systems and liposomes in the presence of photosensitisers (McRae et al., 1985; Pashkovskaya et al., 2010; Kotova et al., 2011; Wong-Ekkabut et al., 2007). The most likely cause of such changes is ROS induced chain-reaction lipid peroxidation (Girotti, 1985; Girotti, 1990; Halliwell et al., 1993; Heck et al., 2003; Lavi et al., 2010). Presence of peroxidised lipids can change bilayer physical and electrical properties (Dobretsov et al., 1977; Richter, 1987; Birben et al., 2012), e.g. it has been suggested that it induces formation of hydrophobic pre-pores and their later transformation into hydrophilic pores permeable to ions (Kotova et al., 2011; Wong-Ekkabut et al., 2007). Based on the previous work, and presented real time, *in vivo* measurements the following model for the complex nature of the light-induced membrane damage can be proposed. Exposure to light causes the formation of ROS that induce lipid peroxidation, and thus alter the electric properties of the membrane. In particular, its permeability to ions due to the formation of hydrophilic pores. In contrast to the ionophores that carry ions across the membrane without causing membrane damage, the drop in V_m I observed under light proceeds as a result of slower, multi-step formation of lipid pores that require active repair to be mitigated. Therefore, I did not see any fast recovery after illumination ceased (Fig. 4.7), and the chain-reaction nature of the process resulted in the exponential-like decay of membrane potential.

The hypothesis was further supported by repeating the experiment in anaerobic conditions. In the absence of oxygen there was no decrease in motor speed assuming no membrane damage, which was consistent with ROS-mediated damage explanation. However, the loss of cytoplasmic pH in this condition still remains unexplained. To further confirm the formation of ROS during the exposure to the light, strains-reporters for hydrogen peroxide and superoxide were constructed (see Section 2.1) but not yet used.

Living cells have built-in mechanisms of coping with oxidative stress, for instance SoxRS/OxyR regulons containing multiple antioxidant encoding genes, such as *sodA* (manganese superoxide dismutase) or *katG* (hydroperoxidase I) (Storz et al., 1999; Birben et al., 2012). The existence of defence mechanisms explains the occurrence of the minimum power required to cause the damage. Less power, even if it causes ROS formation, will not damage the cells that cope using internal protection enzymes. The value of the minimal damage-causing power I measured can indicate the abundance of internal protective resources available to the cell, as well as define the power range for fluorescence imaging that should be used to ensures no (unaccounted for) damage is inflicted to the cells by the exposure to light.

Based on my measurements it is possible to suggest the use of light for delivery of small molecules, such as antimicrobial peptides or fluorescent dyes, which otherwise fail to penetrate *E. coli's* membrane (Lo et al., 2007).

The experiments conducted in the anaerobic conditions implied the possible importance of the oxygen presence for the intracellular pH regulation, which was investigated further. I first observed a switch from aerobic to anaerobic metabolism, which happened sharply after $\sim$30 min of incubation in the closed capillary, resulting in oxygen consumption rate of $\sim$17 mol/kg/hour at the room temperature (21°C) for cells in late exponential phase. The switch was indicated by sudden drop of the motor speed and a slight decrease of cytoplasmic pH. In terms of the circuit analogy the change of the motor speed could be explained by the change of the V_c battery that caused a drop in V_m.

Later, the acid stress was applied to the cells in the oxygen limited environment. The motor speed did not change upon the acid introduction, though the oxygen starvation occurred 4 times sooner than at normal pH (compare Fig. 4.12 and 4.13). In (Stincone et al., 2011) it has been shown that the acid challenge initiates the transcription of the genes related to the anaerobic metabolism and inhibits those related to the aerobic. The authors concluded that it could

serve as an evidence that the acid exposure induces a shift between aerobic and anaerobic metabolism. The PMF behaviour observed during the acid stress in the oxygen limited conditions goes in line with this conclusion, however, the mechanism, which triggers this shift, remains to be understood. Alternatively, the oxygen consumption rate could be increased in the stressed environment, which leads to a faster oxygen depletion and, thus, to the metabolic shift. Further experiments, including assessment of the oxygen concentration dynamics in the medium, are required to establish the cause-and-effect relationship between the pH and oxygen metabolism.

Strikingly, under such experimental conditions I observed a two-step decrease in the intracellular pH: first immediately upon the acid shock followed by the recovery, and the second due to the oxygen depletion. Recently, the argument occurred in the field of bacteria pH maintenance regarding the cytoplasmic pH response to the acid stress. There are multiple works showing that *E.coli*'s cytoplasmic pH exhibits dip-and-recovery behaviour in response to the low pH challenge (Slonczewski et al., 1982; Wilks et al., 2007; Martinez et al., 2012a). However, recently it has been reported that the internal pH does not recovered within 90 minutes after the pH challenge (Chakraborty et al., 2017). To explain why these recent results contradict with the previous data authors give three possible reasons: (1) pHluorin expression is heterogeneous due to the use of arabinose-induced system; (2) the calibration of the pH sensor is not reliable when sodium benzoate is used; (3) MC4100 strain used in previous studies (Wilks et al., 2007) is different from the MG1655 used by the authors. In this work I used MG1655-based strain constitutively expressing pHluorin and carefully calibrated both *in vivo* and *in vitro* (Chapter 3). Heterogeneities in the level of pHluorin expression (if any) could not affect the pH reading due to the ratiometric nature of the sensor. However, the authors measure internal pH of the cells at 3 points only: before the stress, 5 minutes and 90 minutes after the stress, where previous studies record pH for the first 9-14 minutes after the stress with 30 seconds intervals. Thus, it is possible that authors missed an actual response to the pH challenge (dip-and-recovery in Fig. 4.13C) and observed, in fact, an effect of the oxygen depletion that happens after the stress (second pH drop in Fig. 4.13C).

The methodology presented in this Chapter offers a new way of studying

the effects of the external stresses on the bacterial cell by looking at the immediate change in the PMF, cytoplasmic pH and, consequently, in the membrane voltage. The action of stresses are commonly studied by performing a transcriptional analysis on the population of cells. The single-cell electrophysiology approach presented here is a fast and non-invasive technique that allows us to see the consequences of the stress application to bacteria in terms of the free energy maintenance. The results reported in this Chapter open a new perspective on the processes studied before and raise a series of questions for further investigation. Two projects are currently being launched following the findings of this Chapter. One will be focused on the more detailed characterisation of the damage caused by light and the search for its potential applications. In particular, it will be explored how the damage caused by light of a given power is affected by the wavelength. Once this is known, the optimal wavelength and power will be used to perform the delivery of the antibiotics or/and fluorescently labelled DNA or RNA fragments to the cell's cytoplasm. If successful, the "photoporation" can become a great alternative to the standard delivery techniques such as electroporation, as it should offer more controlled and observable molecules delivery. The second project will be aimed at the understanding of the role of oxygen in the cytoplasmic pH maintenance. Here, the model based on this Chapter results will be developed and further predictions will be made and tested. I believe that the electrophysiology approach will bring even more inspiring data once it has been reinforced by the ATP measurements so that the full energy pool of a single bacterium can be observed simultaneously.

Chapter 5

BFM speed proportionality to the PMF is load dependent

5.1 Introduction

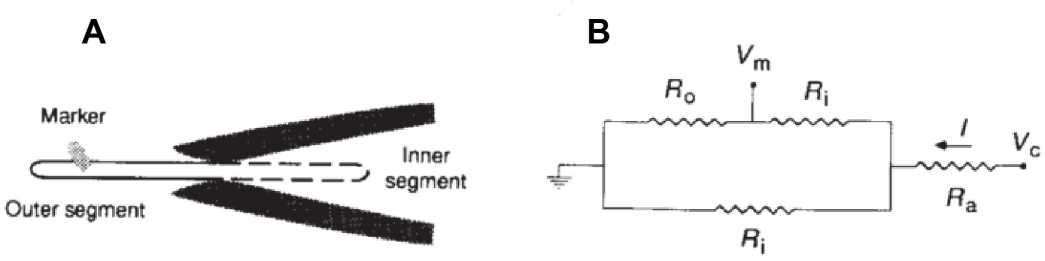

FIGURE 5.1: (**A**) Schematic diagram of a micropipette with partially inserted cell. (**B**) Schematic diagram of the equivalent electrical circuit. R_a is the access resistance of the micropipette, R_i and R_o are the resistances of the inner and outer segments of the cell, respectively, and R_l is the leakage resistance. V_c is the command voltage, and V_m is the voltage across the motor. The total resistance R_T was calculated from V_c and total current I measured by the patch clump. Figure and caption are from (Fung et al., 1995).

The results described in Chapter 4 were obtained under the assumption that BFM motor speed is proportional to the PMF in the entire range of the physiologically possible PMF. This assumption is based on the two papers by Howard Berg *et al*. First, in the 1995 *Nature* paper Fung and Berg showed that the speed of the BFM varies linearly with the PMF by powering the cell with

the external voltage source up to -150 mV (Fung et al., 1995). In this work *E. coli* cells were grown in the presence of cephalexin to become filamentous. One filamentous cell was then held with the micropipette as shown in Fig. 5.1A. Cell's PMF was killed with the ionophore gramicidin S and the command voltage was applied to the cell via the electrode in the micropipette. The equivalent electric circuit used to calculate the potential drop on the motor is shown in Fig. 5.1B.

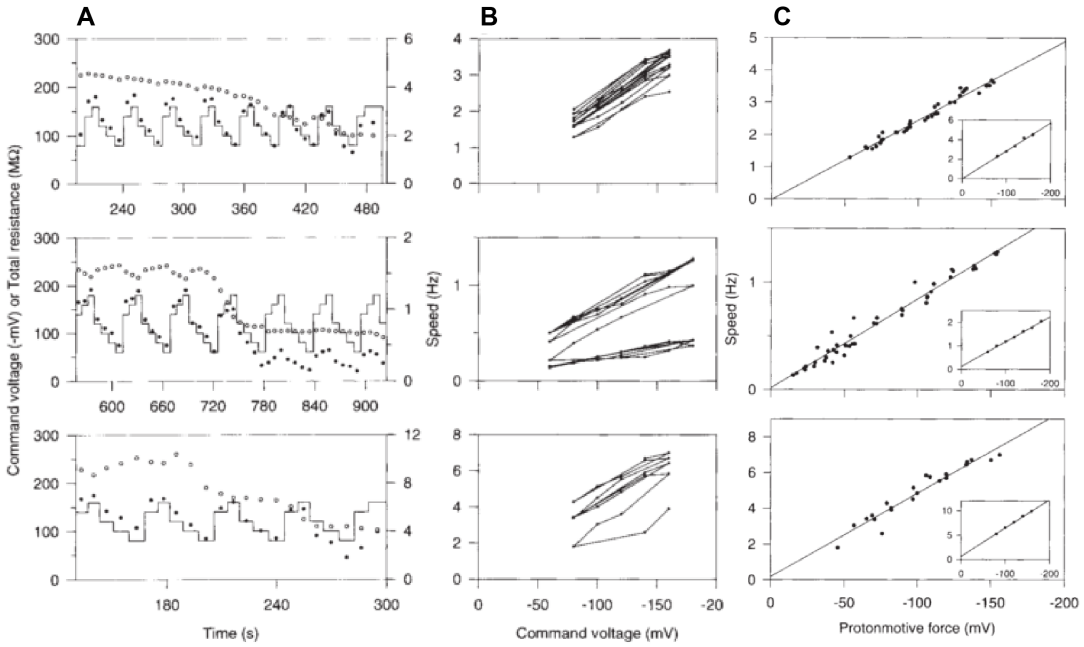

FIGURE 5.2: (**A**) Command voltage (line), motor speed (filled circles) and total resistance (open circles) as a function of time for 3 cells. The time elapsed since the cell was pulled into the micropipette is shown. (**B**) Speed as a function of command voltage for the cells shown in **A**. Successive voltage steps are joined by lines. The initial speeds of the markers were 3.1, 1.4 and 6.8 Hz, respectively; however, the speed of the first marker already was dropping at the time the video was switched on. (**C**) Speed-proton motive force relation for the cells shown in **A** and **B**. Inset, plots validating the assumption that speed is proportional to proton motive force and the resistance of the inner segment of each cell is approximately constant. The parameter B, defined as $B = CV_c(R_i + R_l)/R_l$, is plotted as a function of V_c. Lines are linear regressions. Figure and caption are from (Fung et al., 1995).

The motor speed was measured by recording the rotation of the fluorescent marker attached to the hook of the flagellar motor while an external voltage

was applied. Fig. 5.2A and B shows the motor speed dependence on the applied voltage. In the Fig. 5.2C speed is plotted against the voltage drop on the motor, calculated via known change in the total resistance.

The variation in the slopes of PMF-speed lines for three different cells could be explained by the fact that the fluorescent markers (HCB9 strain cells) were not homogeneous in sizes and the attachment geometry.

Fung and Berg's work was followed by the paper showing that the PMF-speed proportionality is independent on the motor load (Gabel et al., 2003). Speeds of the two motors on the same cell were compared while the cell was treated with either CCCP or sodium azide and shown to be proportional (Fig. 5.3). As the speed of the slower motor had previously been shown to be proportional to the PMF, this experiment provided a further generalisation of the PMF-speed linear relation.

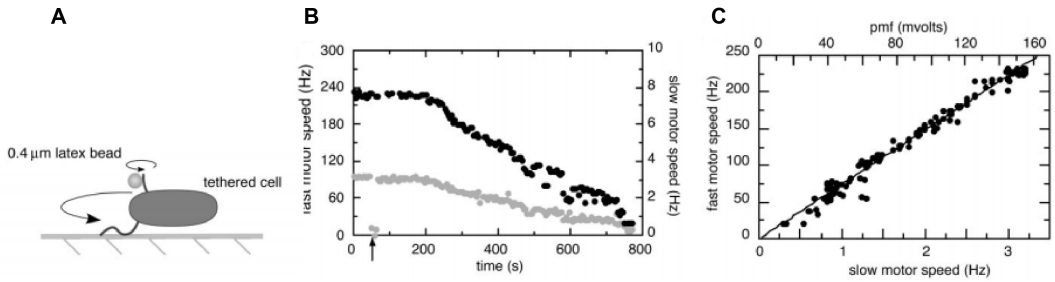

FIGURE 5.3: (**A**) Flagella of a single bacterium were tethered to a glass coverslip and to a small, 0.4-μm-diameter latex bead, respectively. One flagellum rotated slowly because of the large viscous load of the entire bacterium. The other rotated rapidly because of the small viscous load of the latex bead. (**B**) Data for two motors on the same bacterium at 24.0°C are shown. The fully energized bacterium was monitored for ~40 s, and then sodium azide (187 μM) was added (arrow). The cell gradually deenergized. Black points represent the speed of the latex bead (scale on the left), and gray points represent the speed of the cell body (scale on the right). (**C**) The data from **B** are plotted with fast motor speed vs. slow motor speed. Because the slow motor speed (lower x axis) is proportional to pmf, it can be rescaled to give the pmf of the cell (upper x axis). The regression line was constrained to pass through the origin. Figure and caption are from (Gabel et al., 2003).

However, the experiments on the sodium-driven *Vibrio alginolyticus* flagellar motors indicated that BFM speed saturates at the high sodium concentrations and the saturation concentrations are load-dependent (Fig. 5.4 and (Sowa et al., 2003)). The effect was attributed to the limited rate of the sodium association and dissociation kinetics.

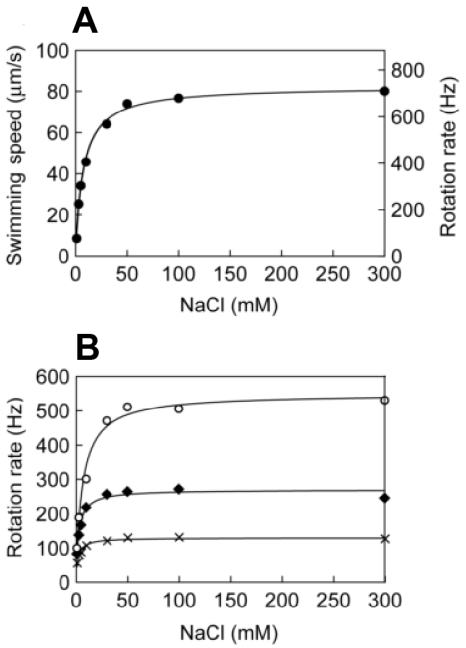

FIGURE 5.4: (**A**) The effect of NaCl concentration on the swimming speed of *V. alginolyticus* NMB136 cells. Each point shows the average swimming speed for 50 cells measured in several independent experiments in the presence of varying NaCl concentrations. The Y-axis on the right represents the flagellar rotation rate calculated from the n:f ratio. (**B**) The relationship between the concentration of NaCl in the external medium and the rotation rate of beads attached to the flagellar filaments. Crosses, filled diamonds and open circles show the average values of rotation rate when beads of 1.08, 0.85 and 0.60 mm diameter were attached to flagellar filaments, respectively. For each data point, at least eight cells were measured. Figure and caption are from (Sowa et al., 2003).

It is expected that proton-driven BFM should also have its limiting rotational speed at high PMF values. In this chapter I revisit the PMF-BFM speed proportionality relationship and find the limits of its applicability.

5.2 BFM speed response to a stress varies with the load

To confirm that the motor speed is proportional to the PMF independently on the load, the experiments described in Chapter 4, originally performed with the 0.5 μm beads, were repeated with the 1 μm beads. Initial speed of the 1 μm bead was $\sim$2.5 times lower than that of a 0.5 μm. Different concentrations of

butanol were applied to the cells and motor speeds were then recorded and analysed the same way as described in Chapter 4. Two examples of the raw traces thus recorded are given in Fig. 5.5 left column. For comparison two examples are given in the same figure right column for 0.5 μm beads. Already from the raw traces it is visible that the same concentration of butanol (e.g. 0.5%, top row in Fig. 5.5) cause a different relative drop in motor speed, which, according to the current perception of the BFM speed-PMF relationship, should not be the case.

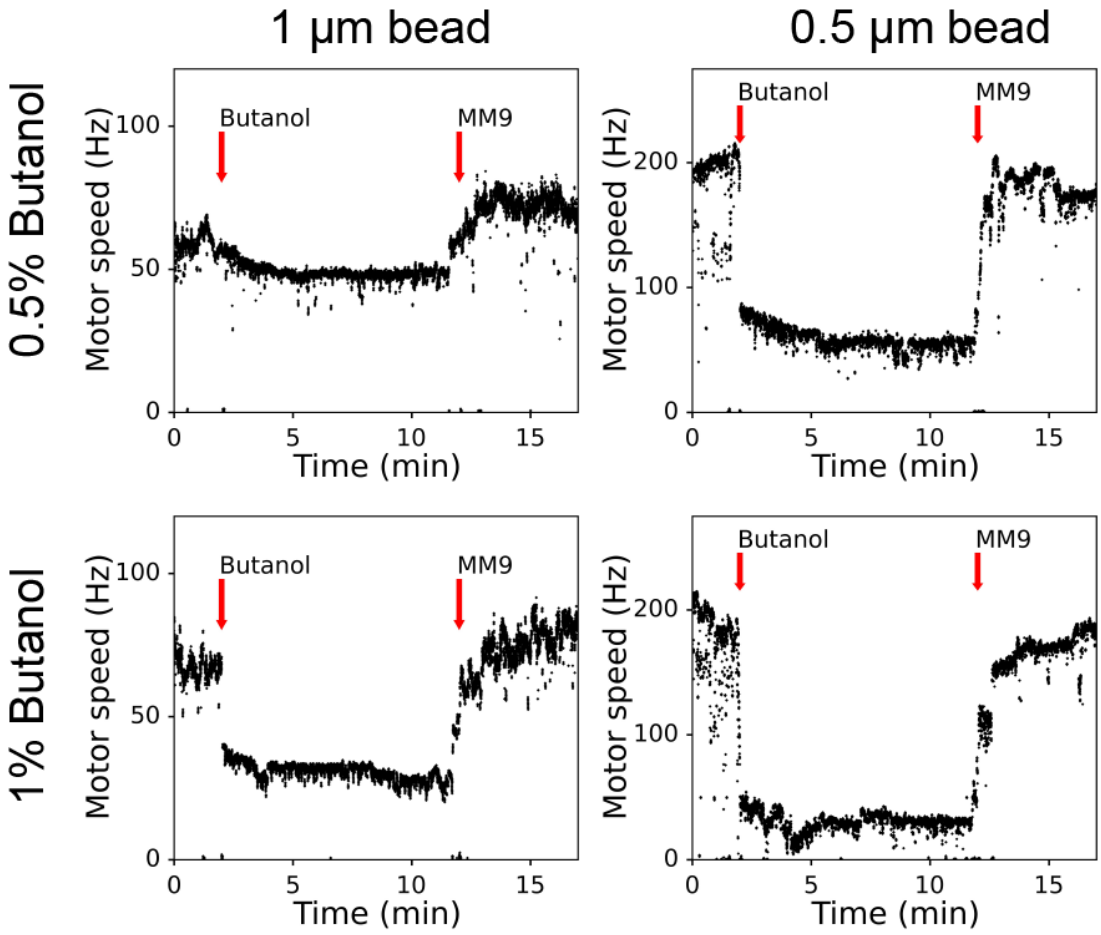

FIGURE 5.5: Raw motor speed traces during treatment with 0.5% (top row) or 1% (bottom row). Speed was recorded for 2 min prior to the stress then butanol was flushed into a tunnel-slide channel and washed out after 10 min (red arrows). Experiment was done with 1 μm (left column) and 0.5 μm (right column) beads.

To rule out the possibility of this effect being attributed to the butanol specifically, the same experiment was repeated with indole. Fig. 5.6 shows a comparison of the normalised motor speeds plotted against indole (A) and

butanol (B) concentrations for the 0.5 μm and 1 μm beads. From the Fig. 5.6 it can clearly be seen that the motor under a higher load (1 μm bead) is less sensitive to low amplitude stresses than the one under a lower load (0.5 μm bead).

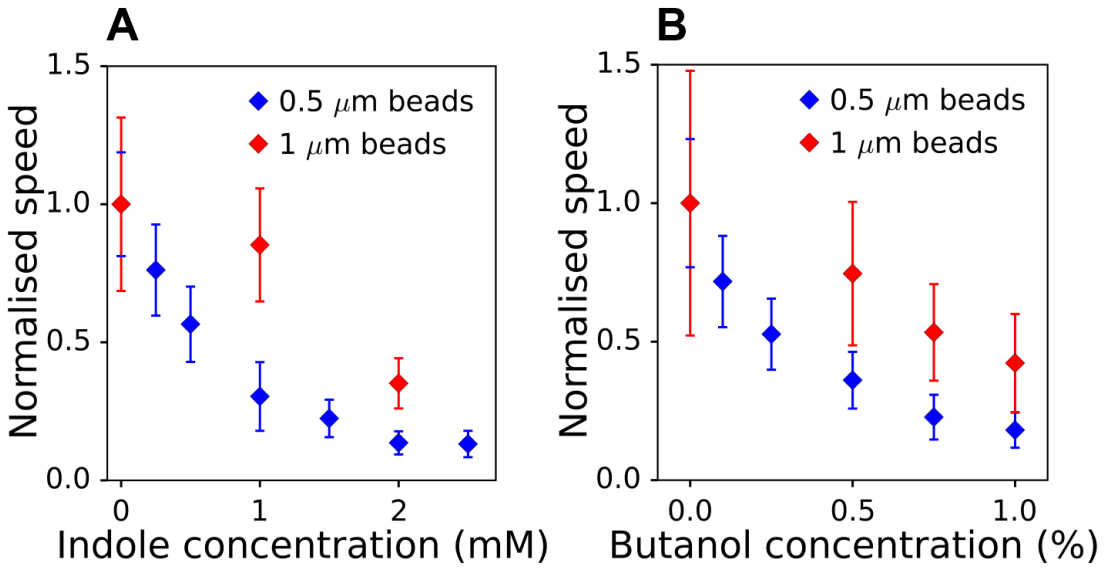

FIGURE 5.6: Shock speeds are normalised by the preshock speed and plotted against indole (**A**) and butanol (**B**) concentration. Blue diamonds show 0.5 μm and red diamonds 1 μm beads speeds. Error bars represent standard deviation.

5.3 BFM speed response to glucose varies with the load

The data discussed above implies that there is a load dependence of the motor speed sensitivity to the PMF changes. One of the possible explanation of this phenomenon could be that the motor speed saturates at the high PMF values and it does so differently at different loads.

To test this hypothesis BFM speed was measured in the range of glucose concentrations at four different loads (Fig. 5.7). Cells attached to the tunnel slide were supplemented with MM9 containing a given amount of glucose. At least 10 motors were measured per condition for 30 seconds interval. Medium was refreshed every 10 minutes to keep both glucose and oxygen concentration at the stable level. The concentration range was chosen based on the findings of (Schwarz-Linek et al., 2016), who showed that the speed of the freely

swimming bacteria changes for the glucose concentrations between 10^{-3} and 10^{-1} mM. The traces were analysed as described in Section 2.5.2. Mean speed values and the standard deviations were calculated from thus found distributions of the motor speed.

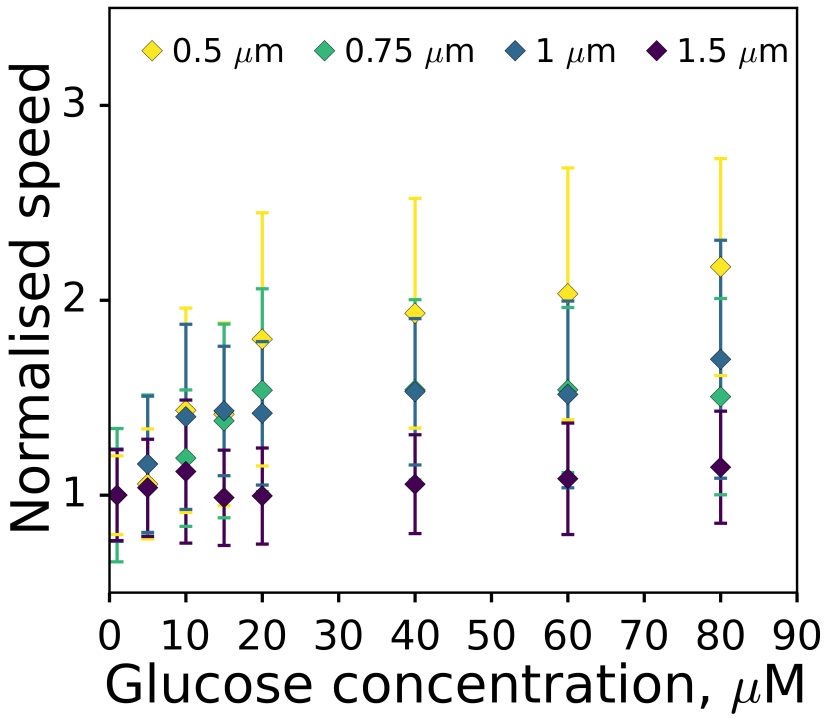

FIGURE 5.7: Motor speeds for four different bead sizes are normalised by the speed at 1 μM glucose and plotted against glucose concentration. Error bars represent standard deviation.

In the Fig. 5.7 the speeds are normalised for the lowest speed at 1 μM glucose for a better comparison. The relative change in the motor speed is smaller at higher loads and becomes more apparent at the lower loads. These data, thus, confirm that the PMF-BFM speed proportionality is not as general concept as it's thought to be.

5.4 Discussion

5.4.1 Load dependent speed saturation

The data presented in this chapter disagree with the thus far accepted results demonstrating that proton-driven BFM motor speed is linearly dependent on

the PMF irrespectively of the external load. The shape of the PMF-speed dependence that could explain the observed effects is shown in Fig. 5.8. In this illustration BFM speed is proportional to the PMF up to a certain value where it flattens out and becomes insensitive to the further PMF increase. The critical value of the PMF where speed reaches its plateau is lower with higher loads.

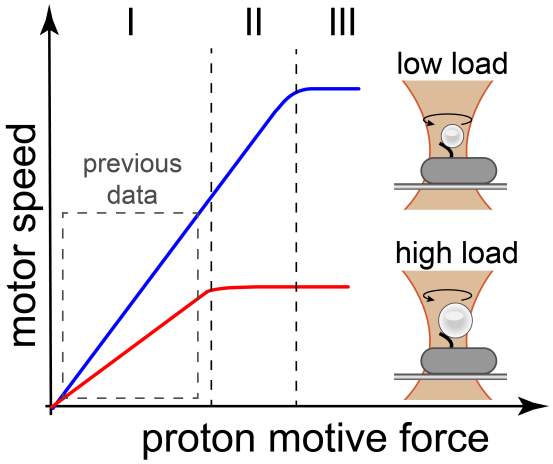

FIGURE 5.8: Cartoon illustrating a hypothesised PMF-speed relation for different loads. Blue and red lines represent PMF-speed curves for low and high load, respectively. The BFM speed is proportional to the PMF at lower values of PMF and saturates at higher values. The saturation happens at the different PMF for the different loads. In the proposed picture, both high and low load speeds are proportional to the PMF in the (I) region, while in the (II) only low load reflects PMF changes and in the (III) both speeds become insensitive to the PMF changes. Previous observations of PMF-motor speed proportionality were presumably focused in (I) region.

If the proposed dependence is correct the difference of the speed changes during butanol and indole treatment in Fig. 5.6 could be explained as follows. Cells in MM9 containing 0.3% glucose (∼25 mM) have a PMF value that lies in region (II) on the illustration in Fig. 5.8 so that BFM speed is proportional to the PMF under the low load (0.5 μm bead) but not under the high load (1 μm bead). However, if we go down the PMF axis the proportionality should restore for the 1 μm bead as well. In Fig. 5.9 I re-plot the data from Fig. 5.6 but normalised by the lower speed (speed at 1 mM indole or at 0.5% butanol). Now we are in the PMF region (I), where both high load and low load motors are sensitive to the PMF changes. The relative speed change is, thus, independent on the load as predicted and the functional dependences obtained in Chapter 4 hold.

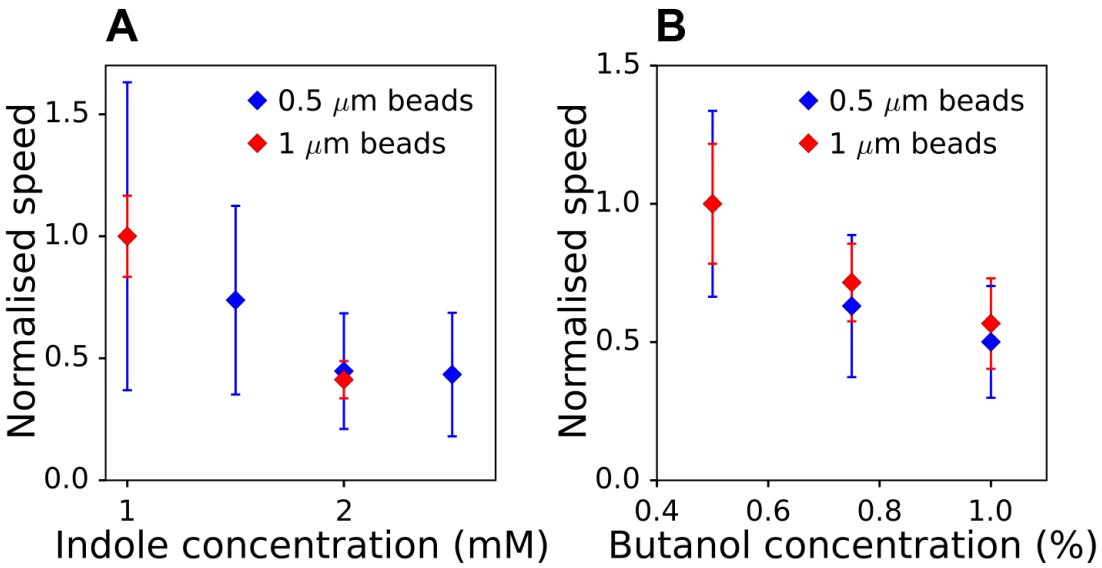

FIGURE 5.9: (**A**) Shock speeds from Fig. 5.6A are normalised by the speed at 1 mM indole and plotted against indole concentration. (**B**) Shock speeds from Fig. 5.6B are normalised by the speed at 0.5% butanol and plotted against butanol concentration. Blue diamonds show 0.5 μm and red diamonds 1 μm beads speeds. Error bars represent standard deviation.

5.4.2 Consistency with previous work

Proposed PMF-speed relationship explains the observed effects and is in agreement with the curves obtained for the sodium-driven motors (Sowa et al., 2003). However, it contradicts results published in (Fung et al., 1995) and (Gabel et al., 2003). The reason could be that in the mentioned works the cell's PMF was not high enough to reach the speed plateau. In (Gabel et al., 2003) speed measurements were performed in a motility medium (10 mM potassium phosphate, 0.1 mM EDTA, 1 mM L-methionine, 0.05% (v/v) lactic acid, pH 7.0) with no glucose, which corresponds to the lowest speed in Fig. 5.7. In (Fung et al., 1995) the voltage was applied directly to the cell and the potential drop on the motor was assumed to be roughly equal to the command voltage varying in the range of 75 to 150 mV. The magnitude of the PMF in *E. coli* has been found to be as high as 160-230 mV (Collins et al., 1976; Tran et al., 1998), which is beyond the range tested by Fung and Berg. Taking the above into account, it is possible to conclude that the results presented in this thesis do not contradict but, in contrary, complement the previous knowledge of the proton-driven motor operation.

5.4.3 Possible mechanism of the speed saturation

The molecular mechanism of the proposed BFM dynamics is still to be understood.

In the Fig. 5.10 I re-plot data from Fig. 5.7 as torque vs. glucose concentration. The torque here is calculated as in (Lo et al., 2007):

$$T = f_r \cdot \omega = (f_b + f_f) \cdot \omega, \tag{5.1}$$

where T is torque, f_r is the rotational frictional drag coefficient and ω is an angular velocity of the BFM. The f_r for the motor is the sum of the drag coefficients of the flagellar filament stub (f_f) and the attached bead (f_b). For the filament stub $f_f \approx 0.5$ pN·nm/Hz (Berg et al., 1993), and f_b is estimated as:

$$f_b = 8\pi\eta {r_b}^3 + 6\pi\eta r_b {r_r}^2, \tag{5.2}$$

where r_b is the radius of the bead, r_r is the radius of the bead's rotation and η is the viscosity of the medium. For MM9 medium viscosity was taken as 0.8 mPa·s (Borić et al., 2012) and the r_r as 200 nm (Lo et al., 2007).

Based on the graph in Fig. 5.10 it is possible to assume that there is the maximum torque (∼2000 pN·nm) that BFM can create, which limits the speed at high loads but not at the lower ones. The factors limiting the BFM torque are yet unclear.

An alternative explanation could be built upon the model of the BFM operation proposed in (Mandadapu et al., 2015; Nirody et al., 2016). According to this model each BFM stator unit performs a two-step power stroke while pumping protons into the cytoplasm (Fig. 5.11). The waiting time (T_w) between strokes depends on the rate of proton arrivals at a binding site given by the Poisson distribution, which, in turns, is defined by the PMF. At the high PMF values the probability of the proton binding increases and the $T_w \to 0$. The load on the motor determines the number of stator units in the single BFM via mechanosensing (Lele et al., 2013; Tipping et al., 2013; Nord et al., 2017). Thus, under the high load the motor will have multiple stator units (up to 11 (Reid et al., 2006)), which at the high PMF values will be operating constantly without the delay due to the proton binding ($T_w \approx 0$). In this regime the steps from different stator units may overlap decreasing the motor efficiency. At the lower loads, having less stator units, BFM will enter the lowered efficiency

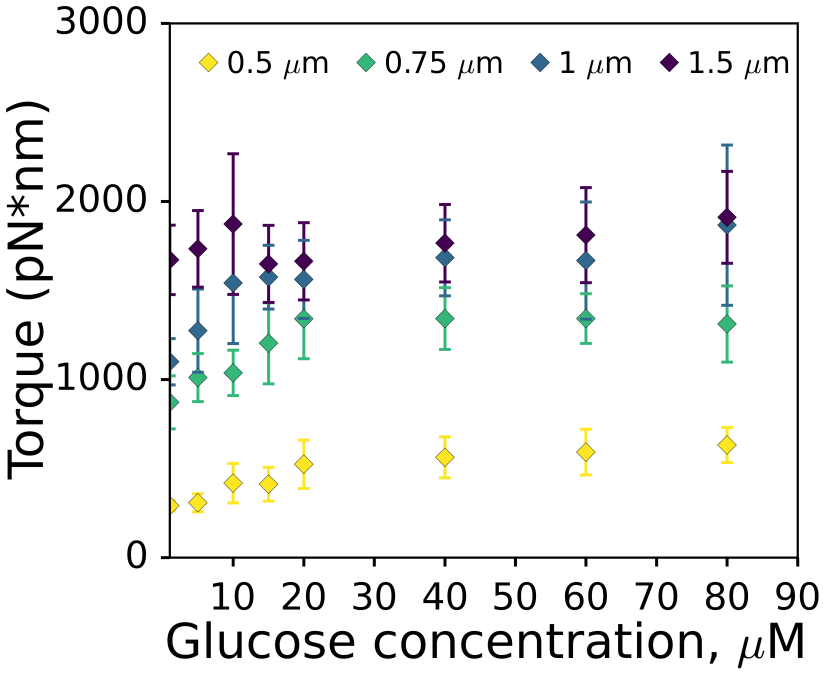

FIGURE 5.10: Motor torque versus the glucose concentration for different loads. Motor speeds from Fig. 5.7 are converted to the torque and plotted against the glucose concentration for 0.5 μm, 0.75 μm, 1 μm and 1.5 μm beads. Error bars represent standard deviation.

regime at the higher PMF values. If that is the case one should see well-defined discrete states of the motor speed saturation at different loads. The fact that in Fig. 5.7 relative speed changes for 0.75 μm and 1 μm are hardly distinguishable may serve as the first evidence in support of the proposed explanation. Further experimental proves are still required, which may include repeating the experiment shown in Fig. 5.7 with the additional bead sizes, and counting a number of fluorescently labelled stator units (Tipping et al., 2013) under the different loads.

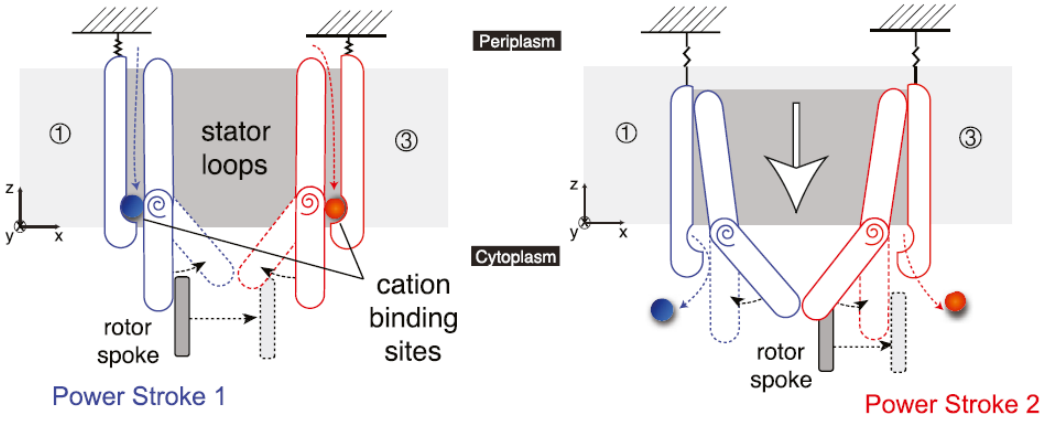

FIGURE 5.11: Overview of our proposed torque generating mechanism. Cation binding induces a strain in the stator, which causes the loops to bend. This results in the first half of the power stroke (here, by Loop 1), and sets up the second loop (here, Loop 3) to perform its half of the power stroke. Subsequently, the cations are released into the cytoplasm. This occurs because our proposed motion also has a vertical component — the loops lower themselves out of the membrane. This release then reverses the strain and causes the loops to re-straighten. This results in the second half of the power stroke. We note that this image depicts a two-dimensional projection of a three-dimensional motion: stator motion is not constrained to the plane of the page. Figure and caption are from (Nirody et al., 2016).

Chapter 6

Conclusions and future work

Living requires energy consumption. Energy transfers are involved in all the biochemical reactions in the cell. The aim of this thesis was to understand the free energy coordination in *E. coli* cells and relate the observed changes to the changes in the cell physiology.

The central concept of bioenergetics is a chemiosmotic theory developed in the middle of the 20th century (Mitchell, 1961). It suggests that the ATP synthesis in respiring cells, both eukaryotes and prokaryotes, is powered by the electrochemical gradient of protons across the inner membrane of the bacteria or mitochondria, making the proton motive force (PMF) one of the crucial components of the cellular energetics. In this work I focused on measuring the PMF and one of the two PMF components — ΔpH. ΔpH is calculated as a difference between the cytoplasmic pH (pH_{in}) and the pH of the external environment (pH_{out}). The latter can be measured with an ion-selective glass electrode and adjusted to the desired value by the addition of either an acidic or alkaline substance to the medium. The ways of measuring pH_{in} have been discussed in Chapter 3.

To simultaneously measure the PMF and the internal pH a variety of *E. coli* strains has been constructed (Section 2.1). Additionally, custom-built microscope design has been extended to accommodate epifluorescence (Section 2.3). The resulting setup allows concurrent back-focal-plane interferometry measurements and the fluorescence imaging.

In this work, I explore the possibility of using genetically encoded ratiometric fluorescent sensors for the intracellular pH measurements in *E. coli*. In Chapter 3 I report that pH can be reliably measured within pH range of 6.0

to 9.0 using pHluorin and newly introduced to bacteria cpYFP proteins. I demonstrate that the pHRed sensor, on the other hand, should not be used for the studies of bacterial physiology (Section 2.1.5). I also discuss the issues related to the pH sensors calibration and the range of conditions it can be used in. The potential future work in this direction includes the search for a pH indicator with a sensitivity in a lower pH range (below 6.0). Few attempts of modifying a pHluorin protein to fulfil this criterion have already been made by an undergraduate student Rachel Mellon under my supervision. Rachel has managed to produce several point mutations in the *pHluorin* gene in order to achieve a lower acid dissociation constant of a protein (pK_a). She obtained a number of functional mutants with spectra different from that of an original pHluorin, but not in a required way. The hope remains that it is possible to use this approach to create a new pHluorin-based sensor for a lower range pH measurements.

To measure the changes in PMF I use bacterial flagellar motor (BFM) as an indicator based on the assumption that its speed varies linearly with PMF within the physiological range of potentials independently of the load (Fung et al., 1995; Gabel et al., 2003). In Chapter 5 I critically assess this statement and find that it does not hold true for higher values of PMF under the higher loads. I confirm that by measuring motor speed changes at various loads in two different cases: while going from high to low PMF using butanol or indole; or while going from low to high PMF by increasing glucose concentration in the medium. In both scenarios I show that at high PMF values and with large loads motor speed saturates and, moreover, the saturation level gets lower with the load increase. I propose two possible explanation for the observed phenomenon: (1) there is a limiting torque BFM is capable to create (approximately 2000 pN·nm, Fig. 5.10); or (2) when under high, the motor has an increased number of stator units, which at high speed (high PMF) regime results in the inefficient cooperation of the stator units. Both hypotheses require further confirmations. In the future, I plan to study PMF-speed relationship under the wider range of the external loads to see whether the saturation exhibits discrete or continuous behaviour. I would also like to perform the stator units number analysis by watching the dynamics of fluorescently labelled MotB (GFP-MotB) protein, that together with MotA forms a $MotA_4MotB_2$ stator unit (Kojima et al., 2004), as in (Tipping et al., 2013). For

the chimeric sodium-driven motor the existence of the limiting speed was explained by the finite rate of the Na^+ ion kinetics, which does not explain the load dependency, unless the number of stator units change, which remains to be confirmed (Sowa et al., 2003). The results however already indicate that the load created by 0.5 μm bead allows the linear PMF-speed relation within the range of physiological PMF values: the maximum created torque is significantly lower than 2000 pN·nm; the speed is sensitive to any non-zero concentrations of the butanol/indole in contrast to the 1 μm bead, where the effect becomes apparent only at concentrations higher than 0.5% or 1 mM respectively. The above analysis allows me to use the flagellar motor speed with the 0.5 μm bead load as a PMF sensor even at high PMF.

Aforesaid made it possible for me to combine well-characterised pH sensors with the bead assay (0.5 μm bead) for simultaneous single-cell internal pH, PMF and V_m measurements. The method was theoretically enhanced by the electric circuit analogy of the bacterial cell to create a new approach we called "quantitative bacterial electrophysiology" by analogy with the neural cell electrophysiology (Chapter 4). The idea of this approach is in understanding of the physiological changes in the bacterial cell in varying environments (e. g. under different stresses) via PMF measurements. First, the PMF change is to be compared in different media to pin down, which part of the cell is affected. Then, using the circuit analogy, a functional description of the affected component change can be found. In Chapter 4 I first confirm the accuracy of the method by applying it to the known membrane stress (indole) and, consequently, evaluate several different unknown stresses: butanol has been shown to act like an ionophore, reversibly and linearly with concentration depolarising the membrane; the light of shorter wavelengths has been demonstrated to damage the membrane immediately upon exposure and irreversibly on the minutes time scale. The damage caused by light has been proven to be oxygen-mediated. Additionally, the oxygen has been found crucial for internal pH maintenance.

I believe that future applications of the quantitative bacterial electrophysiology approach are highly diverse. I would be interested in using it for the classification of the different stresses by their mechanisms of action (e.g. which cellular component is affected, reversibly or irreversibly, functional dependency, etc.) and, potentially, clustering them together in few distinct groups. The

techniques currently used for the this purpose are mostly focused on the proteomics and gene expression analyses. The quantitative bacterial electrophysiology approach will provide a new angle of understanding of stress response in bacteria. Once that's done it would be intriguing to look at the combined action of the stresses from different clusters and find the combination (or combinations) that enhances killing of bacteria the most. That could potentially help in the fight against the antibiotics resistance crisis. Another application could be the studying of the bacterial membrane properties in different conditions, or a membrane proteins electrical properties characterisation (e.g. via change in membrane conductivity upon different levels of expression of a given membrane protein). It could also help with the understanding of the BFM operation itself as discussed previously.

The work described here is a part of the big project, which aim is to discover the fundamental laws of free energy maintenance and coordination. The sensors for single-cell ATP measurements are currently being developed and characterised. These sensors expressed in the reported here strains for the simultaneous PMF and ΔpH measurements will give us an ultimate tool for the free energy dynamics monitoring. The combined ATP and PMF dynamics data obtained in the range of different environments will allow us to construct a mathematical model of the free energy maintenance strategies and significantly expand our understanding of the free energy coordination in a living cell.

Appendix A

Cloning and sequencing

A.1 List of primers

Construct, fragment	**Primers (5′->3′)**	**Template**
pTOF-$fliC^{sticky}$, *fliA* homology	for CCGCTTATGTCTATTGCTGGTCTCG-GTACCCGACCTGCACAATGCTTCGT-GACGCACCA, rev AGCAGGTTCTGTCTCTGCT-GCAGGGTTAATCGTTGTAACCTGAT-TAACTGAGACTGACG	MG1655
pTOF-$fliC^{sticky}$, $fliC^{sticky}$	for CGTCAGTCTCAGTTAATCAGGT-TACAACGATTAACCCTGCAGCAGA-GACAGAACCTGCT, rev CAACGACTTGCAATATAGGATAAC-GAATCATGGCACAAGTCATTAATAC-CAACAGCCTC	pFD313
pTOF-$fliC^{sticky}$, *fliD* homology	for GAGGCTGTTGGTATTAAT-GACTTGTGCCATGATTCGTTATCC-TATATTGCAAGTCGTTG, rev GCTACAGGGCGCGTCCCATTCGC-CACCGGTCGAAAGTTTAGCG-GTAAACGACGATTG	MG1655

pTOF-pHluorin, *att*Tn7 left homology arm	for TATGTCTATTGCTGGTCTCG-GTACCCGACCTGCAATGCCGGT-TATTGTTGTTGCACCGA, rev TCGAAAGACTGGGCCTTTCGTTT-TATCTGCCCGCTTACGCAGGGCATC-CATTTATTACT	MG1655
pTOF-pHluorin, *pHluorin*	for GTAATAAATGGATGCCCTGCG-TAAGCGGGCAGATAAAACGAAAGGC-CCAGTCTTTCGAC, rev AAAACATAACAGGAAGAAAAAT-GCCCCGCATGAGCTGTTGACAAT-TAATCATCGGCTCG	pkk223-3-pHluorin
pTOF-pHluorin, *att*Tn7 right homology arm	for GAGCCGATGAT-TAATTGTCAACAGCTCAT-GCGGGGCATTTTTCTTCCTGTTAT-GTTTTT, rev CAGGGCGCGTCCCATTCGCCAC-CGGTCGACAAACACAGAGAAAG-CACTCATCGATAAGG	MG1655
pTOF-pHluorin+*V.h.* prom, *att*Tn7 left homology arm	for TATGTCTATTGCTGGTCTCG-GTACCCGACCTGCAATGCCGGT-TATTGTTGTTGCACCGA, rev TCGAAAGACTGGGCCTTTCGTTT-TATCTGCCCGCTTACGCAGGGCATC-CATTTATTACT	MG1655
pTOF-pHluorin+*V.h.* prom, *V.harveyi* promoter	for AGTGAAAAGTTCTTCTCCTT-TACTCATATGTATATCTCCTTAAC-TAGGTAATTATCAAGC, rev ATGTTTGATTAAAAA-CATAACAGGAAGAAAAATGCCC-CGCATTTCGACACCTTCGTCCTC	pWR20
pTOF-pHluorin+*V.h.* prom,	for AGTGAAAAGTTCTTCTCCTT-TACTCATATGTATATCTCCTTAAC-TAGGTAATTATCAAGC,	pWR20

pHluorin	rev ATGTTTGATTAAAAA-CATAACAGGAAGAAAAATGCCC-CGCATTTCGACACCTTCGTCCTC	
pTOF-pHluorin+*V.h.* prom, *att*Tn7 right homology arm	for CACTTACCTGAGGACGAAGGT-GTCGAAATGCGGGGCATTTTTCTTCCT-GTTATGTTTTTA, rev CAGGGCGCGTCCCATTCGCCAC-CGGTCGACAAACACAGAGAAAG-CACTCATCGATAAGG	MG1655
pWR-cpYFP/pWR-pHRed, pWR backbone	for TATCCTAGGTGGATGAACTGTA-CAACTGAGGA, rev GCTAGCCATATGTATATCTCCT-TAAC	pWR20
pWR-cpYFP, cpYFP	for TATCATATGTACAACAGCGA-CAACGTCTA, rev TAACCTAGGATCCGGTGGATCG-GATAT	pSHUTTLE CMV_mt-cpYFP
pWR-pHRed, pHRed	for TAACATATGGTTTCCGTTATCG-CAAA, rev TATCCTAGGCCTCTACAAATGTG-GTATGGCTG	pRSET-pHRed
pWR-PkatG, pWR backbone	for GTATCGTAACGGTAACACTGTA-GAGGGGAGCACATTGATGGCTAG-CAAAGGAGAAGAA, rev GTGATCACTGTGTGATTTTCA-CAAAAGCCACACCAAAAAAGTAAT-CAATCGACTACACA	pWR20
pWR-PkatG, P_{katG}	for CCATCTCGACTTTGTGTAGTC-GATTGATTACTTTTTTGGTGTG-GCTTTTGTGAAAATCA, rev GACAACTCCAGTGAA-GAGTTCTTCTCCTTTGCTAGCCAT-CAATGTGCTCCCCTCTACA	MG1655

pWR-PsoxS, pWR backbone	for TGAATTAACGAACTGAACACT-GAAAAGAGGCAGATTTATGGCTAG-CAAAGGAGAAGA, rev CCCGAAGGGCATACGTTAAGT-GCGAAAGAGTGGCAAAAAAGTAAT-CAATCGACTACACA	pWR20
pWR-PsoxS, P_{soxS}	for TCCATCTCGACTTTGTG-TAGTCGATTGATTACTTTTTTGC-CACTCTTTCGCACTTAACG, rev CAACTCCAGTGAAGAGTTCTTCTC-CTTTGCTAGCCATAAATCTGC-CTCTTTTCAGTGT	MG1655
pRSET-pHluorin-his, pRSET back-bone	for TATCCCGGGCTAGATGACTC-GAGGGGC, rev ATTCCTAGGATCTCCTTCTTAAAGT-TAAACAAAA	pRSET-pHRed
pRSET-pHluorin-his, pHluorin-his	for ATCCCCGGGAATTATTTG, rev ATTCCTAGGatgcatcatcac-catcaccacAGTAAAGGAGAA-GAACTTTTCACTG	pkk23-3-pHluorin
pWR-PsoxS/pWR-PkatG, EGFP **control**	TCAGTTGTACAGTTCATCCATG	N/A
pWR-cpYFP/pWR-pHRed, pro-moter **control**	GGGTGCGCTGGTGA	N/A
pBAD-pHRed, promoter **con-trol**	GGCGTCACACTTTGCTATG	N/A
pRSET-pHluorin-his, **control**	CGTTGGCCGATTCATTAATGCAGG	N/A

TABLE A.1: List of primers used for plasmids construction.

A.2 Molecular biology techniques

A.2.1 PCR

For plasmid construction amplification of fragments was done with high fidelity *Phusion* polymerase (NEB, USA) in 50 μl reactions. The PCR mix was prepared on ice as follows:

Component	**Volume for 50 μl reaction**	**Final concentration**
5X Phusion HF Buffer	10 μl	1X
DMSO	1.5 μl	3%
10 mM dNTP	1 μl	200 μM
50 μM primers	2*0.5 μl	0.5 μM
Template DNA	0.5 μl	variable, < 250 ng
Phusion	0.5 μl	1 unit
Nuclease-free water	to 50 μl	-

TABLE A.2: *Phusion* PCR mix for 50 μl reaction.

Samples mixed as described were then transferred to the PCR machine programmed as follows:

Step	**Temperature**	**Time**
Heat lid	110°C	-
Initial denaturation	98°C	30 sec
30 cycles	98°C	10 sec
	T_m	30 sec
	72°C	30 sec per kb
Final extension	72°C	10 min
Store	4°C	-

TABLE A.3: Thermocycling conditions for *Phusion* PCR. T_m was calculated for each set of primers with NEB T_m calculation tool.

For colony PCR I used GoTaq polymerase from Promega (USA). Normally ~16 colonies were picked for the test. PCR mix was prepared in a larger volume and aliquoted 10 μl followed by addition of cells. The typical PCR mix contained the following:

Component	**Volume for 10 μl reaction**	**Final concentration**
5X Green GoTaq Buffer	2 μl	1X
25 mM $MgCl_2$	1 μl	2.5 mM
10 mM dNTP	0.2 μl	200 μM
50 μM primers	2*0.1 μl	0.5 μM
GoTaq	0.1 μl	0.5 units
Nuclease-free water	to 10 μl	-

TABLE A.4: *GoTaq* PCR mix for 10 μl reaction.

Reactions were prepared on ice, cells were added by poking a colony with a pipette tip with subsequent dipping to the PCR mix. The thermocycling conditions were chosen according to the Promega recommendation.

Step	**Temperature**	**Time**
Heat lid	110°C	-
Initial cell disruption and DNA denaturation	95°C	5 min
30 cycles	95°C	30 sec
	T_m	1 min
	72°C	1 min per kb
Final extension	72°C	5 min
Store	4°C	-

TABLE A.5: Thermocycling conditions for *GoTaq* colony PCR. T_m was calculated for each set of primers with NEB T_m calculation tool.

A.2.2 Electrophoresis

50X TAE buffer for gel electrophoresis was prepared as follows: 242 g of Tris Base were dissolved in 600 ml of double distilled water by stirring, then 57.1 ml of Glacial Acetic Acid and 14.61 g f EDTA were added. Volume of the solution was brought up to 1 l and the pH was adjusted to 8.0.

To prepare a mini-gel I added 0.5 mg of agarose (Sigma-Aldrich, USA) to 50 ml of 1X TAE buffer. The agarose was dissolved by heating solution up to boiling in a microwave for $\sim$1.5 min. The melted agarose was then left on the bench until cooled down to $\sim$50°C when 5 μl of 10 000X SafeView Nucleic Acid Stain were added. Agarose solution was then poured into the gel tray with the well comb in place and left to solidify. Ready gel was placed into gel electrophoresis unit filled with 1X TAE. DNA samples pre-mixed with 6X Gel Loading Dye (NEB, USA) were loaded into the gel wells along with the HyperLadder 1 kb or 50 bp (Bioline Reagents Ltd., UK). Gels were run at 140 V for 20-30 minutes and visualised on the GelDoc XR+ system (BioRad, USA).

A.2.3 Purification of DNA fragments

Amplified or digested DNA fragments were purified with Zymo DNA Clean & Concentrator^{TM} or extracted from the agarose gel with Zymoclean^{TM} Gel DNA Recovery Kit according to the manufacturer's instructions.

A.2.4 Digestion

Restriction enzymes (NEB, USA or Promega, USA) were added to 50 μl of the reaction mix according to the manufacturer's instructions. The mix was incubated at 37°C for 1 hour.

A.2.5 Ligation

To ligate fragments of DNA, the T4 DNA ligase (Promega, USA) was used according manufacturer's instructions. Ligation reactions were performed in a total volume of 20 μl per reaction and were incubated at 4°C overnight.

A.2.6 Gibson assembly

Gibson Assembly™ Master Mix (NEB, USA) was used to join multiple fragments together according to NEB protocol. Total reaction volume was 20 μl, incubation was performed in the thermocycler at 50°C for 1 hour.

A.2.7 Transformation

Transformation of chemically competent NEB 5-alpha Competent *E. coli* was done according to the manufacturer's instructions. 5 μl of the ligation or Gibson assembly mixture were added to the cells. Transformed cells were spread onto LB agar plate with the corresponding antibiotic.

A.3 Sequencing results

EK01 strain was sequenced to confirm the presence of *fliC*^{sticky} gene on the chromosome. The sequencing results are shown in Fig. A.1.

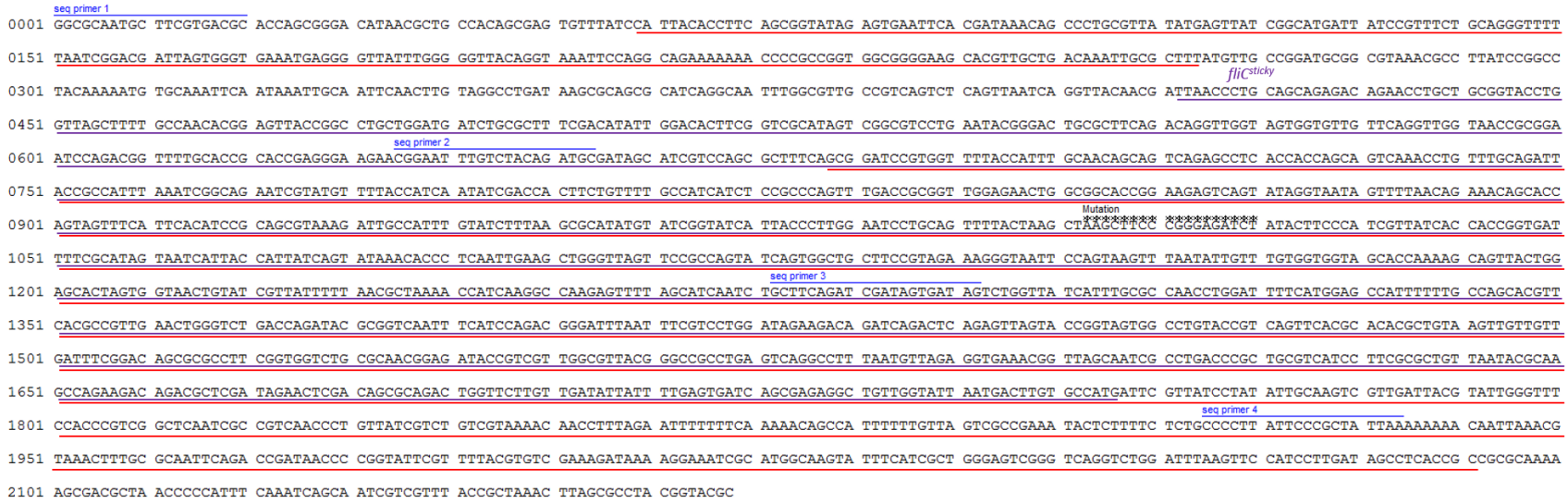

FIGURE A.1: Sequence of the EK01 *fliC*^{sticky} region. Blue lines above the sequence denote sequencing primer locations, purple line underneath — location of the *fliC*^{sticky} gene. Underlined in red regions confirmed with Sanger sequencing. The mutation making flagellar filament "sticky" is marked with the black asterisks.

Appendix B

Mirror mount design

A mount for two polychroic mirrors described in Section 2.3 was designed. The drawing is shown in Fig. B.1.

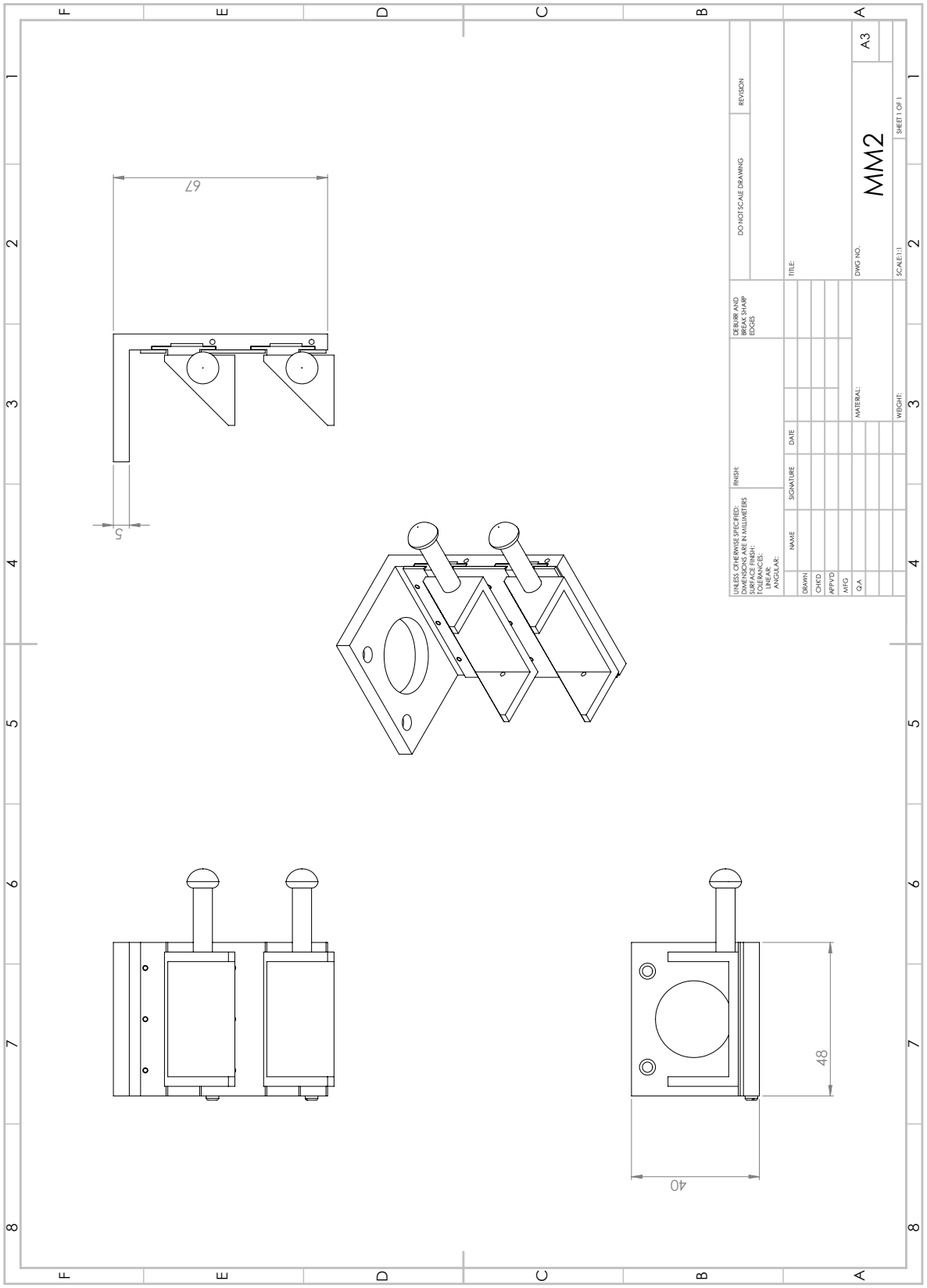

FIGURE B.1: The drawing of the two-level mirror mount. The mount is attached to the stage underneath the objective (see photo in Fig. 2.10B). The inserts can slide in and out of the holder allowing polychroic mirrors to be changed depending on the application.

Bibliography

Ackerman, Joseph J. H. et al. (1996). "The NMR chemical shift pH measurement revisited: analysis of error and modeling of a pH dependent reference." In: *Magnetic resonance in medicine* 36.5, pp. 674–683.

Adler, Julius (1975). "Chemotaxis in bacteria". In: *Journal of supramolecular structure* 4.3, pp. 305–317.

Alberts, Bruce et al. (1994). *Moleculer Biology of the Cell*. 3rd. Vol. 22. 3. Garland Publishing, New York and London, p. 1361. arXiv: arXiv:1011.1669v3.

Amsler, Charles D, Myungsun Cho, and Philip Matsumura (1993). "Multiple factors underlying the maximum motility of Escherichia coli as cultures enter post-exponential growth". In: *Journal of Bacteriology* 175.19, pp. 6238–6244.

Arfman, Nico, V. Worrell, and L. O. Ingram (1992). "Use of the tac promoter and lacI(q) for the controlled expression of Zymomonas mobilis fermentative genes in Escherichia coli and Zymomonas mobilis". In: *Journal of Bacteriology* 174.22, pp. 7370–7378.

Ashkin, Arthur et al. (1986). "Observation of a single-beam gradient force optical trap for dielectric particles". In: *Optics Letters* 11.5, p. 288. arXiv: 1411.1912.

Ashkin, Arthur, J. M. Dziedzic, and T. Yamane (1987). "Optical trapping and manipulation of single cells using infrared laser beams". In: *Nature* 330.6150, pp. 769–771.

Atkinson, Daniel E et al. (1967). "Adenosine Triphosphate Conservation in Metabolic Regulation". In: *The Journal of biological chemistry* 242, pp. 3239–3241.

Bai, Fan et al. (2010). "Conformational spread as a mechanism for cooperativity in the bacterial flagellar switch". In: *Science* 327.5966, pp. 685–689.

Bearne, Stephen L (2014). "Illustrating the effect of pH on enzyme activity using Gibbs energy profiles". In: *Journal of Chemical Education* 91.1, pp. 84–90.

Bennett, Bryson D. et al. (2009). "Absolute metabolite concentrations and implied enzyme active site occupancy in Escherichia coli." In: *Nature Chemical Biology* 5.8, pp. 593–599.

Berg, Howard C. (1971). "How to track bacteria". In: *Review of Scientific Instruments* 42.6, pp. 868–871.

— (2003). "The rotary motor of bacterial flagella". In: *Annual Review of Biochemistry* 72.1, pp. 19–54.

Berg, Howard C. and Douglas A. Brown (1972). "Chemotaxis in Escherichia coli analysed by three-dimensional tracking". In: *Nature* 239.5374, pp. 500–504.

Berg, Howard C. and Robert A. Anderson (1973). "Bacteria swim by rotating their flagellar filaments". In: *Nature* 245.5425, pp. 380–382.

Berg, Howard C. and L. Turner (1993). "Torque generated by the flagellar motor of Escherichia coli". In: *Biophysical Journal* 65.5, pp. 2201–16.

Berg, Jeremy M., John L. Tymoczko, and Lubert Stryer (2002). *Biochemistry*. 5th. New York: W. H. Freeman and Company, p. 974.

Berg, Jim, Yin Pun Hung, and Gary Yellen (2009). "A genetically encoded fluorescent reporter of ATP:ADP ratio". In: *Nature Methods* 6.2, pp. 161–166.

Birben, Esra et al. (2012). "Oxidative Stress and Antioxidant Defense". In: *World Allergy Organization Journal* 5.1, pp. 9–19. arXiv: NIHMS150003.

Boehm, Alex et al. (2010). "Second Messenger-Mediated Adjustment of Bacterial Swimming Velocity". In: *Cell* 141.1, pp. 107–116.

Boer, Herman A. de, L. J. Comstock, and M. Vasser (1983). "The tac promoter: a functional hybrid derived from the trp and lac promoters." In: *Proceedings of the National Academy of Sciences of the United States of America* 80.1, pp. 21–25.

Bolivar, Francisco et al. (1977). "Construction and characterization of new cloning vehicle. II. A multipurpose cloning system". In: *Gene* 2.2, pp. 95–113.

Bolton, Eugene, Patrick Glynn, and Fergal O'Gara (1984). "Site specific transposition of Tn7 into a Rhizobium meliloti megaplasmid". In: *MGG - Molecular & General Genetics* 193.1, pp. 153–157.

Borić, Maja, Tjaša Danevčič, and David Stopar (2012). "Viscosity dictates metabolic activity of Vibrio ruber". In: *Frontiers in Microbiology* 3, p. 255.

Breeuwer, Pieter and Tjakko Abee (2004). "Assessment of the membrane potential, intracellular pH and respiration of bacteria employing fluorescence

techniques". In: *Molecular Microbial Ecology Manual*. 2nd. 8.01. Kluwer Academic Publishers, pp. 1563–80.

Brosius, Jurgen and Adriana Holy (1984). "Regulation of ribosomal RNA promoters with a synthetic lac operator." In: *Proceedings of the National Academy of Sciences of the United States of America* 81.22, pp. 6929–6933.

Buda, Renata et al. (2016). "Dynamics of Escherichia coli 's passive response to a sudden decrease in external osmolarity". In: *Proceedings of the National Academy of Sciences of the United States of America* 113.40, E5838–E5846.

Cabiscol, Elisa, Jordi Tamarit, and Joaquim Ros (2000). "Oxidative stress in bacteria and protein damage by reactive oxygen species". In: *International Microbiology* 3.1, pp. 3–8.

Caldwell, Peter C. (1956). "Intracellular pH". In: *International Review of Cytology* 5.C, pp. 229–277.

Cavari, Ben Z. and Y. Avi-Dor (1967). "Effect of carbonyl cyanide m-chlorophenylhydrazone on respiration and respiration-dependent phosphorylation in Escherichia coli." In: *The Biochemical Journal* 103.2, pp. 601–608.

Chakraborty, Smarajit et al. (2017). "Non-canonical activation of OmpR drives acid and osmotic stress responses in single bacterial cells". In: *Nature Communications* 8.1, p. 1587.

Chen, Xiaobing and Howard C Berg (2000). "Torque-speed relationship of the flagellar rotary motor of Escherichia coli". In: *Biophysical Journal* 78.2, pp. 1036–1041.

Chimerel, Catalin et al. (2012). "Indole prevents Escherichia coli cell division by modulating membrane potential". In: *Biochimica et Biophysica Acta - Biomembranes* 1818.7, pp. 1590–1594.

Choi, Jeongjoon and Eduardo A. Groisman (2016). "Acidic pH sensing in the bacterial cytoplasm is required for Salmonella virulence". In: *Molecular Microbiology* 101.6, pp. 1024–1038.

Cleri, Fabrizio (2016). *The Physics of Living Systems*. Springer Nature, p. 611.

Cole, Heather A., J. W.T. Wimpenny, and D. E. Hughes (1967). "The ATP pool in Escherichia coli. I. Measurement of the pool using a modified luciferase assay". In: *Biochimica et Biophysica Acta - Bioenergetics* 143.3, pp. 445–453.

Collins, Stephen H. and W. Allan Hamilton (1976). "Magnitude of the protonmotive force in respiring Staphylococcus aureus and Escherichia coli". In: *Journal of Bacteriology* 126.3, pp. 1224–1231.

Cremer, Jonas et al. (2018). "On the growth and migration of chemotactic bacterial populations in nutrient-replete environments". In: *In preparation*.

Cubitt, Andrew B. et al. (1995). "Understanding, improving and using green fluorescent proteins". In: *Trends in Biochemical Sciences* 20.11, pp. 448–455.

Datsenko, Kirill A and Barry L Wanner (2000). "One-step inactivation of chromosomal genes in Escherichia coli K-12 using PCR products." In: *Proceedings of the National Academy of Sciences of the United States of America* 97.12, pp. 6640–5. arXiv: 1111.6189v1.

Denk, Winfried and Watt W. Webb (1990). "Optical measurement of picometer displacements of transparent microscopic objects." In: *Applied optics* 29.16, pp. 2382–2391.

Dobretsov, Gennady E. et al. (1977). "The increase of phospholipid bilayer rigidity after lipid peroxidation." In: *FEBS Letters* 84.1, pp. 125–8.

Duhem, Pierre (1886). *Le potentiel thermodynamique et ses applications à la mécanique chimique et à l'étude des phénomènes électriques*. Paris: A. Hermann, p. 264.

Ehrenberg, Benjamin et al. (1988). "Membrane potential can be determined in individual cells from the nernstian distribution of cationic dyes". In: *Biophysical Journal* 53.5, pp. 785–794.

Farré, Arnau, Ferran Marsà, and Mario Montes-Usategui (2012). "Optimized back-focal-plane interferometry directly measures forces of optically trapped particles". In: *Optics Express* 20.11, p. 12270.

Fiske, Cyrus H. (1934). "The nature of the depressor substance of the blood." In: *Proceedings of the National Academy of Sciences of the United States of America* 20.1, pp. 25–7.

Fletcher, Eugene et al. (2016). "Characterization of the effects of n-butanol on the cell envelope of E. coli". In: *Applied Microbiology and Biotechnology* 100.22, pp. 9653–9659.

Ford, Sharon R. et al. (1996). "Use of firefly luciferase for ATP measurement: Other nucleotides enhance turnover". In: *Journal of Bioluminescence and Chemiluminescence* 11.3, pp. 149–167.

Francis, Noreen R. et al. (1994). "Isolation, characterization and structure of bacterial flagellar motors containing the switch complex". In: *Journal of Molecular Biology* 235.4, pp. 1261–1270.

Fricke, Hugo (1923). "The electric capacity of cell suspension". In: *Physical Review* 21, pp. 708–709.

Fricke, Hugo et al. (1956). "A dielectric study of the low-conductance surface membrane in E. coli". In: *Nature* 177.4499, pp. 134–135.

Fung, David C. and Howard C. Berg (1995). "Powering the flagellar motor of Escherichia coli with an external voltage source". In: *Nature* 375.6534, pp. 809–812.

Gabel, Christopher V and Howard C Berg (2003). "The speed of the flagellar rotary motor of Escherichia coli varies linearly with protonmotive force." In: *Proceedings of the National Academy of Sciences of the United States of America* 100.15, pp. 8748–8751.

Galvani, Luigi (1791). "De viribus electricitatis in motu musculari commentarius". In: *De Bononiensi Scientiarum et Artium Instituto atque Academia Commentarii, tomus septimus.* Pp. 363–418.

Garcia-Ochoa, Felix et al. (2010). "Oxygen uptake rate in microbial processes: An overview". In: *Biochemical Engineering Journal* 49.3, pp. 289–307.

Gibson, Daniel G et al. (2009). "Enzymatic assembly of DNA molecules up to several hundred kilobases". In: *Nature Methods* 6.5, pp. 343–345.

Girotti, Albert W. (1985). "Mechanisms of lipid peroxidation". In: *Journal of Free Radicals in Biology and Medicine* 1.2, pp. 87–95.

— (1990). "Photodynamic lipid peroxidation in biological systems." In: *Photochemistry and photobiology* 51.4, pp. 497–509.

Gittes, Frederick and Christoph F Schmidt (1998). "Interference model for back-focal-plane displacement detection in optical tweezers". In: *Optics Letters* 23.1, p. 7.

Gorden, Jed and P. L. Small (1993). "Acid resistance in enteric bacteria." In: *Infection and immunity* 61.1, pp. 364–7.

Green, Robert Montraville (1953). "A Translation of Luigi Galvani's De viribus electricitatis in motu musculari commentarius. Commentary on the Effect of Electricity on Muscular Motion". In: *Journal of the American Medical Association* 153.10, p. 989.

Guyer, M S et al. (1981). "Identification of a sex-factor-affinity site in E. coli as gamma delta." In: *Cold Spring Harbor Symposia on Quantitative Biology* 45 Pt 1, pp. 135–140.

Guzman, Luz-Maria et al. (1995). "Tight regulation, modulation, and high-level expression by vectors containing the arabinose P(BAD) promoter". In: *Journal of Bacteriology* 177.14, pp. 4121–4130.

Halliwell, Barry et al. (1993). "Lipid peroxidation: Its mechanism, measurement, and significance". In: *American Journal of Clinical Nutrition* 57.5 SUPPL. 715S–725S.

Han, Junyan and Kevin Burgess (2010). "Fluorescent indicators for intracellular pH". In: *Chemical Reviews* 110.5, pp. 2709–2728.

He, Tong-Chuan et al. (1998). "A simplified system for generating recombinant adenoviruses". In: *Proceedings of the National Academy of Sciences of the United States of America* 95.5, pp. 2509–2514.

Heck, Diane E et al. (2003). "UVB light stimulates production of reactive oxygen species: Unexpected role for catalase". In: *Journal of Biological Chemistry* 278.25, pp. 22432–22436.

Hodgkin, Alan L. and Andrew F. Huxley (1939). "Action potentials recorded from inside a nerve fibre". In: *Nature* 144.3651, pp. 710–711.

Hodgkin, Alan L., Andrew F. Huxley, and Bernard Katz (1952). "Measurement of current-voltage relations in the membrane of the giant axon of Loligo". In: *The Journal of Physiology* 116.4, pp. 424–448.

Iino, Ryota et al. (2005). "Real-time monitoring of conformational dynamics of the ϵ subunit in F1-ATPase". In: *Journal of Biological Chemistry* 280.48, pp. 40130–40134.

Imamura, Hiromi et al. (2009). "Visualization of ATP levels inside single living cells with fluorescence resonance energy transfer-based genetically encoded indicators". In: *Proceedings of the National Academy of Sciences of the United States of America* 106.37, 15651 LP –15656.

Jager, T. L. de, A. E. Cockrell, and S. S. Du Plessis (2017). "Ultraviolet Light Induced Generation of Reactive Oxygen Species". In: *Ultraviolet Light in Human Health, Diseases and Environment. Advances in Experimental Medicine and Biology*. Ed. by S. Ahmad. Springer, Cham, pp. 15–23.

Kashket, Eva R (1985). "The proton motive force in bacteria: a critical assessment of methods". In: *Annual Review of Microbiology* 39, pp. 219–42.

Keis, Stefanie et al. (2006). "Inhibition of ATP hydrolysis by thermoalkaliphilic F1F 0-ATP synthase is controlled by the C terminus of the ϵ subunit". In: *Journal of Bacteriology* 188.11, pp. 3796–3804.

Kerb, Stanley E. and Lateefeh Daoud (1935). "A study of the organic acid-soluble phosphorus of the erythrocytes of various vertebrates". In: *Journal of Biological Chemistry* 109, pp. 301–315.

Kneen, Malea et al. (1998). "Green fluorescent protein as a noninvasive intracellular pH indicator". In: *Biophysical Journal* 74.3, pp. 1591–1599.

Kojima, Seiji and David F. Blair (2004). "Solubilization and Purification of the MotA/MotB Complex of Escherichia coli". In: *Biochemistry* 43.1, pp. 26–34.

Kotova, Elena A et al. (2011). "Selective permeabilization of lipid membranes by photodynamic action via formation of hydrophobic defects or prepores". In: *Biochimica et Biophysica Acta - Biomembranes* 1808.9, pp. 2252–2257.

Kralj, Joel M. et al. (2011). "Electrical spiking in Escherichia coli probed with a fluorescent voltage-indicating protein". In: *Science* 333.6040, pp. 345–348. arXiv: NIHMS150003.

Kurkdjian, Armen and Jean Guern (1989). "intracellular pH: measurement and importance in cell activity". In: *Annual review of plant physiology and plant molecular biology* 40, pp. 271–303.

Kuwajima, Goro (1988). "Construction of a minimum-size functional flagellin of Escherichia coli". In: *Journal of Bacteriology* 170.7, pp. 3305–3309.

Lavi, Ronit et al. (2010). "Detailed analysis of reactive oxygen species induced by visible light in various cell types". In: *Lasers in Surgery and Medicine* 42.6, pp. 473–480.

Lazar, Sara W et al. (1998). "Role of the Escherichia coli SurA protein in stationary-phase survival". In: *Journal of Bacteriology* 180.21, pp. 5704–5711.

Lele, Pushkar P, Basarab G Hosu, and Howard C Berg (2013). "Dynamics of mechanosensing in the bacterial flagellar motor". In: *Proceedings of the National Academy of Sciences of the United States of America* 110.29, pp. 11839–11844.

Leonhartsberger, Susanne, Ingrid Korsa, and August Böck (2002). "The molecular biology of formate metabolism in enterobacteria." In: *Journal of molecular microbiology and biotechnology* 4.3, pp. 269–76.

Lewis, Gilbert Newton (1907). "Outlines of a new system of thermodynamic chemistry". In: *Proceedings of the American Academy of Arts and Sciences* 43, pp. 259–293.

Li, Mei, Xin Huang, and Stephen Mann (2014). "Spontaneous growth and division in self-reproducing inorganic colloidosomes". In: *Small* 10.16, pp. 3291–3298.

Li, Yulong and Richard W Tsien (2012). "PHTomato, a red, genetically encoded indicator that enables multiplex interrogation of synaptic activity". In: *Nature Neuroscience* 15.7, pp. 1047–1053. arXiv: NIHMS150003.

Lin, Jyhshiun et al. (1995). "Comparative analysis of extreme acid survival in Salmonella typhimurium, Shigella flexneri, and Escherichia coli". In: *Journal of Bacteriology* 177.14, pp. 4097–4104.

Ling, G. and R. W. Gerard (1949). "The membrane potential and metabolism of muscle fibers." In: *Journal of Cellular Physiology* 34.3, pp. 413–38.

Link, Andrew J and Dereth Phillips (1997). "Methods for generating precise deletions and insertions in the genome of wild-type Escherichia coli : application to open reading frame characterization". In: *Journal of Bacteriology* 179.20, pp. 6228–6237.

Liu, Bin et al. (2014). "Helical motion of the cell body enhances Caulobacter crescentus motility". In: *Proceedings of the National Academy of Sciences of the United States of America* 111.31, pp. 11252–11256.

Lo, Chien Jung et al. (2007). "Nonequivalence of membrane voltage and ion-gradient as driving forces for the bacterial flagellar motor at low load". In: *Biophysical Journal* 93.1, pp. 294–302.

Lo, Chien-Jung et al. (2013). "Mechanism and kinetics of a sodium-driven bacterial flagellar motor". In: *Proceedings of the National Academy of Sciences of the United States of America* 110.28, E2544–E2551.

Lockwood, Daniel B. et al. (2005). "Blue light generates reactive oxygen species (ROS) differentially in tumor vs. normal epithelial cells". In: *Dental Materials* 21.7, pp. 683–688.

Lolkema, Juke S., Klaas J. Hellingwerf, and Wil N. Konings (1982). "The effect of 'probe binding' on the quantitative determination of the protonmotive force in bacteria". In: *Biochimica et Biophysica Acta - Bioenergetics* 681.1, pp. 85–94.

Lowe, Graeme, Markus Meister, and Howard C. Berg (1987). "Rapid rotation of flagellar bundles in swimming bacteria". In: *Nature* 325, pp. 637–640.

Lund, Peter, Angela Tramonti, and Daniela De Biase (2014). "Coping with low pH: Molecular strategies in neutralophilic bacteria". In: *FEMS Microbiology Reviews* 38.6, pp. 1091–1125.

Magariyama, Yukio et al. (1995). "Simultaneous measurement of bacterial flagellar rotation rate and swimming speed." In: *Biophysical Journal* 69, pp. 2154–2162.

Magariyama, Yukio, Shigeru Sugiyama, and Seishi Kudo (2001). "Bacterial swimming speed and rotation rate of bundled flagella". In: *FEMS Microbiology Letters* 199.1, pp. 125–129.

Mancini, Leonardo et al. (2018). "Membrane voltage dyes: probes or actuators?" In: *In preparation*.

Mandadapu, Kranthi K et al. (2015). "Mechanics of torque generation in the bacterial flagellar motor". In: *Proceedings of the National Academy of Sciences of the United States of America* 112.32, E4381–E4389. arXiv: arXiv:1501.02883v1.

Manson, Michael D., P. M. Tedesco, and Howard C. Berg (1980). "Energetics of flagellar rotation in bacteria". In: *Journal of Molecular Biology* 138.3, pp. 541–561.

Martinac, B et al. (1987). "Pressure-sensitive ion channel in Escherichia coli." In: *Proceedings of the National Academy of Sciences of the United States of America* 84.8, pp. 2297–2301.

Martinez, Keith A et al. (2012a). "Cytoplasmic pH response to acid stress in individual cells of Escherichia coli and Bacillus subtilis observed by fluorescence ratio imaging microscopy". In: *Applied and Environmental Microbiology* 78.10, pp. 3706–3714.

Martinez, Vincent A. et al. (2012b). "Differential dynamic microscopy: A high-throughput method for characterizing the motility of microorganisms". In: *Biophysical Journal* 103.8, pp. 1637–1647. arXiv: 1202.1702.

Martinez-Salas, Encarnacion, Juan A. Martin, and Miguel Vicente (1981). "Relationship of Escherichia coli density to growth rate and cell age". In: *Journal of Bacteriology* 147.1, pp. 97–100.

Matlashov, Mikhail E. et al. (2015). "Fluorescent ratiometric pH indicator SypHer2: Applications in neuroscience and regenerative biology". In: *Biochimica et Biophysica Acta - General Subjects* 1850.11, pp. 2318–2328.

Matsuura, Shusuke, Jun ichi Shioi, and Yasuo Imae (1977). "Motility in Bacillus subtilis driven by an artificial protonmotive force". In: *FEBS Letters* 82.2, pp. 187–190.

McElroy, William D. (1947). "The Energy Source for Bioluminescence in an Isolated System." In: *Proceedings of the National Academy of Sciences of the United States of America* 33.11, pp. 342–5.

McRae, Donald G., Etsuo Yamamoto, and G. H.Neil Towers (1985). "The mode of action of polyacetylene and thiophene photosensitizers on liposome permeability to glucose". In: *Biochimica et Biophysica Acta - Biomembranes* 821.3, pp. 488–496.

Meister, Markus, Graeme Lowe, and Howard C Berg (1987). "The proton flux through the bacterial flagellar motor". In: *Cell* 49.5, pp. 643–650.

Meng, Jiao et al. (2016). "High-yield anaerobic succinate production by strategically regulating multiple metabolic pathways based on stoichiometric maximum in Escherichia coli". In: *Microbial Cell Factories* 15.1, p. 141.

Merlin, Christophe, Sean Mcateer, and Millicent Masters (2002). "Tools for Characterization of Escherichia coli Genes of Unknown Function". In: *Journal of Bacteriology* 184.16, pp. 4573–4581.

Miesenböck, Gero, Dino A. De Angelis, and James E. Rothman (1998). "Visualizing secretion and synaptic transmission with pH-sensitive green fluorescent proteins". In: *Nature* 394.6689, pp. 192–195. arXiv: `9810036 [physics]`.

Miller, Samuel I, Anne M Kukral, and John J Mekalanos (1989). "A two-component regulatory system (phoP phoQ) controls Salmonella typhimurium virulence." In: *Proceedings of the National Academy of Sciences of the United States of America* 86.13, pp. 5054–5058.

Mitchell, Peter (1961). "Coupling of phosphorylation to electron and hydrogen transfer by a chemi-osmotic type of mechanism". In: *Nature* 191.4784, pp. 144–148.

Miyamoto, V.K and T.E Thompson (1967). "Some electrical properties of lipid bilayer membranes". In: *Journal of Colloid and Interface Science* 25.1, pp. 16–25.

Molina, Pablo M, Alberto E Parma, and Marcelo E Sanz (2003). "Survival in acidic and alcoholic medium of Shiga toxin-producing Escherichia coli O157:H7 and non-O157:H7 isolated in Argentina". In: *BMC Microbiology* 3.1, pp. 1–6.

Moon, Richard B. and John H. Richards (1973). "Communication Determination of Intracellular pH by 31P Magnetic Resonance". In: *The Journal of Biological Chemistry* 248.20, pp. 7276–7278.

Morimoto, Yusuke V. et al. (2011). "M153R mutation in a pH-sensitive green fluorescent protein stabilizes its fusion proteins". In: *PLoS ONE* 6.5, e19598.

Nagai, Takeharu et al. (2001). "Circularly permuted green fluorescent proteins engineered to sense Ca2+". In: *Proceedings of the National Academy of Sciences of the United States of America* 98.6, pp. 3197–3202.

Nelson, Philip C (2003). *Biological Physics: Energy, Information, Life*. Freeman, W.H.

Neuman, Keir C et al. (1999). "Characterization of photodamage to Escherichia coli in optical traps". In: *Biophysical Journal* 77.5, pp. 2856–2863.

Nicholls, David G. and Stuart J. Ferguson (1992). *Bioenergetics 2*. Academic Press, p. 272.

Nirody, Jasmine A., Richard M. Berry, and George Oster (2016). "The Limiting Speed of the Bacterial Flagellar Motor". In: *Biophysical Journal* 111.3, pp. 557–564. arXiv: 1505.05966.

Nirody, Jasmine A, Yi-Ren Sun, and Chien-Jung Lo (2017). "The biophysicist's guide to the bacterial flagellar motor". In: *Advances in Physics: X* 2.2, pp. 324–343.

Nord, Ashley L et al. (2017). "Catch bond drives stator mechanosensitivity in the bacterial flagellar motor". In: *Proceedings of the National Academy of Sciences of the United States of America* 114.49, pp. 12952–12957.

Noumi, Takato, Masatomo Maeda, and Masamitsu Futai (1987). "Mode of inhibition of sodium azide on H+-ATPase of Escherichia coli". In: *FEBS Letters* 213.2, pp. 381–384.

Nyström, Thomas and Niklas Gustavsson (1998). "Maintenance energy requirement: What is required for stasis survival of Escherichia coli?" In: *Biochimica et Biophysica Acta - Bioenergetics* 1365.1-2, pp. 225–231.

Otsu, Nobuyuki (1979). "A Threshold Selection Method from Gray-Level Histograms". In: *IEEE Transactions on Systems, Man, and Cybernetics* 9.1, pp. 62–66. arXiv: arXiv:1011.1669v3.

Pashkovskaya, Alina et al. (2010). "Light-triggered liposomal release: Membrane permeabilization by photodynamic action". In: *Langmuir* 26.8, pp. 5725–5733.

Paul, Koushik et al. (2010). "The c-di-GMP Binding Protein YcgR Controls Flagellar Motor Direction and Speed to Affect Chemotaxis by a "Backstop Brake" Mechanism". In: *Molecular Cell* 38.1, pp. 128–139.

Peterka, Darcy S, Hiroto Takahashi, and Rafael Yuste (2011). "Imaging Voltage in Neurons". In: *Neuron* 69.1, pp. 9–21.

Peters, Joseph E. and Nancy L. Craig (2001). "Tn7: Smarter than we thought". In: *Nature Reviews Molecular Cell Biology* 2.11, pp. 806–814.

Pilizota, Teuta et al. (2007). "A programmable optical angle clamp for rotary molecular motors". In: *Biophysical Journal* 93.1, pp. 264–275.

Pilizota, Teuta and Joshua W. Shaevitz (2012). "Fast, multiphase volume adaptation to hyperosmotic shock by Escherichia coli." In: *PLoS ONE* 7.4. Ed. by Rajeev Misra, e35205.

Prindle, Arthur et al. (2015). "Ion channels enable electrical communication in bacterial communities". In: *Nature* 527.7576, pp. 59–63. arXiv: 15334406.

Prüss, Birgit M. et al. (1994). "Mutations in NADH: ubiquinone oxidoreductase of Escherichia coli affect growth on mixed amino acids." In: *Journal of Bacteriology* 176.8, pp. 2143–50.

Pu, Yingying et al. (2016). "Enhanced Efflux Activity Facilitates Drug Tolerance in Dormant Bacterial Cells". In: *Molecular Cell* 62.2, pp. 284–294.

Pu, Yingying et al. (2018). "ATP-dependent dynamic protein aggregation regulates bacterial dormancy depth critical for antibiotic tolerance". In: *In review*.

Rasmussen, Hans N. and Ulla F Rasmussen (2003). "Oxygen solubilities of media used in electrochemical respiration measurements". In: *Analytical Biochemistry* 319.1, pp. 105–113.

Reid, Stuart W et al. (2006). "The maximum number of torque-generating units in the flagellar motor of Escherichia coli is at least 11". In: *Proceedings of the National Academy of Sciences of the United States of America* 103.21, pp. 8066–8071.

Richardson, Eric S. and Yong-Fu Xiao (2010). "Electrophysiology of Single Cardiomyocytes: Patch Clamp and Other Recording Methods". In: *Cardiac Electrophysiology Methods and Models*. Boston, MA: Springer US, pp. 329–348.

Richter, Christoph (1987). "Biophysical consequences of lipid peroxidation in membranes". In: *Chemistry and Physics of Lipids* 44.2-4, pp. 175–189.

Robey, R. Brooks et al. (1998). "pH-Dependent Fluorescence of a Heterologously Expressed Aequorea Green Fluorescent Protein Mutant: In Situ Spectral Characteristics and Applicability to Intracellular pH Estimation". In: *Biochemistry* 37.28, pp. 9894–9901.

Rosko, Jerko (2017). "Osmotaxis in Escherichia coli". PhD thesis. The Edinburgh University.

Rosko, Jerko et al. (2017). "Osmotaxis in Escherichia coli through changes in motor speed". In: *Proceedings of the National Academy of Sciences of the United States of America* 114.38, E7969–E7976. arXiv: 1703.03926.

Ruthe, Hans Jürgen and Julius Adler (1985). "Fusion of bacterial spheroplasts by electric fields". In: *Biochimica et Biophysica Acta - Biomembranes* 819.1, pp. 105–113.

Ryu, William S., Richard M. Berry, and Howard C. Berg (2000). "Torque-generating units of the flagellar motor of Escherichia coli have a high duty ratio". In: *Nature* 403.6768, pp. 444–447.

Salmon, Sarah A. and Jeffrey L. Watts (2000). "Minimum inhibitory concentration determinations for various antimicrobial agents against 1570 bacterial isolates from turkey poults." In: *Avian diseases* 44.1, pp. 85–98.

Schoepfer, Ralf (1993). "The pRSET family of T7 promoter expression vectors for Escherichia coli". In: *Gene* 124.1, pp. 83–85.

Schwarz-Linek, Jana et al. (2016). "Escherichia coli as a model active colloid: A practical introduction". In: *Colloids and Surfaces B: Biointerfaces* 137, pp. 2–16. arXiv: 1506.04562v1.

Schwarzländer, Markus et al. (2014). "The 'mitoflash' probe cpYFP does not respond to superoxide". In: *Nature* 514.7523, E12–E14. arXiv: 15334406.

Schwiening, Christof J (2007). "Measurement of Intracellular pH: a comparison between ion-sensitive microelectrodes and fluorescent dyes". In: *Regulation of tissue pH in plants and animals: a reappraisal of current techniques*. Cambridge University Press.

Sezonov, Guennadi, Danièle Joseleau-Petit, and Richard D'Ari (2007). "Escherichia coli physiology in Luria-Bertani broth". In: *Journal of Bacteriology* 189.23, pp. 8746–8749. arXiv: /linkinghub.elsevier.com/retrieve/pii/S0960982205000989 [http:].

Shaner, Nathan C et al. (2004). "Improved monomeric red, orange and yellow fluorescent proteins derived from Discosoma sp. red fluorescent protein". In: *Nature Biotechnology* 22.12, pp. 1567–1572. arXiv: NIHMS183007.

Shen, En Zhi et al. (2014). "Mitoflash frequency in early adulthood predicts lifespan in caenorhabditis elegans". In: *Nature* 508.1, pp. 128–132.

Silverman, Michael and Melvin Simon (1974). "Flagellar rotation and the mechanism of bacterial motility". In: *Nature* 249.5452, pp. 73–74.

Slonczewski, Joan L et al. (1981). "pH homeostasis in Escherichia coli: measurement by 31P nuclear magnetic resonance of methylphosphonate and

phosphate." In: *Proceedings of the National Academy of Sciences of the United States of America* 78.10, pp. 6271–6275.

Slonczewski, Joan L et al. (1982). "Effects of pH and Repellent Tactic Stimuli on Protein Methylation Levels in Escherichia coli Effects of pH and Repellent Tactic Stimuli on Protein Methylation Levels in Escherichia coli". In: *Journal of Bacteriology* 152.1, pp. 384–399.

Slonczewski, Joan L. et al. (2009). "Cytoplasmic pH Measurement and Homeostasis in Bacteria and Archaea". In: *Advances in Microbial Physiology* 55.

Slonczewski, Joan L. and John W. Foster (2017). *Microbiology: An Evolving Science*. 4th. New York, London: W. W. Norton & Company, p. 1174.

Sowa, Yoshiyuki et al. (2003). "Torque-speed relationship of the Na+-driven flagellar motor of Vibrio alginolyticus". In: *Journal of Molecular Biology* 327.5, pp. 1043–1051.

Sowa, Yoshiyuki and Richard M Berry (2008). "Bacterial flagellar motor". In: *Quarterly Reviews of Biophysics* 41.2, pp. 103–132.

Stincone, Anna et al. (2011). "A systems biology approach sheds new light on Escherichia coli acid resistance". In: *Nucleic Acids Research* 39.17, pp. 7512–7528.

Storz, Gisela and James A Imlayt (1999). "Oxidative stress". In: *Current Opinion in Microbiology* 2.2, pp. 188–194.

Studier, F William and Barbara A Moffatt (1986). "Use of bacteriophage T7 RNA polymerase to direct selective high-level expression of cloned genes". In: *Journal of Molecular Biology* 189.1, pp. 113–130.

Svoboda, Karel et al. (1993). "Direct observation of kinesin stepping by optical trapping interferometry". In: *Nature* 365.6448, pp. 721–727.

Tantama, Mathew, Yin Pun Hung, and Gary Yellen (2011). "Imaging Intracellular pH in Live Cells with a Genetically-Encoded Red Fluorescent Protein Sensor". In: *Journal of the American Chemical Society* 133.26, pp. 10034–10037.

Tantama, Mathew et al. (2013). "Imaging energy status in live cells with a fluorescent biosensor of the intracellular ATP-to-ADP ratio". In: *Nature Communications* 4, p. 2550.

Taute, K. M. et al. (2015). "High-throughput 3D tracking of bacteria on a standard phase contrast microscope". In: *Nature Communications* 6.1, p. 8776.

Thomas, R. C. (1974). "Intracellular pH of snail neurones measured with a new pH-sensitive glass micro-electrode". In: *The Journal of Physiology* 238.1, pp. 159–180.

Tipping, Murray J et al. (2013). "Load-dependent assembly of the bacterial flagellar motor". In: *mBio* 4.4.

Tran, Quang Hon and Gottfried Unden (1998). "Changes in the proton potential and the cellular energetics of Escherichia coli during growth by aerobic and anaerobic respiration or by fermentation". In: *European Journal of Biochemistry* 251.1-2, pp. 538–543.

Turner, Linda, William S Ryu, and Howard C Berg (2000). "Real-time imaging of fluorescent flagellar filaments". In: *Journal of Bacteriology* 182.10, pp. 2793–2801.

Unden, Gottfried and J. Bongaerts (1997). "Alternative respiratory pathways of Escherichia coli: Energetics and transcriptional regulation in response to electron acceptors". In: *Biochimica et Biophysica Acta - Bioenergetics* 1320.3, pp. 217–234.

Van Rotterdam, Bart J. et al. (2002). "Simplicity in complexity: The photosynthetic reaction center performs as a simple 0.2 V battery". In: *FEBS Letters* 510.1-2, pp. 105–107.

Vemuri, Goutham N. et al. (2006). "Overflow metabolism in Escherichia coli during steady-state growth: Transcriptional regulation and effect of the redox ratio". In: *Applied and Environmental Microbiology* 72.5, pp. 3653–3661.

Walter, Jessica M et al. (2007). "Light-powering Escherichia coli with proteorhodopsin." In: *Proceedings of the National Academy of Sciences of the United States of America* 104.7, pp. 2408–12.

Wang, Wang et al. (2008). "Superoxide Flashes in Single Mitochondria". In: *Cell* 134.2, pp. 279–290.

Wang, Yao Kuan et al. (2018). "Bacterial Immobilization Assays for Single Cell Experiment." In: *In preparation*.

Wilks, Jessica C and Joan L Slonczewski (2007). "pH of the cytoplasm and periplasm of Escherichia coli: Rapid measurement by green fluorescent protein fluorimetry". In: *Journal of Bacteriology* 189.15, pp. 5601–5607.

Wilson, Laurence G. et al. (2011). "Differential dynamic microscopy of bacterial motility". In: *Physical Review Letters* 106.1, p. 018101. arXiv: 1004.4764.

Winkel, J. Derk te et al. (2016). "Analysis of Antimicrobial-Triggered Membrane Depolarization Using Voltage Sensitive Dyes". In: *Frontiers in Cell and Developmental Biology* 4, p. 29.

Wong-Ekkabut, Jirasak et al. (2007). "Effect of lipid peroxidation on the properties of lipid bilayers: A molecular dynamics study". In: *Biophysical Journal* 93.12, pp. 4225–4236.

Yagi, Hiromasa et al. (2007). "Structures of the thermophilic F1-ATPase epsilon subunit suggesting ATP-regulated arm motion of its C-terminal domain in F1". In: *Proceedings of the National Academy of Sciences of the United States of America* 104.27, pp. 11233–11238.

Yaginuma, Hideyuki et al. (2014). "Diversity in ATP concentrations in a single bacterial cell population revealed by quantitative single-cell imaging". In: *Scientific Reports* 4.1, p. 6522.

Zhao, Xilin and Karl Drlica (2014). "Reactive oxygen species and the bacterial response to lethal stress". In: *Current Opinion in Microbiology* 21, pp. 1–6. arXiv: NIHMS150003.

Zilberstein, Dan et al. (1984). "Escherichia coli intracellular pH, membrane potential, and cell growth". In: *Journal of Bacteriology* 158.1, pp. 246–252.